ASA TECHNICAL
MEMORANDUM

1. NASA TM X-3246

NASA TM X-3246

2. 21/21

EFFECT OF INLET INGESTION OF A WING TIP VORTEX ON COMPRESSOR FACE FLOW AND TURBOJET STALL MARGIN

Glenn A. Mitchell

ewis Research Center
leveland, Ohio 44135

ATIONAL AERONAUTICS AND SPACE ADMINISTRATION • WASHINGTON, D. C. • JULY 1975

5.

1. Report No. NASA TM X-3246	2. Government Accession No.	3. Recipient's Catalog No.

4. Title and Subtitle

EFFECT OF INLET INGESTION OF A WING TIP VORTEX ON COMPRESSOR FACE FLOW AND TURBOJET STALL MARGIN

5. Report Date
July 1975

6. Performing Organization Code

7. Author(s)

Glenn A. Mitchell

8. Performing Organization Report No.
E-8213

9. Performing Organization Name and Address

Lewis Research Center
National Aeronautics and Space Administration
Cleveland, Ohio 44135

10. Work Unit No.
505-11

11. Contract or Grant No.

12. Sponsoring Agency Name and Address

National Aeronautics and Space Administration
Washington, D.C. 20546

13. Type of Report and Period Covered
Technical Memorandum

14. Sponsoring Agency Code

15. Supplementary Notes

16. Abstract

A two-dimensional inlet was alternately mated to a coldpipe plug assembly and a J85-GE-13 turbojet engine, and placed in a Mach 0.4 stream so as to ingest the tip vortex of a forward mounted wing. Vortex properties were measured just forward of the inlet and at the compressor face. Results show that ingestion of a wing tip vortex by a turbojet engine can cause a large reduction in engine stall margin. The loss in stall compressor pressure ratio was primarily dependent on vortex location and rotational direction and not on total-pressure distortion.

17. Key Words (Suggested by Author(s))

Intake systems; Engine inlets; Turbojet engines; Distortion; Ingestion (engines); Tip vortices; Engine failure (stalling); Supersonic inlets

18. Distribution Statement

Unclassified - unlimited
STAR Category 02 (rev.)

19. Security Classif. (of this report)	20. Security Classif. (of this page)	21. No. of Pages	22. Price*
Unclassified	Unclassified	78	$4.75

---

* For sale by the National Technical Information Service, Springfield, Virginia 22151

EFFECT OF INLET INGESTION OF A WING TIP VORTEX ON COMPRESSOR FACE FLOW AND TURBOJET STALL MARGIN

by Glenn A. Mitchell

Lewis Research Center

SUMMARY

A two-dimensional inlet was alternately mated to a coldpipe plug assembly and a J85-GE-13 turbojet engine, and placed in a Mach 0.4 stream in the Lewis 10- by 10-Foot Supersonic Wind Tunnel so as to ingest the tip vortex of a forward mounted wing. The vortex was ingested at various vertical locations across the inlet entrance. Wing angle variations were utilized to produce vortices of maximum strength that rotated either with or opposite to the engine rotation. Vortex properties were measured just forward of the inlet and at the compressor face.

Results show that ingestion of a wing tip vortex by a turbojet engine can cause a reduction in engine stall margin. Stall occurred at a compressor pressure ratio that was as much as 28 percent (along a line of constant corrected speed) closer to the nominal normal operating line than the predicted stall pressure ratio attainable with total-pressure distortion alone. Vortex location at the compressor face and vortex rotational direction had a significant effect on stall compressor pressure ratio. Vortex induced losses in stall pressure ratio did not correlate with compressor face total-pressure distortions.

The core of the ingested vortex was small enough that its total-pressure loss was not always sensed by the compressor face total-pressure rakes. Also, the vortex affected the compressor face distortion by altering total pressures at locations away from the immediate vicinity of the vortex. Vortex ingestion generally increased distortion up to 2 percent.

The vortex displayed a maximum tangential (or rotational) velocity of 51 percent of free-stream velocity prior to entering the inlet, and a maximum tangential velocity of 30 percent of average axial velocity at the compressor face.

INTRODUCTION

Some aircraft require the use of forward mounted stub wings for stability and control purposes. At large angles of attack such a wing would generate a strong tip vortex. With propulsion systems mounted on or close to the fuselage, it is probable that certain combinations of airplane pitch and yaw would cause the vortex to trail aft into an engine air inlet. The effects of such a vortex on engine operating characteristics are unknown but may be degrading enough to cause engine stall.

A two part study of these phenomena was conducted in the Lewis 10- by 10-Foot Supersonic Wing Tunnel with the test section operating at a subsonic speed of Mach 0.4. The Reynolds number was 7.5×10^6 per meter. A wing was mounted in the test section so that its tip vortex trailed aft into a two-dimensional inlet.

In the initial study the inlet was mated to a coldpipe choked exit plug assembly. A rake of probes capable of measuring steady-state flow angles in a single plane was mounted forward of the inlet to survey the vortex and determine the wing angle of attack yielding the maximum vortex strength. Initial data were obtained on the effects of this vortex on standard steady-state compressor face total-pressure rakes. The rake of flow angularity probes was placed near the compressor face for part of the initial study to measure vortex strength at this location. Results of this preliminary study are reported in reference 1.

For the final part of the study the inlet was mated to a J85-GE-13 turbojet engine and more sophisticated flow angularity probes were utilized. These were capable of measuring steady-state flow angles in any plane and yielding axial and tangential flow velocities. A rake of these probes was placed forward of the inlet and, later, at the compressor face to determine vortex properties at both locations. The effects of the ingested vortex on compressor face total pressures, distortion, and J85-GE-13 turbojet stall margin were determined. Effects on turbojet stall margin are reported in reference 2. Results presented herein cover both parts of the study, including information contained in references 1 and 2.

U. S. Customary Units were used in the design of the test model and for the recording and computing of experimental data. These units were converted to the International System of Units for presentation in this report.

APPARATUS AND PROCEDURE

Inlet

The inlet used in this investigation was a two-dimensional, external compression type designed for operation at a Mach number of 2.2. The inlet was attached to a cylindrical nacelle 0.635 meter in diameter in which a J85-GE-13 engine or a coldpipe choked exit plug assembly could be installed. The inlet with coldpipe assembly, as used in the initial study (ref. 1), is shown in figure 1 mounted in the tunnel test section. The inlet height (ramp edge to cowl lip) was 0.408 meter and the ramp width was 0.369 meter.

The inlet geometry was varied by movable ramps. The first ramp was a fixed one, having an angle of 3° with the inlet at 0° angle of attack. The second and third ramps were variable and together with the first ramp accomplished external compression during supersonic operation. The fourth ramp was a backward facing ramp which initiated internal flow diffusion. For this test the inlet throat area was opened to a maximum by setting the ramps as flat as possible. The resulting second and third ramp angles of $5\frac{1}{3}^{\circ}$ and $7\frac{2}{3}^{\circ}$ measured relative to the inlet at 0° angle of attack are shown in figure 1. A bleed slot between the third and fourth ramp was available for boundary layer control. All bleed and bypass systems were closed for this test.

Some variations exist between the inlet configuration shown in the figure and the configurations used during this test. The vortex generators shown in figure 1 on the ramp and side walls were not present. Also the cowl lip was 0.76 centimeter thick and not sharp edged but blunted with a 3-to-1 ellipse. During the initial test phase, when the inlet was terminated with a coldpipe, the side fairings were sharp lipped. They were not cut back as in figure 1 but extended straight from the ramp edge at the design shock angle to a point just above the cowl lip. During the engine portion of the test, the side fairings were cut back as shown. The leading edge was not sharp but blunted with a radius of 0.42 centimeter.

Engine

The J85-GE-13 engine consists of an eight-stage axial-flow compressor coupled directly to a two-stage turbine. It incorporates controlled compressor interstage bleed and variable inlet guide vanes, a through-flow annular combustor, and an afterburner (not used in this test) with a variable area primary exhaust nozzle. Engine installation is shown in figure 2.

At sea-level conditions and military power operation, the eight-stage compressor develops an overall static pressure ratio of 7.0. The pressure ratio per stage averages out to 1.275.

The compressor interstage bleed valves (located after the third, fourth, and fifth compressor stages) are mechanically linked to the variable inlet guide vanes so that when the bleed valves are fully open, the guide vanes are fully closed. The inlet guide vanes are linked together and scheduled by the main fuel control as a function of corrected speed. This provides the normal interstage bleed schedule. For stall attempts during this test and for all comparison data presented herein, the guide vanes were computer controlled on a nonstandard schedule providing the maximum allowable bleed closure for safe engine operation as dictated by compressor blade vibration limits. This procedure was required to obtain the maximum assurance of engine stall at corrected speeds below 94 percent of rated speed.

Compressor stalls were initiated by closing the exhaust nozzle. In order to lower turbine temperatures during this procedure, the first stage turbine nozzle was replaced by a unit approximately 14 percent smaller in area. This rematched the turbine to the compressor at a lower than normal turbine inlet temperature.

At engine speeds below 90 percent of rated speed, manual closure of the standard exhaust nozzle resulted in minimum nozzle areas that were too large to cause compressor stall. To obtain smaller nozzle areas (and higher compressor pressure ratios), six airflow blockage plates were installed inside the nozzle leaves.

Steady-state operation of the J85-GE-13 engine, while coupled to an axisymmetric mixed-compression inlet is reported in reference 3. Reference 4 reports transient interactions between the engine and the same inlet.

Wing

Details of the wing are shown in figure 3. The wing had a slight aft sweep of the leading edge and a forward sweep of the trailing edge. Also, the wing was symmetrical with parallel upper and lower surfaces over much of the chord. The leading edge was a 4.52-to-1 ellipse and the trailing edge was formed by a 25° included angle and faired into the straight sides of the wing.

The wing was mounted in the tunnel test section forward of the inlet and extended vertically down from a circular inset in the tunnel ceiling (fig. 4). Wing angle of attack was varied by rotating the circular inset. The inlet location aft of the wing (fig. 5) placed the ramp edge 8.2 wing-tip chord lengths downstream of the wing-tip trailing edge. A typical vortex path from the wing to the inlet is shown in figures 5 and 6. This path was produced by the wing at $+11^{\circ}$ angle of attack (ref. 1). The inlet is shown at 0° angle of attack. The inlet was placed at various vertical locations relative to the vortex trailing aft from the wing by pitching the inlet to various angles of attack. The vortex position could be varied from the ramp edge to the cowl lip by varying inlet angle of attack from 0° to -7°. As indicated in figure 5, positive angle of attack was opposite to the normal convention. This was because the inlet was mounted upside down in the tunnel.

Instrumentation

During parts of the test program, a rake of flow angularity probes was mounted in front of the inlet to survey the wing tip vortex. Initial surveys were made with a rake whose probes measured steady-state flow angles in the vertical direction only. Flow velocities derived from these angles by means of the tangent function were thus limited to those in the wing spanwise direction ratioed to local axial velocity. This rake of two-dimensional probes was later replaced with a rake of more sophisticated three-dimensional probes which measured steady-state flow angles in both vertical and horizontal planes. In addition these probes were calibrated to yield static and total pressures. Probe measurements were converted to an axial velocity and velocities in the lateral plane by means of geometric relations and flow equations assuming no total temperature loss. The lateral velocities were resolved into wing spanwise and normal components.

Placement of the flow angularity rakes in front of the inlet is shown in figure 5. The vertical location of each rake was 20.3 centimeters above the ramp edge. This placed each rake on the inlet horizontal centerline at 0° inlet angle of attack. Each rake was placed 30.48 centimeters forward of the ramp leading edge as shown in figures 7 and 8. The lateral locations of the flow angularity probes on each rake are shown in the appropriate figure.

Each two-dimensional probe consisted of three 0.084-centimeter outside-diameter stainless-steel tubes which were soldered adjacent to each other in a plane normal to the rake (fig. 7). The top and bottom tubes were cut at a 45° angle as shown. The three-dimensional probes were also fabricated from 0.084-centimeter-diameter stainless-steel tubes but were soldered in a cruciform pattern (fig. 8). The four extreme tubes of the cruciform were cut at a 45° angle. Details of these probe designs and calibration data are reported in reference 5.

The probes were calibrated in a free-jet facility at a Mach number of 0.4. Each two-dimensional probe was calibrated at angles normal to the rake from -35° to $+35^{\circ}$. The effect of yaw flow on the normal plane calibrations was not determined for each probe. According to reference 5, a yaw flow of 30° causes up to a 4° error in the normal plane calibration. For the current test such errors were not considered important because credence was given to the measured flow angles only when the rake was near the vortex center where little yaw flow existed.

The three-dimensional probes were not calibrated before the test and, unfortunately, many of them were severely damaged on removal from the model. Therefore an individual calibration of each probe as it existed during the test program was impossible. A single, undamaged, probe was calibrated to $\pm 35^{\circ}$ in both pitch and yaw planes and its calibration used for all of the three-dimensional probes. Although the calibration curves for all probes of this type are similar, small physical differences between probes exist within the specified manufacturing tolerances and cause zero shifts and slope changes in the calibrations. Thus the use of a single calibration for all probes introduces some error.

However, calibrations of two additional three-dimensional probes were available. These probes were made by the same manufacturing techniques and had the same type rake body as the probes used in this test. A statistical comparison was made comparing the calibration data of these probes to the data of the single undamaged probe. Due to the primary concern of high flow angles in the vortex, the comparisons were limited to flow angles of 10° and greater. From these comparisons the probable errors introduced by using a single probe calibration for the two other probes were computed and found to be acceptable. The errors are tabulated in table I. If these errors are typical, then the actual errors due to using the single probe calibration for all rake probes are of similar magnitude.

Figure 9 presents the compressor face instrumentation installed during the coldpipe portion of the test. This figure shows the compressor face in its normal position rather than the inverted testing position shown in figure 1. Because a complete array of total-pressure rakes was not available, the rakes were installed primarily in the left side of the duct. The rake of two-dimensional flow angularity probes was, for a part of the coldpipe test (ref. 1), installed just forward of the compressor face station at the circumferential position shown in figure 9. It was inserted into the duct through the bypass opening at the axial location shown in figure 2. Because of mounting problems only six of the seven probes could be placed in the duct.

The compressor face instrumentation installed during the engine portion of the test is shown in figure 10. The 36 total-pressure probe array shown in the figure was area weighted in the following manner. The compressor face area was divided into six equal area rings. Long rakes were placed 60° apart around the duct with three total-pressure probes in each rake. Probes were centered at the mid-area locations of the first ring (innermost), third ring, and fifth ring. Short rakes were centered between the long rakes. The total-pressure probes of the short rakes were centered at the mid-area locations of the second, fourth, and sixth rings. Location of the rake of three-dimensional flow angularity probes when installed at the compressor face is shown in the figure.

The engine compressor discharge pressure was measured by the eight radially area weighted total-pressure probes shown in figure 11. Engine speed was measured by a magnetic pickup which sensed the tooth passage of a rotating gear which was attached to the customer power takeoff shaft from the engine gearbox. Turbine discharge temperature was carefully monitored during all engine stall attempts and was measured by eight thermocouples, which were installed by the engine manufacturer and wired in parallel to give an average reading.

The engine corrected airflow was not measured directly but was determined from the compressor operating map previously determined for this engine in connected pipe tests (ref. 6). Specifically, the corrected airflow was picked from the compressor map to correspond to the measured compressor pressure ratio and engine corrected speed. This procedure required a linear interpolation between the existing constant corrected speed lines.

During the engine portion of the test, the mass-flow ratios were determined from the engine corrected airflows and free-stream conditions. Mass-flow ratios were also computed from the compressor face static and total pressures and plotted against the engine derived mass-flow ratios to form a correlation curve. For the coldpipe part of the test, mass-flow ratios were initially computed from the compressor face pressures by assuming rakes 1 to 6 to be area weighted. These mass-flow ratios were converted to engine derived values (hereinafter called estimated values) by means of the correlation curve.

Test Procedure

The initial part of the coldpipe portion of the test program was conducted to obtain the strongest vortex from the wing (i. e., the one having the largest rotational velocity). This goal was attained by pitching the inlet to pass the forward mounted two-dimensional flow angularity rake across the vortex path and survey the vortex created by the wing at various angles of attack. In the engine portion of the test, the maximum strength vortex was resurveyed in front of the inlet using the more sophisticated three-dimensional flow angularity rake.

Vortex effects on compressor face flow and engine stall margin were obtained with the wing set at the angle yielding the strongest vortex. The forward mounted rakes were removed, allowing the vortex to trail undisturbed into the inlet.

To obtain the effects of the ingested vortex at the compressor face, a series of data points were obtained at each selected corrected airflow (or mass-flow ratio). Each point of the series occurred with the vortex entering the inlet at a different vertical location between the cowl lip and the inlet ramp edge. This placed the vortex at various locations across the compressor face. Prior to each series, a vertical location reference point was obtained by pitching the inlet and using the tunnel schlieren system to visually impinge the center of the trailing vortex on the cowl lip.

Data series obtained during the coldpipe test used a positive wing angle of attack whereas during the engine test data series were obtained at both positive and negative wing angles. A positive wing angle of attack (defined in fig. 12) produced a counterclockwise rotating vortex when viewed looking downstream, and conversely, a negative angle of attack produced a clockwise rotating vortex. To define the vortex effects at the compressor face more clearly, data series were also obtained without the vortex by removing the wing from the test section.

The three-dimensional flow angularity rake was installed at the compressor face for all of the aforementioned engine data series but was removed prior to any engine stall attempts. The two-dimensional flow angularity rake was installed near the compressor face for a single data series of the coldpipe test. The two-dimensional rake data are not presented herein but can be found in reference 1.

Engine stall attempts were made with the wing at both positive and negative wing angles of attack to produce vortices which rotated in the same direction as, and counter to, engine rotation. In addition, stall attempts were made at various selected engine corrected airflows and vortex positions.

All stall attempts were initiated at the lowest compressor pressure ratio available at the selected engine corrected airflow. The initial condition was achieved by controlling the throttle to set the selected corrected airflow while keeping the exhaust nozzle open. The stall point was approached by closing the nozzle to increase the compressor pressure ratio while manually biasing the throttle to keep a constant compressor face static- to total-pressure ratio (i. e., a constant corrected airflow). Stalls were attempted at a constant corrected airflow rather than a constant engine speed in order to keep the entering vortex at a constant position as stall was approached. Reference 1 reports that the vortex path in the vicinity of the inlet was affected by the airflow streamlines approaching the inlet in a manner such that the vertical position of the vortex at the inlet entrance varied with inlet mass-flow ratio, that is, corrected airflow.

Stall data presented later in this report were obtained at a compressor pressure ratio as close to stall as possible without stall occurring during the data scan. For most of these points stall occurred after the data scan; for others the pressure ratio was within 0.04 of the pressure ratio where stall occurred. When no stall occurred, data points were taken at the highest pressure ratio obtainable without exceeding the turbine discharge temperature limit of 1017 K.

Vortex Reference Systems

The vortex data obtained by surveys in front of the inlet were related to the wing geometry using the coordinate system presented in figure 12. Data from surveys of the vortex at the compressor face were related to the duct position of each three-dimensional flow angularity probe and to the ingested vortex vertical position parameter h/H. This parameter gives the approximate vertical position of the vortex at the cowl lip station relative to the inlet (see sketch (a)).

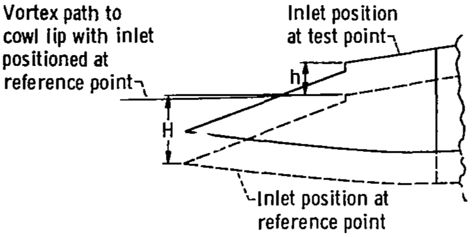

(a)

The numerator of the parameter h is the vertical distance of the cowl lip from the previously mentioned reference point (vortex on lip) as calculated by geometric relations and the inlet change in pitch angle from the reference point. The denominator H is simply the vertical distance from the cowl lip to the inlet ramp edge. The ratio h/H would then determine the vertical distance of the entering vortex from the cowl lip in relation to the inlet height; but only if the vortex path was unaffected by inlet vertical position. This was probably not true at the axial location of the cowl lip when the vortex was near the ramp and affected by the flow turning induced by the ramp angles. This could not be visually observed because of the inlet side fairings.

RESULTS AND DISCUSSION

Maximum Vortex Strength

The results of varying the wing angle of attack to obtain the strongest vortex are presented in figure 13. Each point on the plot represents the maximum tangential velocity produced at the rake station ($x/c \approx 7$) by the trailing vortex at a particular wing angle of attack. Each point was obtained from a survey of the vortex using the two-dimensional flow angularity rake. Obviously, the strongest vortex was produced by a wing angle of attack near 11°. Wing angles of either $\pm 11^{\circ}$ were therefore used during the remainder of the test program. The maximum spanwise velocity produced by the vortex at this streamwise station was recorded as 57 percent of the local axial velocity. Since the three-dimensional flow angularity rake data presented later in this report show the axial velocity to decrease across the vortex core, the measured spanwise velocity ratio would be somewhat lower if based on free-stream velocity.

Vortex Path to Inlet

The position of the vortex produced by the wing at 11° angle of attack is compared in figure 14 to data obtained by other investigators (refs. 7 to 9). These data were obtained using rectangular wings and known airfoil shapes as noted in the figure. The path of the vortex of the current test, as revealed by the rake surveys at $x/c \approx 7$, agrees quite well in the spanwise plane with those shown in the figure for references 7 to 9. The agreement is not as good in the normal axis, however, with the vortex of the present test trailing higher above the wing than the others. The tabulation of vortex core diameter in figure 14 indicates that the core size determined from the current test is a reasonable value. (The core diameter is the distance across the vortex center to the points of maximum rotational velocity.)

Also shown in figure 14 are spanwise vortex center positions at axial locations of 10 and 12.3 (x/c). These data show the vortex path to be greatly altered from the path reported by other investigators. The data were obtained from a schlieren photograph of the vortex path with the inlet model drooped below the vortex at 11.3°. Although the inlet centerline at the ramp edge was 2.8 wing tip chord lengths outboard of the wing tip (+y in fig. 12), the flow around the model greatly influenced the vortex path as shown in the figure. The schlieren photograph is shown in figure 15. The vortex path is clearly shown by the density gradient across the core region.

By analyzing a series of schlieren photographs such as was shown in figure 15, the effect of the spanwise position of the inlet on the vortex path was determined (fig. 16). The inlet was pitched to various angles, varying inlet spanwise positions inboard and outboard of the wing tip. The vortex center location at $x/c = 10$ was determined for each position; x/c of 10 was just downstream of the schlieren window upstream edge (fig. 5). Figure 16 shows that the spanwise vortex center location did not greatly vary with the inlet spanwise location. Also, figure 16 shows that a change in the inlet mass-flow ratio affected the vortex path. An increase in inlet flow spillage caused the vortex path to bend inboard. This might be expected because of the orientation of the two-dimensional inlet which directed spilled flow in the inboard direction. The effect of inlet mass-flow ratio, or spillage, on the vortex path near the cowl lip is strikingly illustrated by the schlieren photographs presented in figure 17.

Vortex Path From Inlet to Compressor Face

Figure 18 presents the variations in inlet entrance and compressor face vortex position obtained by pitching the inlet to vary the ingested vortex vertical position parameter h/H. Data are shown for the counterclockwise rotating vortex produced by the wing at 11° angle of attack. The lateral position of the vortex at the inlet entrance or cowl lip station (fig. 18(a)) was obtained by extrapolating the vortex path in the wing normal plane from figure 14. Vertical positions are approximated by the parameter h/H. Vortex positions at the compressor face (fig. 18(b)) were obtained from analysis of data from the three-dimensional flow angularity rake at the compressor face and the total-pressure rakes (fig. 10). Because of a total-pressure defect in the vortex core, the total-pressure probes sensed passage of the vortex as a total-pressure loss. Typical vortex passage "signatures" recorded by total-pressure probes are shown in figure 19.

Figure 18 illustrates the large lateral variations in the vortex path at the compressor face that were not present at the inlet entrance. These results were initially unexpected in that the vortex was expected to trail undisturbed to the compressor face and roughly reflect the entering positions. However, these expectations overlooked vortex path analyses previously applied to vortex generators in boundary-layer control work. Reference 10, for example, explains the observed lateral vortex displacement by demonstrating that a vortex near a surface is swept laterally along the surface by the induced velocity of the surface reflected vortex image. In addition, the lateral movement is greater when the vortex is closer to the surface (that is, nearer the cowl or ramp in fig. 18). The larger lateral movement observed when the vortex was near the ramp rather than the cowl was probably due to the longer surface run of the ramp.

Although the vortex path shown in figure 18(b) was obtained at an engine corrected airflow of 18 kilograms per second, it is a typical path for a counterclockwise rotating vortex because the path did not substantially change at other tested engine corrected airflows. The path shown in figure 18(b) also represents the path of a clockwise rotating vortex because it is, with small variations, a mirror image of the path of a clockwise vortex. Path similarities are illustrated in figure 20 which shows the positional variations of the vortex at different engine corrected airflows and opposite vortex rotational directions. The vortex positions were determined from total-pressure "signatures" and are shown in terms of the parameter h/H at various total-pressure probe locations. The probes shown for the clockwise vortex are located at the mirror-image compressor face positions of the probes shown for the counterclockwise vortex.

Effect of Vortex at Compressor Face

Selected compressor face total-pressure rake profiles obtained during the engine portion of the test are presented in figures 21 to 23. Each figure compares profiles obtained without the ingested vortex to profiles obtained with both clockwise and counterclockwise rotating vortices. The figures show clearly that the profiles obtained with opposite rotating vortices were mirror images of each other. This is of course a result of the mirror-image locations of the opposite rotating vortices and their similar but opposite hand effect not only near the vortex core locations but outside of the core over the entire compressor face flow field. For example, the flow field induced by the counterclockwise ingested vortex in figure 21(a) produced lower total pressures on rakes 8, 9, and 10 that were mirrored on rakes 6, 5, and 4 by the clockwise vortex induced flow field. An example of the vortex core in close proximity to a total-pressure probe is shown in figure 21(c). Both the clockwise and counterclockwise vortices were located at the bottom center hub-side probe (rake 7) which recorded the lower pressure in the vortex core. Mirror-image effects outside of the core of the opposite rotating vortices can also be seen in figure 21(c); notably on the tip probe of rakes 6 and 8.

The compressor face total-pressure profiles were essentially unchanged by variations of engine corrected airflow. For example, compare figures 21(b), 22(a), and 22(b). Higher pressure losses near the tip wall were observed at the higher corrected airflows, perhaps due to increased viscous effects.

With a series of compressor face total-pressure rake profiles such as shown in figure 21, and with the inlet located aft of a suspected vortex source of reasonable strength, it would be relatively easy to determine if the vortex was being ingested without special instrumentation such as a flow angularity rake. One clue that a vortex was present would be the detection of the core total-pressure loss by a probe pressure variation or "signature" (fig. 19) as the vortex passed by a probe. Also, the ingested vortex altered total pressures outside of the vortex core so that variations in total-pressure profiles from the profiles without the ingested vortex would be significant.

However, the presence of the ingested vortex would be almost impossible to detect with only a single set of compressor face total-pressure profiles if the vortex core was located unluckily between probes and no comparable vortex-free profiles were available. The diameter of the vortex core at the compressor face was about 0.3 of the annulus height as illustrated in figure 18(b) and could easily be located between many of the total-pressure probes. For example, at an ingested vortex vertical position parameter h/H of 0.150 (fig. 21(a)) the core of the counterclockwise vortex was located between rakes 8 and 9 where its total-pressure defect could not affect the probes. At an h/H of 0.41 this core was located between the hub and rake 6. A location near this ($h/H = 0.438$) is illustrated in figure 21(d). The core total-pressure defect was slightly affecting the hub side probe of rake 5.

At lower corrected airflows where viscous effects are less, the changes in compressor face total pressures from vortex-free to vortex-ingested flow are also less outside of the vortex core. Compare figures 21(a), 23(a), and 23(b). With only a single set of compressor face total-pressure profiles having the vortex located between probes, the presence of the vortex would be difficult to detect at the lowest corrected airflow even with comparable vortex-free profiles (fig. 23(b)). Thus reference 1, with vortex-free and vortex-ingested total-pressure profiles at conditions near those of figure 23(b), prematurely concluded that standard compressor face rakes would not detect a vortex at that airflow condition.

During the coldpipe portion of the test, compressor face total-pressure profiles were obtained at a corrected airflow higher than available with the engine; about 21.5

kilograms per second. The high airflow was obtained by removing the coldpipe assembly. This action also necessitated removal of the simulated compressor hub. In addition, an incomplete array of total-pressure rakes was available. The data are shown in figure 24 using the same format as the engine compressor face data.

As figure 24 shows, the ingestion of the vortex greatly changed the compressor face total-pressure profiles near the cowl side of the duct (rakes 6 and 7A). Without the ingested vortex, the pressure profiles indicate that the cowl side of the duct contained a large region of relatively low energy air. It appears that the action of the vortex was to energize this retarded flow region. This action appears similar to that induced by small vortices created by diffuser mounted vortex generators. They are reported in reference 11 to be capable of energizing retarded flow regions in a diffuser.

The coldpipe data of figure 24 were limited to values of the ingested vortex vertical position parameter h/H that ranged from zero to 0.5. In this range the vortex core total-pressure defect was not detected by any of the total-pressure probes except at an h/H of 0.14 (fig. 24(a)) where the lower total pressure was recorded by the hub side probe of rake 8. Because the hub was removed, the vortex path through this h/H range was probably nearer the duct center than it was during the engine portion of the test and missed most of the rakes.

Compressor face total-pressure distortions obtained during the engine portion of the test are presented in figure 25. Ingestion of the vortex increased distortion about 1 to 2 percent at the higher engine corrected airflows and up to 1 percent at the lower corrected airflows. These effects were due to lower tip pressures when the vortex was present. In general, the vortex core total pressure defect did not affect the measured distortion. Refer to figures 25(a) and (b) for example. With vortex ingestion the distortion level did not increase at conditions where the vortex was crossing over a probe. Evidently the minimum core total pressures recorded by the various probes were greater than the lowest total pressures near the duct tip. An exception to this fact occurred at the lowest corrected airflow with counterclockwise vortex ingestion (fig. 25(c)). The two peaks in the distortion curve correlate with conditions where the vortex core was crossing over a probe. In this case the pressures near the duct tip were greater due to the lower corrected airflow, and the vortex probably passed more directly over the probes causing a lower recorded pressure from the core pressure defect.

Vortex Properties

Flow properties of the vortex as obtained from surveys using the three-dimensional flow-angularity rake are presented herein. Data from surveys of the two-dimensional flow-angularity rake are presented in reference 1.

Surveys of the vortex in front of the inlet were obtained with the vortex rotating counterclockwise (fig. 26). Figures 26(a), (b), and (c) present the measured spanwise, normal, and tangential velocity profiles. The tangential (or rotational) velocity of the vortex was assumed to be the total velocity measured perpendicular to the axial velocity. As with previous investigations of velocity distributions in trailing vortices these measurements were made with a steady-state data scan at each probe (or rake) location. Because of the tendency of the vortex to meander as reported in reference 12, this technique results in measured velocities that are time averaged. Thus the measured peak velocities would be somewhat low.

Figures 26(d) and (e) present the total- and static-pressure profiles obtained from the vortex survey and figure 26(f) presents the axial velocity profiles which were computed assuming no total temperature variation. But total temperature gradients do exist in swirling flow. Lower total temperatures exist within the vortex core as a result of the flow curvature (ref. 13). One example of this is the energy separation observed in the Ranque-Hilsch tube (ref. 13). Because temperature variations are difficult to measure, other investigators also ignore temperature gradients. Hot wire surveys such as found in reference 12 use King's law which ignores both temperature and density gradients.

Surveys of the vortex at the compressor face are illustrated by figures 27 and 28. These figures present the surveys made at the lowest engine corrected airflow and are typical of those at higher airflows. Vortex properties are presented in the same order as in figure 26. Also each figure shows the approximate path of the ingested vortex as the inlet was pitched to vary h/H. With the ingested vortex rotating counterclockwise (fig. 27), the vortex crossed the flow angularity rake centerline near the hub end probe at an l/L of 0.17 and an h/H of 0.373. Because of the nonsymmetrical position of the flow angularity rake relative to the vortex paths of the opposite rotating vortices, the clockwise vortex crossed the flow angularity rake centerline farther from the hub at an l/L of 0.29 and an h/H of 0.278 (fig. 28). These rake-crossing positions were very close to those observed at the other corrected airflows.

The total- and static-pressure profiles across the vortex appear to be symmetrical with the vortex center (parts (d) and (e) of figs. 26 to 28). (The core center was determined from the spanwise and normal velocity profiles and its position is shown on each figure.) The axial velocity seems less symmetrical about the vortex center in front of the inlet (fig. 26(f)) than at the compressor face (figs. 27(f) and 28(f)).

In an ideal situation, measurements into a vortex core would include conditions at the exact core center. Such measurements can be made with a single translating probe but are a matter of chance with a rake of probes such as used herein where the rake is either fixed or translatable in a single plane. In none of the vortex surveys conducted with the flow-angularity rake did a probe cross directly over the vortex center where the minimum values of pressure and axial velocity were expected. With the rake surveys at the compressor face, a probe always passed within 0.08 core diameter of the vortex center and the recorded values were probably quite close to the core center values. With the rake in front of the inlet, a probe crossed the core at 0.15 core diameter from the center. In order to assess the measured minimum values, cross plots (not shown) of the static and total pressures were made across the core center ($y/c = -0.3$) and faired to the center. The plots indicated that the total pressure at the core center was about 2 percent less than the measured minimum and the static pressure about 1 percent less. Core center axial velocity computed from the faired plots was no lower than the measured minimum value. Thus all measured minimum values appear to be reasonably representative of the core center values.

Vortex properties are summarized in figure 29 which presents the results of the flow angularity rake surveys in front of the inlet ($x/c = 7.03$) and at the compressor face ($x/c = 17.5$).

Prior to entering the inlet, the vortex core diameter was 14 percent of the wing tip chord length and the vortex maximum tangential velocity was 51 percent of the free-stream velocity (fig. 29(a-1) and (a-2)). Farther downstream at the compressor face the core had enlarged to about 18 percent of the wing tip chord length and the maximum tangential velocity had fallen to about 30 percent of the average axial velocity at that station (fig. 29(b-1) and (b-2)). These trends of a growing core diameter and a decreasing tangential velocity with increasing distance aft of the wing are typical vortex characteristics (refs. 9, 12, and 14). Reference 12 suggests that these trends are linked by a relation between the core diameter and the maximum tangential velocity. Data of reference 12 indicate that the product of the core diameter and the maximum tangential velocity is constant. This implies that the circulation within the core is constant. The product of these values are presented in figure 29(a-3) and (b-3). These data suggest that the circulation was reduced at the downstream location of the compressor face; probably as a result of inlet interference with the vortex flow field. The data also suggest two other effects. Increased flow spillage over the cowl lip at reduced mass-flow ratios decreased the circulation. And a close encounter of the vortex core with the engine hub (vortex at $l/L \approx 0.17$) may have reduced circulation.

The total-pressure defect within the vortex core (a function of wing profile drag, ref. 15) was measured in front of the inlet by the flow angularity rake and found to have a maximum value of 9.5 percent (fig. 29(a-4)). The maximum measured static pressure defect was 10 percent (fig. 29(a-5)). The magnitudes of these defects were reduced farther downstream at the compressor face; with the maximum total-pressure defect averaging about 5 percent (fig. 29(b-4)) and the maximum static-pressure defect about 3 percent (fig. 29(b-5)). These trends in pressure defect are similar to those observed in a vortex trailing undisturbed from a wing where vortex properties tend toward free-stream conditions with distance aft of the wing. The maximum total-pressure defect recorded at the compressor face seemed to vary with vortex location. When the vortex was nearest the engine hub ($l/L \approx 0.17$), the maximum defect was 2 percent greater than the maximum defect measured when the vortex was farther from the hub. In addition to reduced circulation, this may be an additional effect of hub interference with the vortex core flow.

Axial velocity variations across a wing tip vortex core can be either greater or less than the free-stream velocity depending on the ratio of profile drag to induced drag (ref. 15). The wing used in this study produced a vortex core axial velocity less than free-stream velocity. The maximum axial velocity defect measured in front of the inlet ($x/c = 7.03$) was about 7 percent (fig. 29(a-6)). References 9 and 14 report core axial velocity defects that grow smaller with increasing distance aft of the wing. Reference 12, however, reports no change with axial distance. In the present study the maximum core axial velocity defect measured at the downstream location ($x/c = 17.5$) was about the same as the defect measured upstream when the vortex was away from the engine hub at an l/L of about 0.29 (fig. 29(b-6)). When the vortex was near the hub ($l/L \approx 0.17$), the maximum axial velocity defect was greater than the defect measured upstream, reaching values as high as 23 percent. These larger defects were probably a result of the larger total pressure defects resulting from hub interference with the core flow. The data of figure 29(b-6) also suggest that lowering the inlet mass-flow ratio, thereby spilling increased flow over the cowl and decreasing the compressor-face flow velocity, increased the vortex core axial velocity defect.

Effect of Ingested Vortex on Engine Stall Margin

Stall margin losses caused by the ingested vortex are presented in figure 30 as losses in stall compressor pressure ratio at a constant corrected engine speed plotted against the ingested vortex vertical position parameter h/H. These losses were computed from the vortex stall data of reference 2 and a reference stall line obtained with undistorted inflow to the same engine in a connected pipe test (ref. 6). The data of both references 2 and 6 were obtained with the same inlet guide vane and compressor interstage bleed schedules. An engine overhaul occurred between the two sets of data.

In reference 2 the engine was operated up to the pressure ratio causing stall or the turbine temperature limit at three nominal corrected airflows. These vortex ingestion data are somewhat lacking in completeness due to the fact that, at the higher and lower corrected airflows, the turbine temperature limit prevented engine operation up to the pressure ratios of the undistorted inflow stall line. Turbine temperature limits are shown in figure 30 as tailed symbols. At the higher corrected airflows, stall sometimes occurred below the temperature limit adding to the data completeness; but at the lower corrected airflows stalls were never obtained. The maximum corrected airflow was limited to 18 kilograms per second because higher airflows would have required the engine to exceed its rated mechanical speed when operated near the undistorted inflow stall line.

Although the basic stall data of reference 2 were obtained at constant corrected airflows to keep the vortex at a constant duct location, the loss in stall pressure ratio was computed along a line of constant corrected engine speed rather than constant corrected airflow.

Also presented in figure 30 are the predicted losses in stall compressor pressure ratio due to the total-pressure distortion at the compressor face. These losses were computed from the measured compressor face total-pressure profiles at each condition using a method developed in reference 16. This was a connected pipe test in which tip radial, hub radial, and circumferential distortion patterns were induced at the compressor face by various porosity screen patterns. Correlating parameters based on parallel compressor theory were developed from these distortion data to predict the losses in stall pressure ratio resulting from the distortions. In these predictions, reference 16 accepted a scatter band in the predicted loss in stall pressure ratio of ±0.02.

In applying the method of reference 16 to the current data, the known vortex core total-pressure defect was taken into account when not affecting a rake to augment the standard compressor face total-pressure rake data. Predicted losses in stall pressure ratio were computed from the augmented tip radial, hub radial, and circumferential distortion patterns and the largest predicted losses are shown in figure 30.

Large losses in stall compressor pressure ratio were caused by the ingestion of the wing tip vortex (fig. 30). The maximum loss in stall pressure ratio caused by the ingested vortex rotating counter to the engine was larger than the maximum loss in stall pressure ratio caused by the vortex rotating with the engine. When the vortex rotated counter to the engine, the maximum loss in stall pressure ratio, over and above that attributable to distortion, ranged from 0.043 to 0.052 at the mid to high corrected airflows (figs. 30(a) and (b)); whereas when the vortex rotated with the engine rotation, the maximum loss in stall pressure ratio not attributable to distortion ranged from 0.17 to 0.19 at the mid to high corrected airflows. A better perspective of the significance of these numbers is gained by the realization that the 0.052 loss in stall pressure ratio represents a stall pressure ratio that was 28 percent nearer to the nominal normal operating line (along a line of constant corrected speed) than the stall pressure ratio attainable with the equivalent total-pressure distortion alone. The 0.019 loss in stall pressure ratio caused by the vortex rotating with the engine represents a point 11 percent nearer to the nominal normal operating line than the stall pressure ratio attainable with distortion alone.

At the lower engine corrected airflow where no stalls were obtained the turbine temperature limit line in figure 30(c) indicates that the loss in stall pressure ratio could not have exceeded about 0.03; roughly half of the maximum loss in stall pressure ratio incurred at the higher corrected airflows with the vortex rotating counter to the engine; but about the same as the maximum loss in stall pressure ratio incurred at the higher corrected airflows with the vortex rotating with the engine (fig. 30(a) and (b)). Because of the different stall results between the higher and lower engine corrected airflows it seems that the vortex induced stall characteristics of the engine changed considerably at lower airflows.

Figure 31 presents a correlation of the ingested vortex vertical position parameter with the measured radial position of the vortex at the compressor face. The radial positions of the vortex were obtained from the data used to construct the vortex path shown in figure 18(b). Because of the path similarities noted earlier in this report the radial positions shown in figure 31 are representative of those at any tested engine condition for either vortex rotational direction.

It is clear from figures 30 and 31 that, when the ingested vortex was rotating counter to the engine rotation, the maximum loss in stall compressor pressure ratio occurred at the higher corrected airflows when the vortex was located near the engine hub. When the vortex rotated with the engine rotation the maximum loss in stall pressure ratio occurred again at the higher corrected airflows but the vortex was approximately midway between the hub and tip on the cowl side of the duct. These conditions are the only ones where the stall data in figure 30 are outside of the 0.02 scatter band of the computed loss in stall pressure ratio due to distortion. Thus these stalls were probably not caused by total-pressure distortion. Indeed, the distortions presented in figure 25 did not correlate in any way with the observed losses in stall pressure ratio (fig. 30). In addition, the compressor face total-pressure profiles, as previously noted, revealed that at each ingested vortex position the profiles obtained with opposite rotating vortices were, with small variations, mirror images of each other. These facts, coupled with the above dissimilar effects of vortex rotational direction on stall, make it clear that no interpretation of the total-pressure variations across the compressor face could correlate them with the observed losses in stall compressor pressure ratio.

The stall effects reported herein must then be dependent on the rotational properties of the vortex. The data of figure 30 not only show an effect of vortex rotational direction on the loss in stall pressure ratio but also that the vortex position at the compressor face greatly influenced the loss in stall pressure ratio. However, the dissimilar position effects of the clockwise and counterclockwise vortices strongly suggest that the effect of vortex position alone cannot be interpreted without also considering the influence of the rotational direction of the vortex and its effects on the engine.

The probable streamline of the vortex maximum rotational (or tangential) velocity as it expanded and wrapped around the engine hub when the vortex was located near the hub is shown in sketch (b).

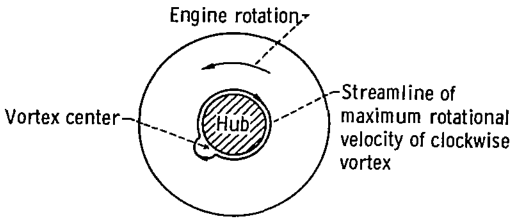

(b)

The resulting large rotational velocities near the hub and totally around its circumference explain the large loss in stall pressure ratio that occurred when the vortex was near the hub and rotating counter to the engine. With such a condition fluid rotational velocities would appear to the compressor blades as a continual large increase in angle of attack near the hub and thereby increase the likelihood of stall.

SUMMARY OF RESULTS

A two-dimensional inlet was placed in a Mach 0.4 stream in the Lewis 10- by 10-Foot Supersonic Wind Tunnel so as to ingest the tip vortex of a wing mounted at a forward location in the test section. The inlet was alternately mated to a coldpipe plug assembly and a turbojet engine. Prior to measurements at the compressor face, the vortex was surveyed with a rake of flow angularity probes located just forward of the inlet ramp leading edge. Wing angle of attack was selected to produce the maximum vortex strength, and positive and negative angles were utilized to generate vortices that rotated with and counter to the direction of engine rotation. Inlet angle of attack variation was used to cause vortex ingestion to occur at selected vertical locations across the inlet entrance. To detect the vortex within the inlet, a rake of flow angularity probes was mounted at a fixed location at the compressor face. The effects of the vortex on compressor face total pressures, distortion, and the stall margin of the J85-GE-13 turbojet engine were determined.

The effects of the ingested vortex on engine stall margin are as follows:

1. With the ingested vortex rotating opposite to the engine rotation, a major reduction in engine stall margin (stall pressure ratio) was obtained only when the vortex was located near the hub. In this case the engine stalled at a compressor pressure ratio that was closer to the normal operating line than the predicted stall pressure ratio attainable with distortion alone by as much as 28 percent along a line of constant corrected speed.

2. With the vortex and engine rotating in the same direction, the maximum loss in stall pressure ratio was smaller and occurred when the vortex was located on the cowl side of the duct about midway between the hub and tip. The stall pressure ratio was as

much as 11 percent closer to the normal operating line than the predicted stall pressure ratio attainable with distortion alone.

3. The loss in stall pressure ratio induced by the ingested vortex did not correlate with any interpretation of the total-pressure variations across the compressor face; including total-pressure distortion and the predicted loss in stall pressure ratio due to distortion.

The effects of the ingested vortex at the compressor face are as follows:

1. The core of the ingested vortex was small enough that its total-pressure loss was not always sensed by the compressor face total-pressure rakes.

2. Total pressures away from the core at other locations across the compressor face were also altered when the vortex was ingested. The changes in pressures from vortex-free to vortex-ingested flow was least at the lowest engine corrected airflow. At a corrected airflow higher than available with the engine, coldpipe data revealed the ability of the ingested vortex to improve compressor face flow by energizing and almost eliminating a large region of retarded flow. Vortex ingestion increased the compressor face total-pressure distortion 1 to 2 percent at the higher engine corrected airflows and up to 1 percent at the lower airflows.

Vortex characteristics are as follows:

1. The strongest vortex was produced by the wing at 11° angle of attack. Prior to entering the inlet, the vortex had a maximum tangential velocity of 51 percent of free-stream velocity and a core diameter of 14 percent of the wing tip chord. Core total- and static-pressure defects were each about 10 percent. Axial velocity defect in the core was 7 percent.

2. At the compressor face the vortex maximum tangential velocity had decayed to about 30 percent based on the average compressor face velocity and the core was enlarged to about 18 percent of the wing tip chord. Total-pressure defect was about 5 percent, and static-pressure defect about 3 percent. Axial velocity defect was about the same order of magnitude as the defect measured in front of the inlet except when the vortex was near the hub where a defect as large as 23 percent was measured.

3. The initial path of the vortex as it trailed aft from the wing was in good agreement with paths noted by other investigators. In the vicinity of the inlet the vortex path was changed from that expected in undisturbed flow and varied with the amount of airflow that was deflected and spilled by changes in mass-flow ratio.

4. The vortex path from the inlet entrance to the compressor face displayed large lateral displacements when the vortex core was located near an inlet surface.

Lewis Research Center,
National Aeronautics and Space Administration,
Cleveland, Ohio, February 12, 1975,
505-11.

APPENDIX - SYMBOLS

b	wing span, cm
c	wing tip chord, cm
d	vortex core diameter, cm
H	vertical distance from cowl lip to ramp leading edge, cm
h	vertical distance from cowl lip to initial position where vortex impinged on cowl lip, cm
L	compressor face hub to tip distance along flow angularity rake, cm
LSPR	loss in stall compressor pressure ratio. $\left\{1 - \left[(\overline{P}_3/\overline{P}_2)_{iv}/(\overline{P}_3/\overline{P}_2)_u\right]\right\}_{N/\sqrt{\theta}=\text{const}}$
l	distance from compressor face hub along flow angularity rake, cm
N	engine speed, rpm
P	total pressure, N/m^2
p	static pressure, N/m^2
T	total temperature, K
U_0	free-stream velocity, m/sec
u_x	velocity in axial direction, m/sec
$u_{x'}$	axial velocity parallel to compressor face axis, m/sec
u_y	velocity in spanwise direction, m/sec
$u_{y'}$	spanwise velocity perpendicular to compressor face axis, m/sec
u_z	velocity in normal direction, m/sec
u_θ	total velocity perpendicular to axial velocity, $\sqrt{(u_y)^2 + (u_z)^2}$, m/sec (assumed to represent vortex tangential or rotational velocity)
$u_{\theta'}$	total velocity perpendicular to compressor face axis, $\sqrt{(u_{y'})^2 + (u_z)^2}$, m/sec (assumed to represent vortex tangential or rotational velocity)
u_2	average compressor face axial velocity, m/sec
W	engine airflow, kg/sec
W_{corr}	engine corrected airflow, $W\sqrt{\theta/\delta}$, kg/sec
x	streamwise (axial) ordinate, aft from wing tip trailing edge
y	spanwise ordinate, outboard from wing tip

z	normal ordinate, above upper wing surface from wing tip trailing edge
α	inlet angle of attack
δ	local corrected total pressure, P/101 325 $\mathrm{N/m^2}$
θ	local corrected total temperature, T/288.2 K

Subscripts:

iv	compressor stall point with ingested vortex
loc	local conditions outside vortex core
min	minimum
u	undistorted inflow compressor stall point
0	free stream
2	compressor face station
3	compressor-discharge station

REFERENCES

1. Mitchell, Glenn A.: Preliminary Investigation of Inlet Ingestion of a Wing Tip Vortex. NASA TM X-68225, 1973.
2. Mitchell, Glenn A.: Effect of Inlet Ingestion of a Wing Tip Vortex on Turbojet Stall Margin. NASA TM X-71610, 1974.
3. Coltrin, Robert E.; and Choby, David A.: Steady-State Interactions from Mach 1.98 to 2.58 Between a Turbojet Engine and an Axisymmetric Inlet with 60-Percent Internal Area Contraction. NASA TM X-1780, 1969.
4. Choby, David A.; Burstadt, Paul L.; and Calogeras, James E.: Unstart and Stall Interactions Between a Turbojet Engine and an Axisymmetric Inlet with 60-Percent Internal Area Contraction. NASA TM X-2192, 1971.
5. Dudzinski, Thomas J.; and Krause, Lloyd N.: Flow-Direction Measurement with Fixed-Position Probes. NASA TM X-1904, 1969.
6. Calogeras, James E.; Johnsen, Roy L.; and Burstadt, Paul L.: Effect of Screen-Induced Total-Pressure Distortion on Axial Flow Compressor Stability. NASA TM X-3017, 1974.
7. Fage, A.; and Simmons, L. F. G.: An Investigation of the Air-Flow Pattern in the Wake of an Aerofoil of Finite Span. Phil. Trans. Roy. Soc. (London), ser. A, vol. 225, no. 632, Dec. 7, 1925, pp. 303-330.
8. Dosanjh, D. S.; Gasparek, E. P.; and Eskinazi, S.: Decay of a Viscous Trailing Vortex. Aero. Quart., vol. 13, pt. 2, May 1962, pp. 167-188.
9. Chigier, N. A.; and Corsiglia, V. R.: Wind-Tunnel Studies of Wing Wake Turbulence. J. Aircraft, vol. 9, no. 12, Dec. 1972, pp. 820-825.
10. Pearcy, H. H.: Shock Induced Separation and Its Prevention by Design and Boundary Layer Control. Boundary Layer and Flow Control. Vol. 2, Gustav V. Lachman, ed., Pergamon Press, 1961, p. 1283.
11. Mitchell, Glenn A.; and Davis, Ronald W.: Performance of Centerbody Vortex Generators in an Axisymmetric Mixed-Compression Inlet at Mach Numbers from 2.0 to 3.0. NASA TN D-4675, 1968.
12. Corsiglia, V. R.; Schwind, R. G.; and Chigier, N. A.: Rapid Scanning, Three-Dimensional, Hot-Wire Anemometer Surveys For Wing Tip Vortices in the Ames 40- by 80-Foot Wind Tunnel. AIAA Paper 73-681, July 1973.
13. Hall, M. G.: The Structure of Concentrated Vortex Cores. Progress in Aeronautical Sciences. Volume 7, D. Kucheman, ed., Pergamon Press, 1966, pp. 53-110.

14. Kuhn, Gary D.; and Nielsen, Jack N.: Analytical Studies of Aircraft Trailing Vortices. AIAA Paper 72-42, Jan. 1972.

15. Brown, Clinton E.: On the Aerodynamics of Wake Vortices. TR-7115, Hydronautics, Inc. (AFOSR-72-1209TR; AD-744860), May 1972.

16. Calogeras, James E.; and Burstadt, Paul L.: Formulation of a Distortion Index Based on Peak Compressor Pressure Ratios. NASA TM X-71568, 1974.

TABLE I. - STANDARD ERROR IN FLOW
PROPERTIES DETERMINED FROM
THREE-DIMENSIONAL FLOW
ANGULARITY PROBES

Flow property	Standard error
Flow angle normal to rake, deg	2
Flow angle parallel to rake, deg	2
Total pressure	0.5 Percent
Static pressure	1.0 Percent
Axial velocity	4 Percent
Tangential velocity	4 Percent

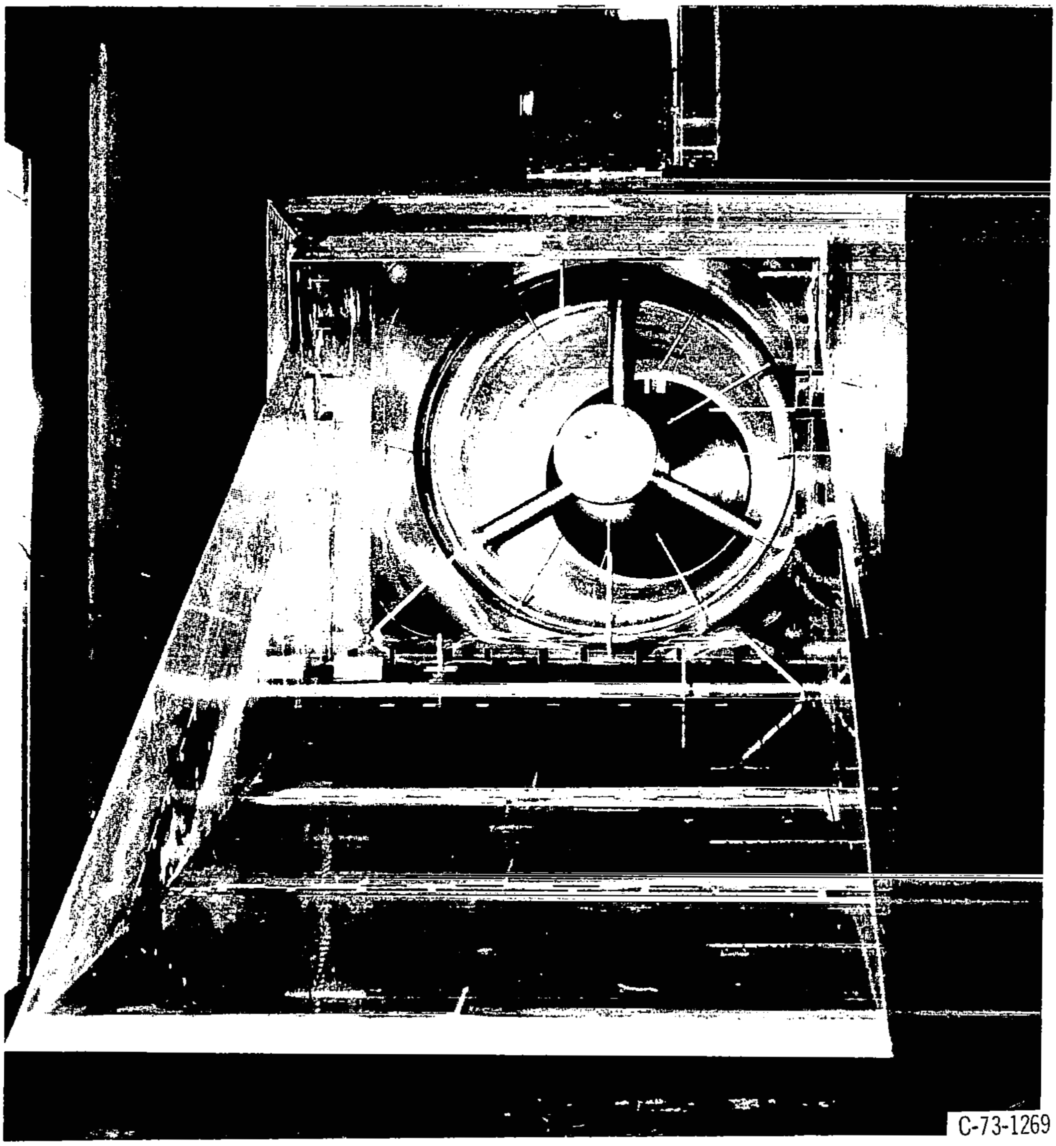

Figure 1. - Inlet model installed in 10- by 10-Foot Supersonic Wind Tunnel.

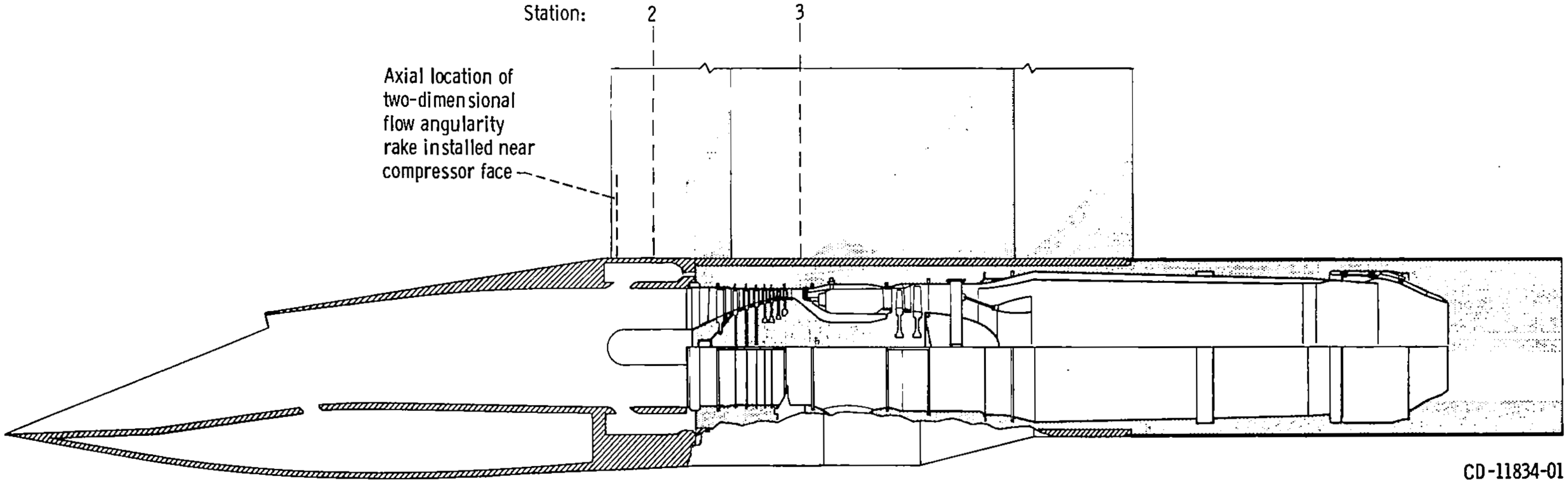

Figure 2. - Cutaway of nacelle showing installation of J85-GE-13 turbojet engine.

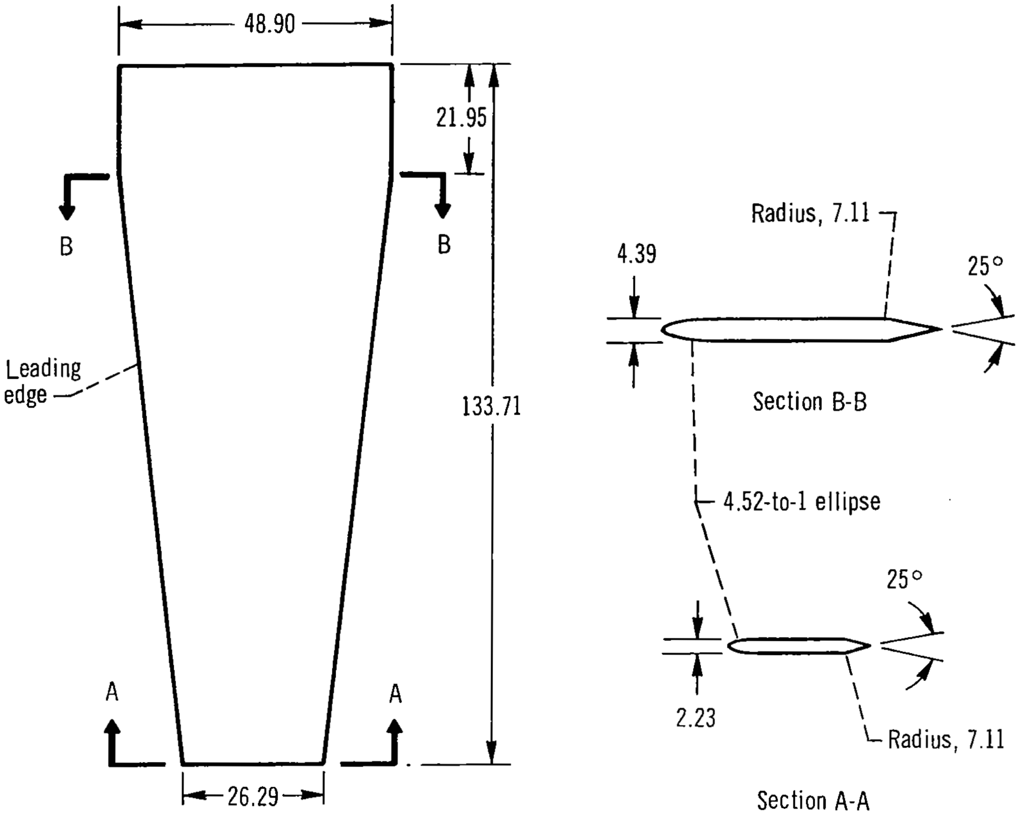

Figure 3. - Details of wing. (All dimensions are in cm unless indicated otherwise.)

C-73-1272

Figure 4. - Wing and inlet installed in 10- by 10-Foot Supersonic Wind Tunnel.

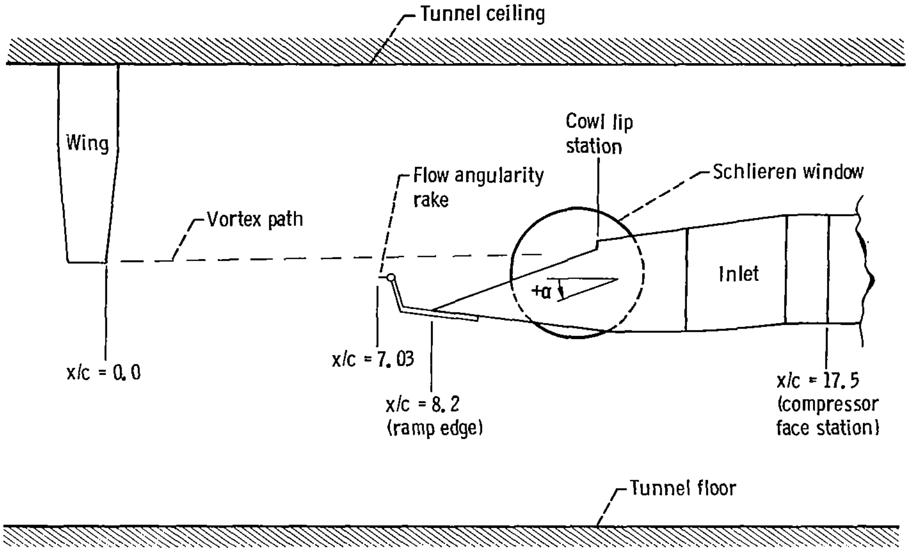

Figure 5. - Schematic of test setup.

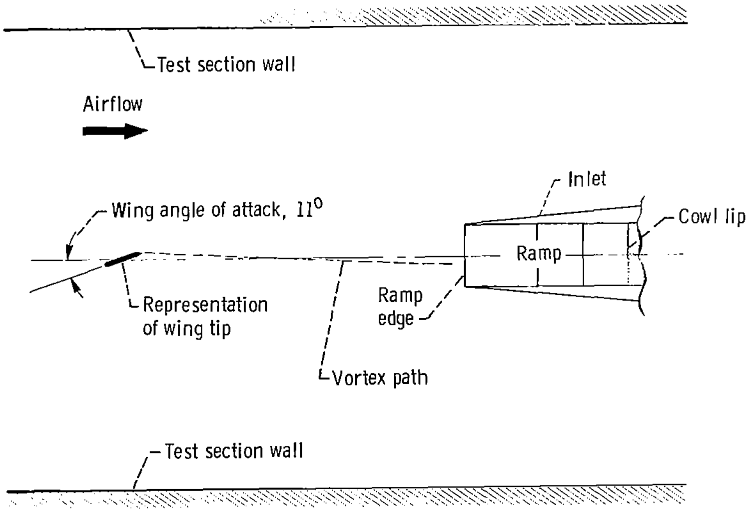

Figure 6. - Plan view of test setup.

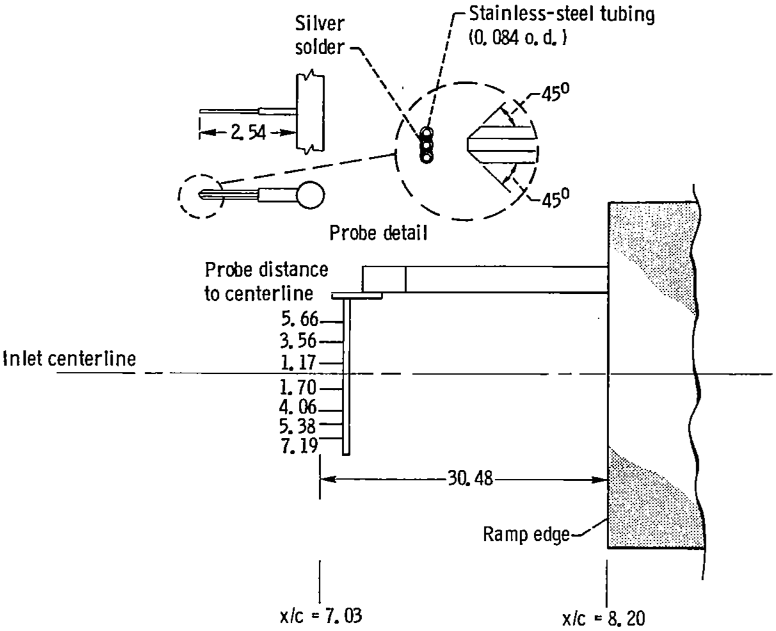

Figure 7. - Plan view of two-dimensional flow angularity rake installed in front of inlet. (All dimensions in cm unless indicated otherwise.)

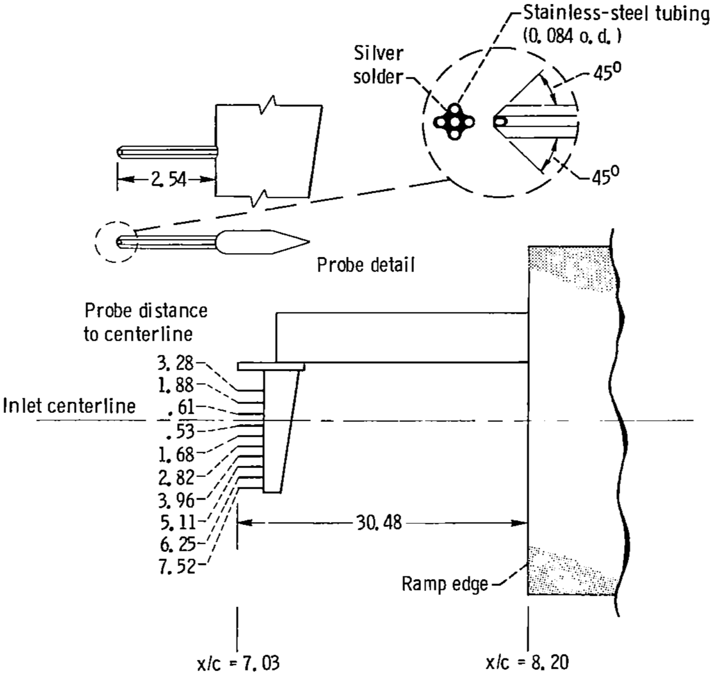

Figure 8. - Plan view of three-dimensional flow angularity rake installed in front of inlet. (All dimensions in cm unless indicated otherwise.)

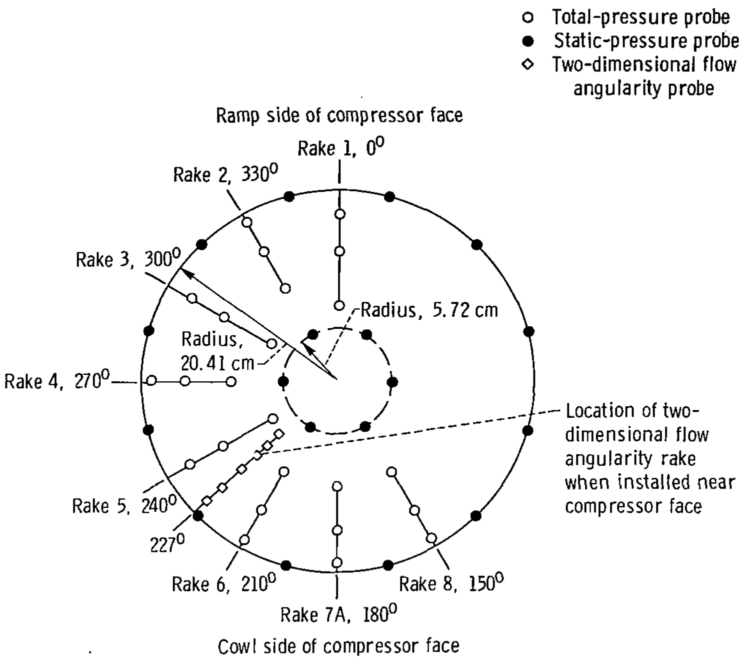

Figure 9. - Compressor face instrumentation with cold pipe installed, looking downstream and inverted from testing orientation of figure 1.

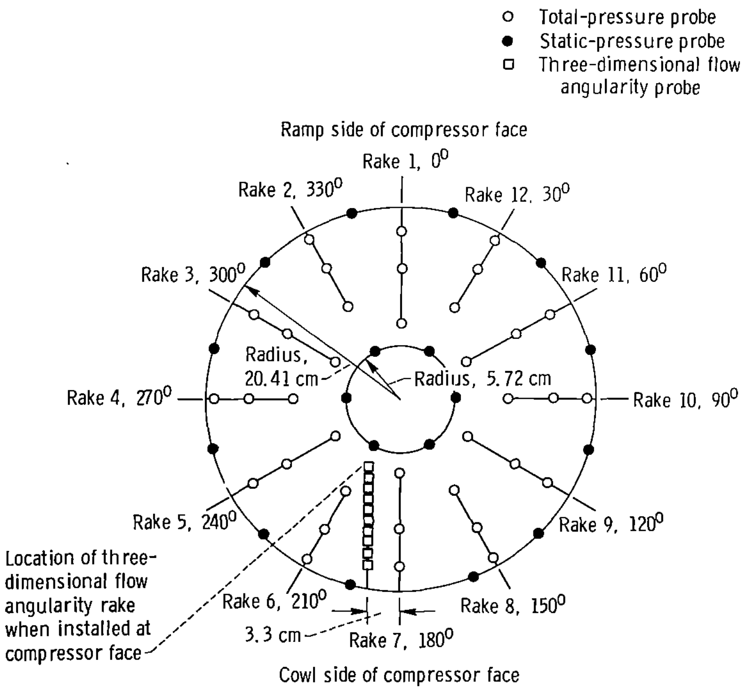

Figure 10. - Compressor face (station 2) instrumentation with engine installed, looking downstream and inverted from testing orientation of figure 1.

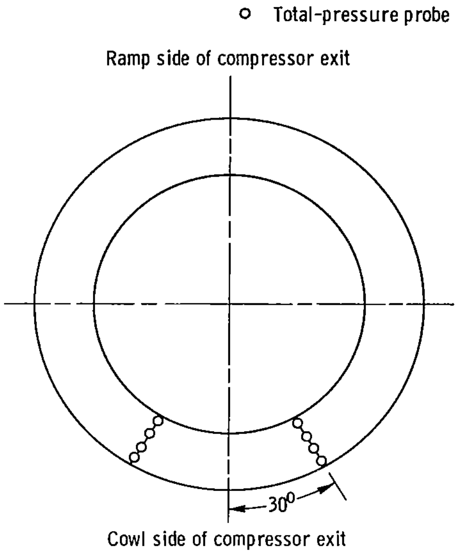

Figure 11. - J85-GE-13 engine compressor exit (station 3) instrumentation.

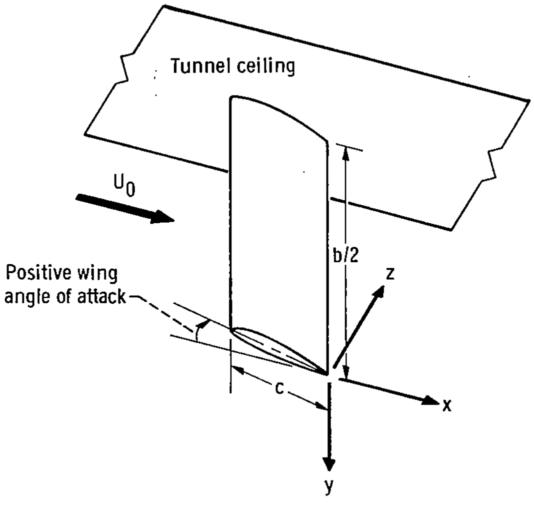

Figure 12. - Geometry and coordinate system.

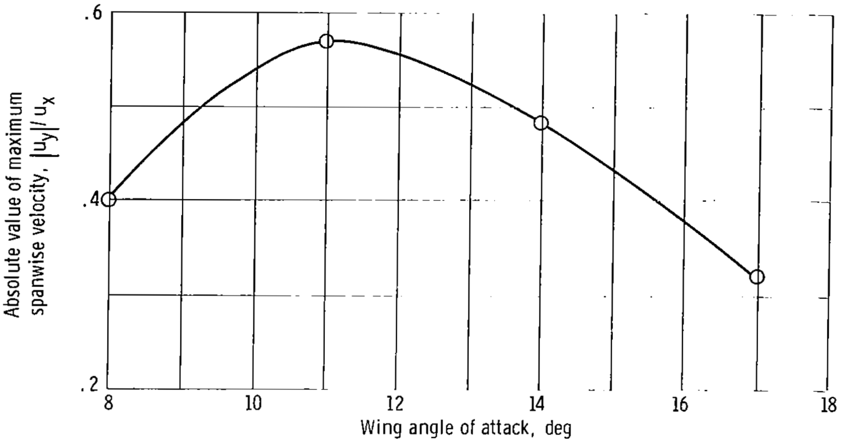

Figure 13. - Maximum spanwise velocity measured in vortex with two-dimensional rake as function of wing angle of attack. Axial distance from wing tip trailing edge $x/c = 7.03$.

	Air-foil	Semi-span, cm	Tip chord, cm	Angle of attack, deg	Estimated core diameter at $x/c \approx 7$	Data source
○	See fig. 3	133.7	26.3	11	0.14 c	Present test
□	R. A. F. 6a	91.5	15.2	6	.15 c	Rectangular wing from ref. 7
△	NACA 0009	26.7	7.6	8	.24 c	Rectangular wing from ref. 8
◇	NACA 0015	121.8	45.7	12	.10 c	Rectangular wing from ref. 9

Upward tailed symbols denote three-dimensional rake
Downward tailed symbols denote two-dimensional rake

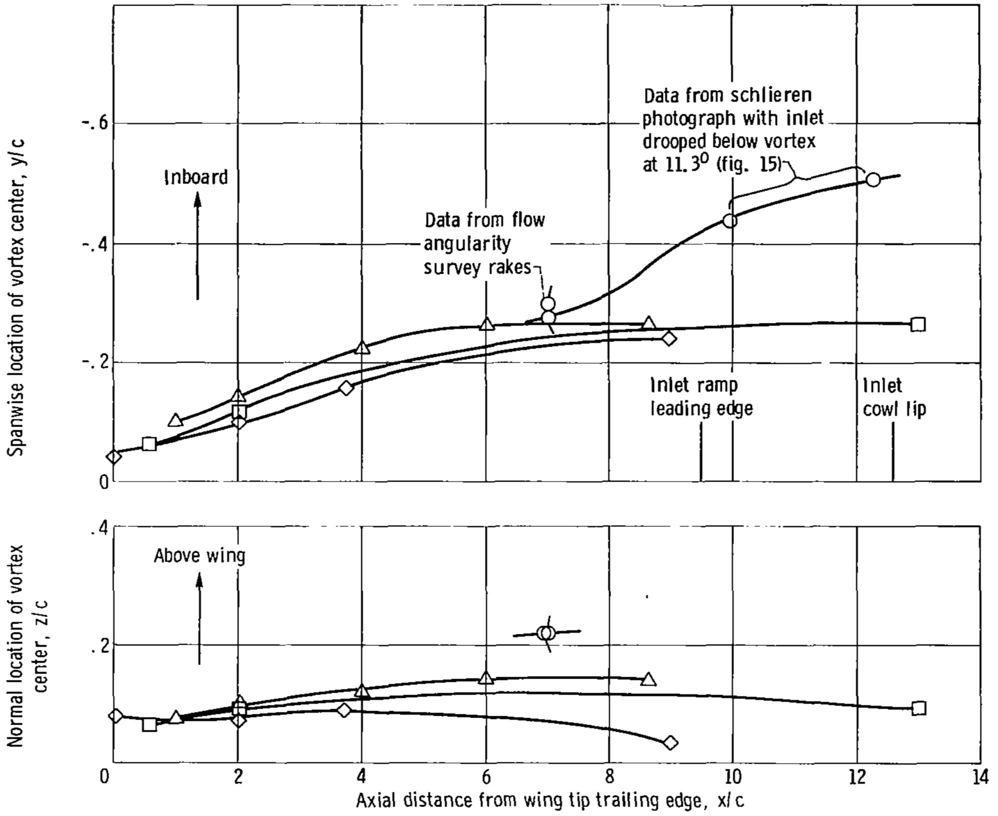

Figure 14. - Spanwise and normal location of vortex centerline as function of axial distance.

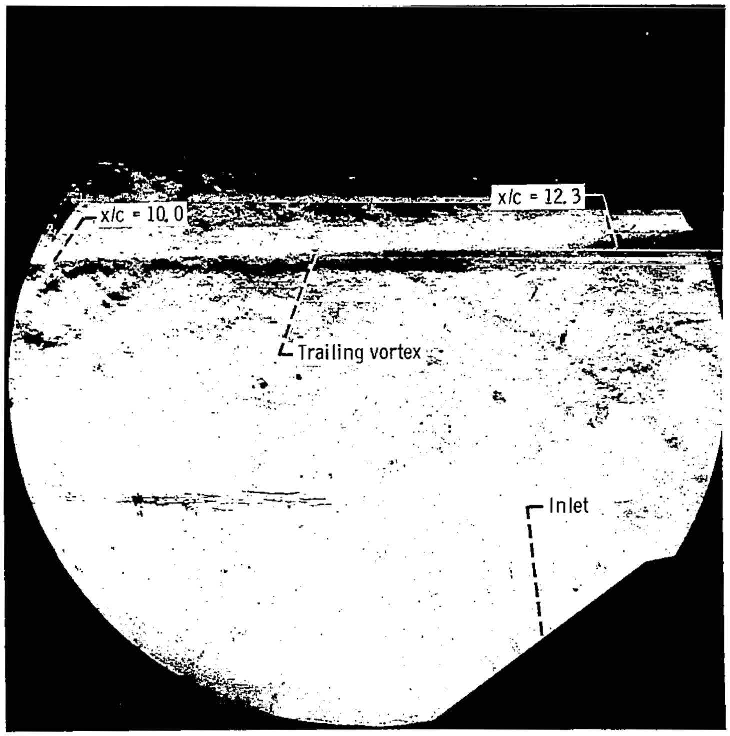

Figure 15. - Schlieren photograph of vortex trailing aft from wing tip. Spanwise position of inlet centerline at ramp edge station y/c = 2.8; inlet angle of attack α = 11.3°; wing angle of attack, 11°.

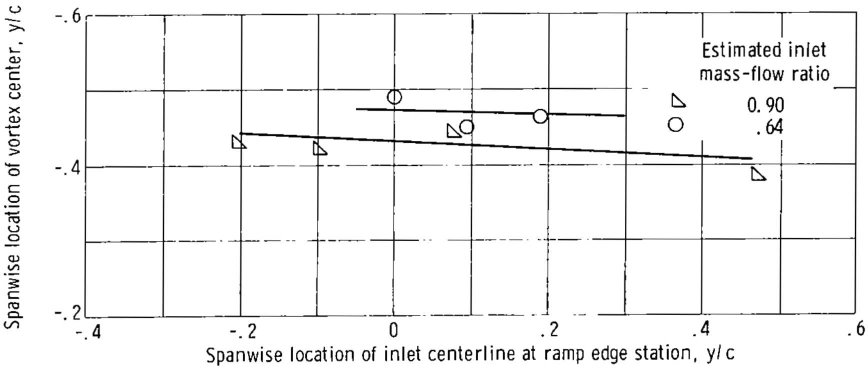

Figure 16. - Effect of spanwise inlet location on spanwise location of vortex at axial location x/c = 10.0; wing angle of attack, 11°.

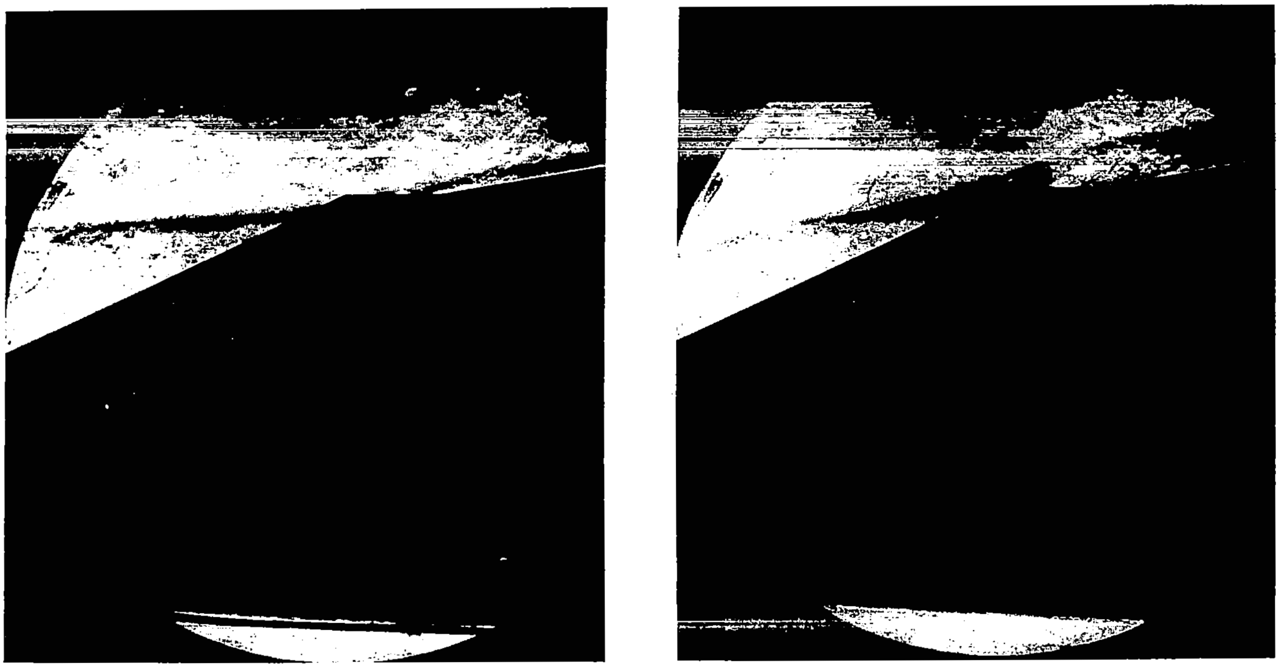

(a) Estimated inlet mass-flow ratio, 0.64.

(b) Estimated inlet mass-flow ratio, 0.54.

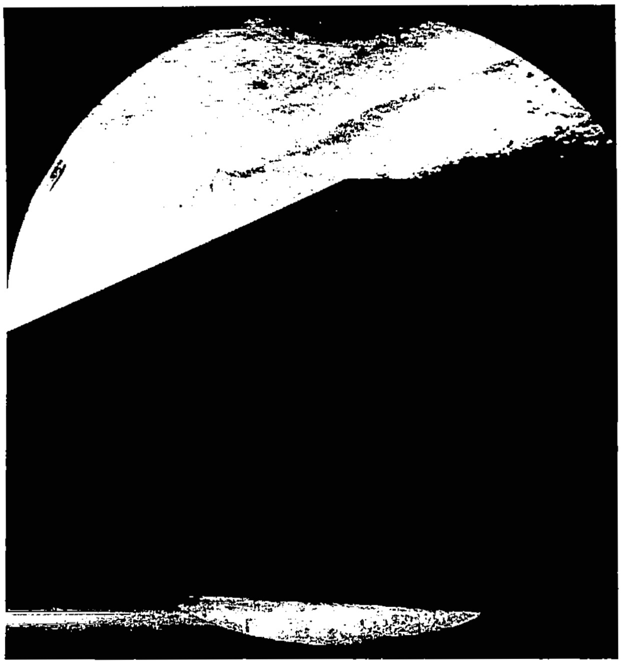

(c) Estimated inlet mass-flow ratio, 0.27.

Figure 17. - Schlieren photographs showing effect of inlet mass-flow ratio on vortex path. Spanwise position of inlet centerline at ramp edge station $y/c = 0.189$; inlet angle of attack $\alpha = -0.26^{\circ}$; wing angle of attack, 11°.

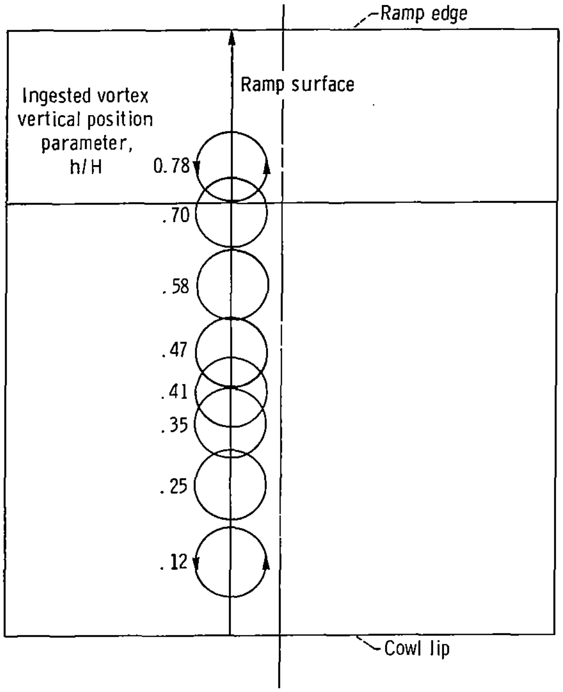

(a) Location of vortex at inlet entrance.

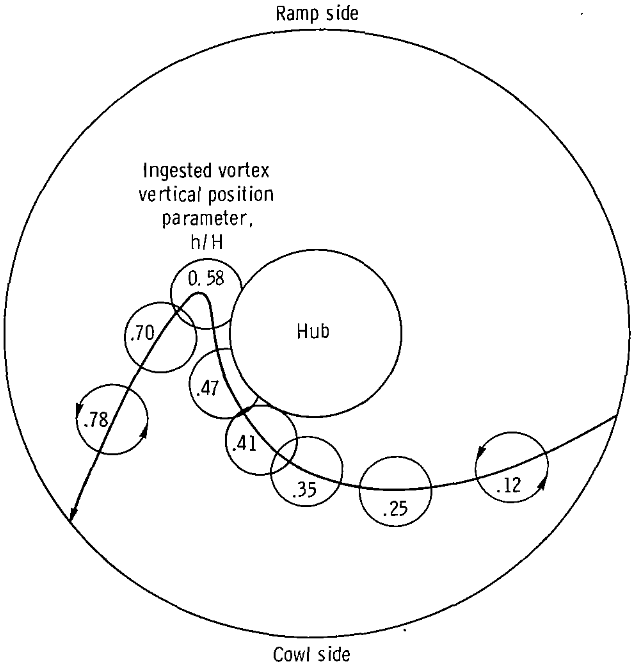

(b) Location of vortex at compressor face.

Figure 18. - Path of counterclockwise vortex. Nominal engine corrected airflow, 18 kilograms per second; nominal inlet mass-flow ratio, 0.76.

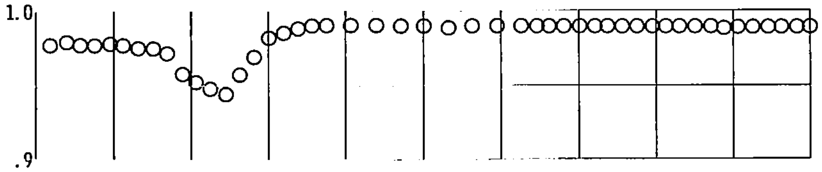

(a) Rake 8, hub probe.

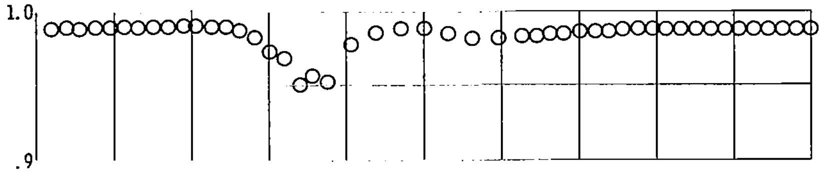

(b) Rake 7, hub probe.

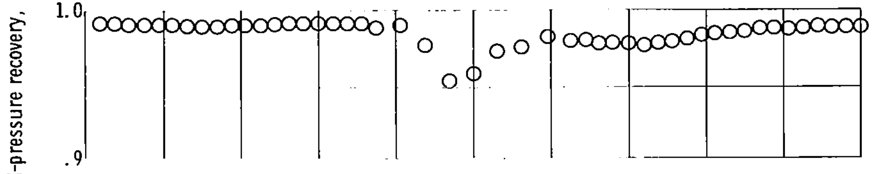

(c) Rake 5, hub probe.

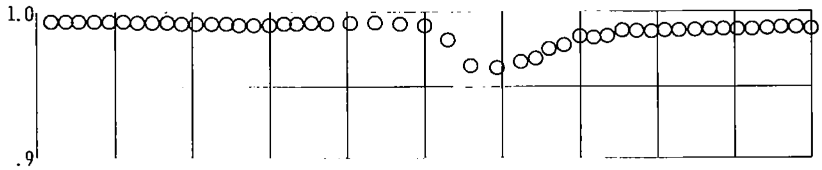

(d) Rake 3, hub probe.

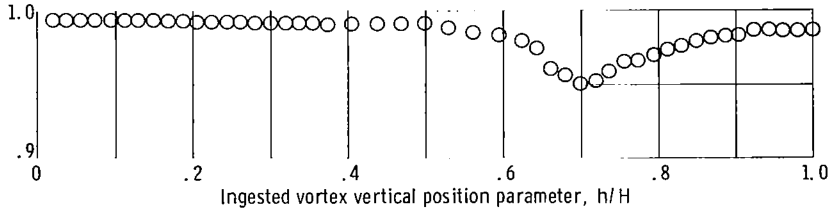

(e) Rake 4, hub probe.

Figure 19. - Vortex passage recorded by selected compressor face total-pressure probes. Nominal engine corrected airflow, 18 kilograms per second; nominal inlet mass-flow ratio, 0.76; wing angle of attack, 11° (counterclockwise vortex).

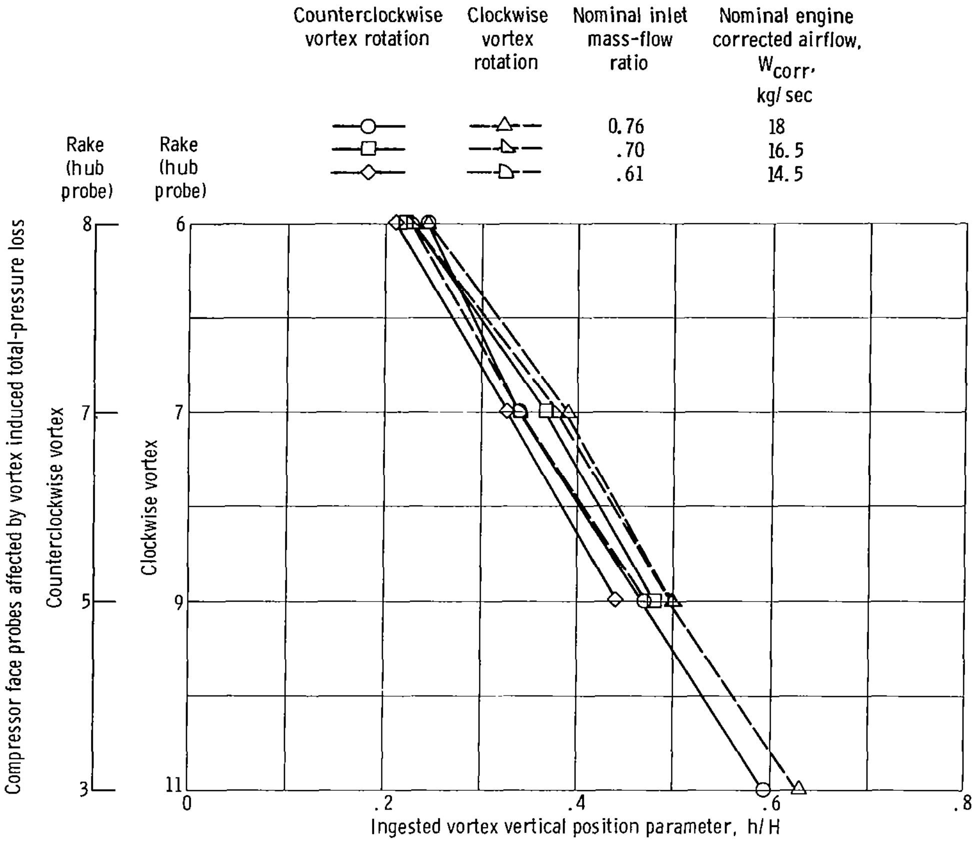

Figure 20. - Vortex position determined by maximum total-pressure loss of compressor face probes.

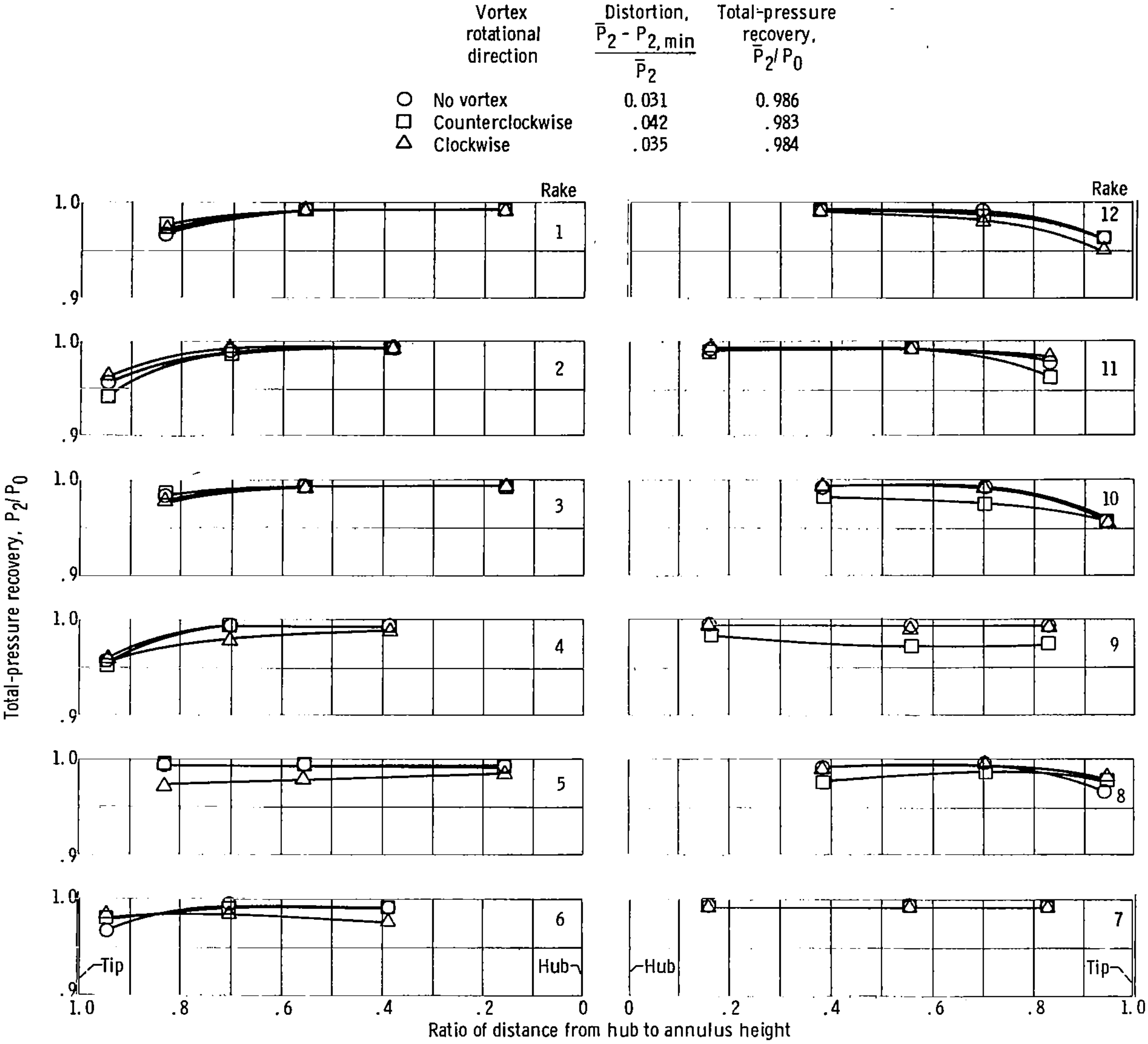

(a) Ingested vortex vertical position parameter h/H = 0.150.

Figure 21. - Compressor face total-pressure profiles. Nominal engine corrected airflow, 18 kilograms per second; nominal inlet mass-flow ratio, 0.76.

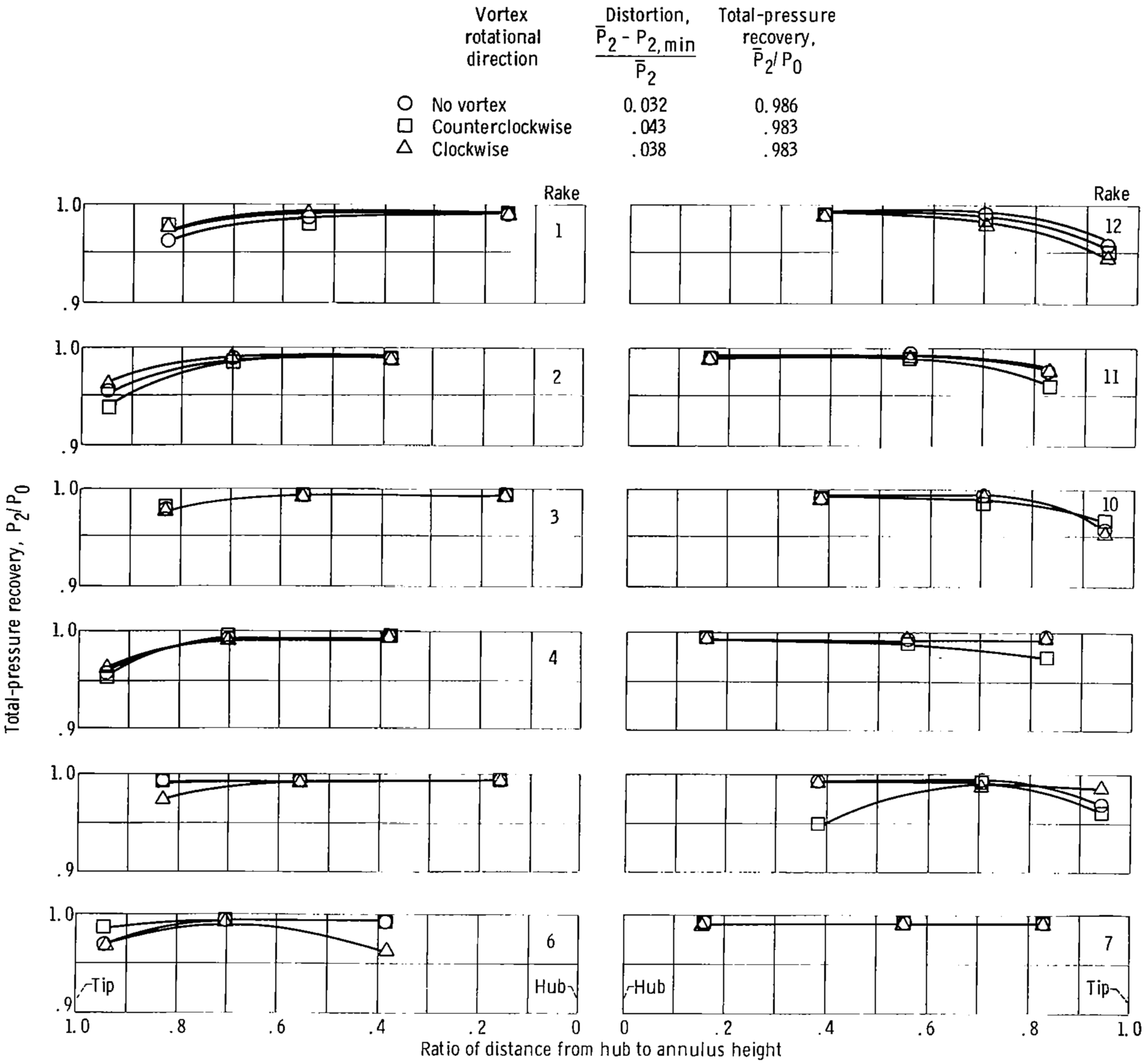

Vortex rotational direction	Distortion, $\frac{\bar{P}_2 - P_{2,min}}{\bar{P}_2}$	Total-pressure recovery, $\bar{P}_2/P_0$
○ No vortex	0.032	0.986
□ Counterclockwise	.043	.983
△ Clockwise	.038	.983

(b) Ingested vortex vertical position parameter $h/H = 0.225$.

Figure 21. - Continued.

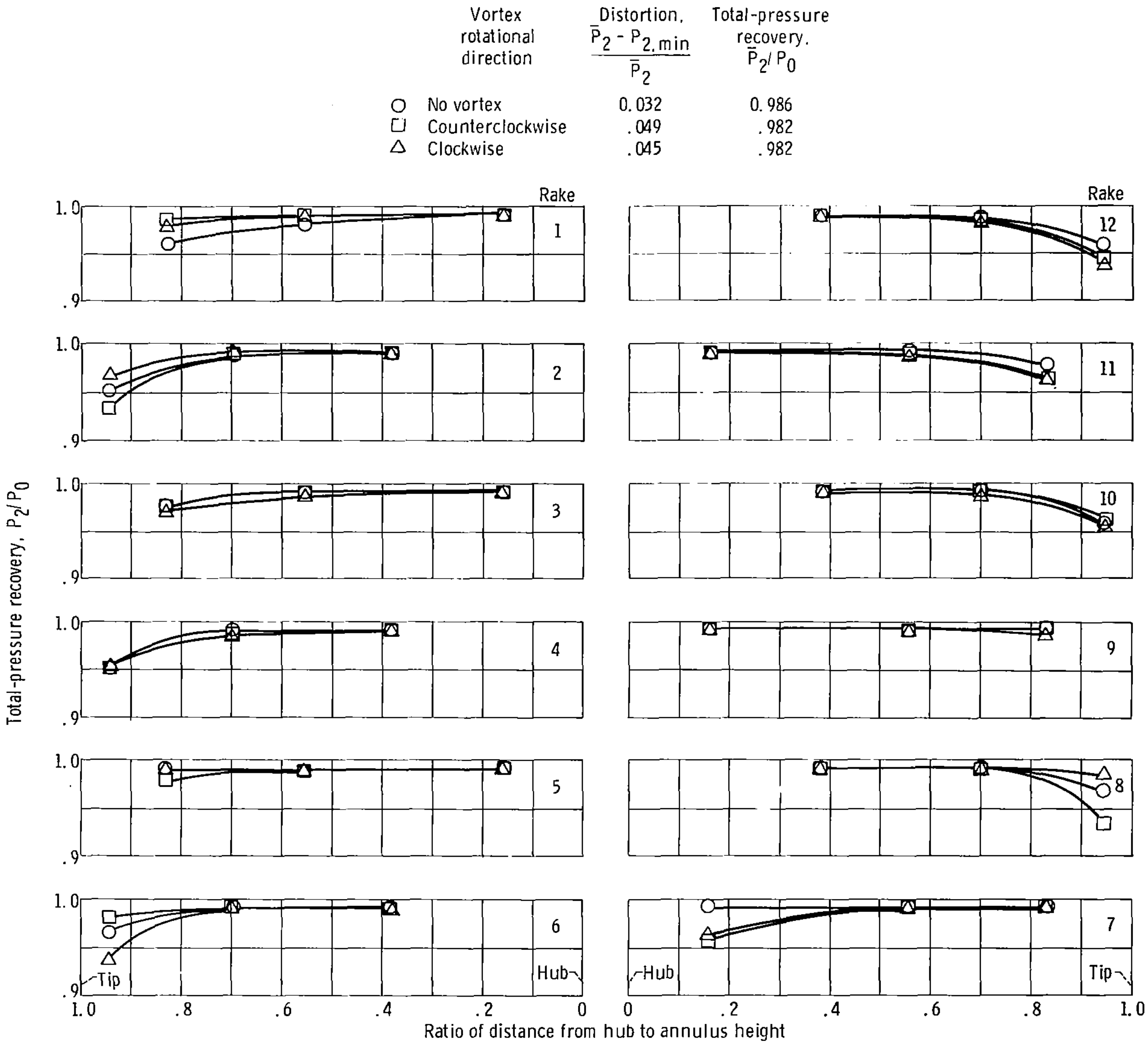

(c) Ingested vortex vertical position parameter h/H = 0.375.

Figure 21. - Continued.

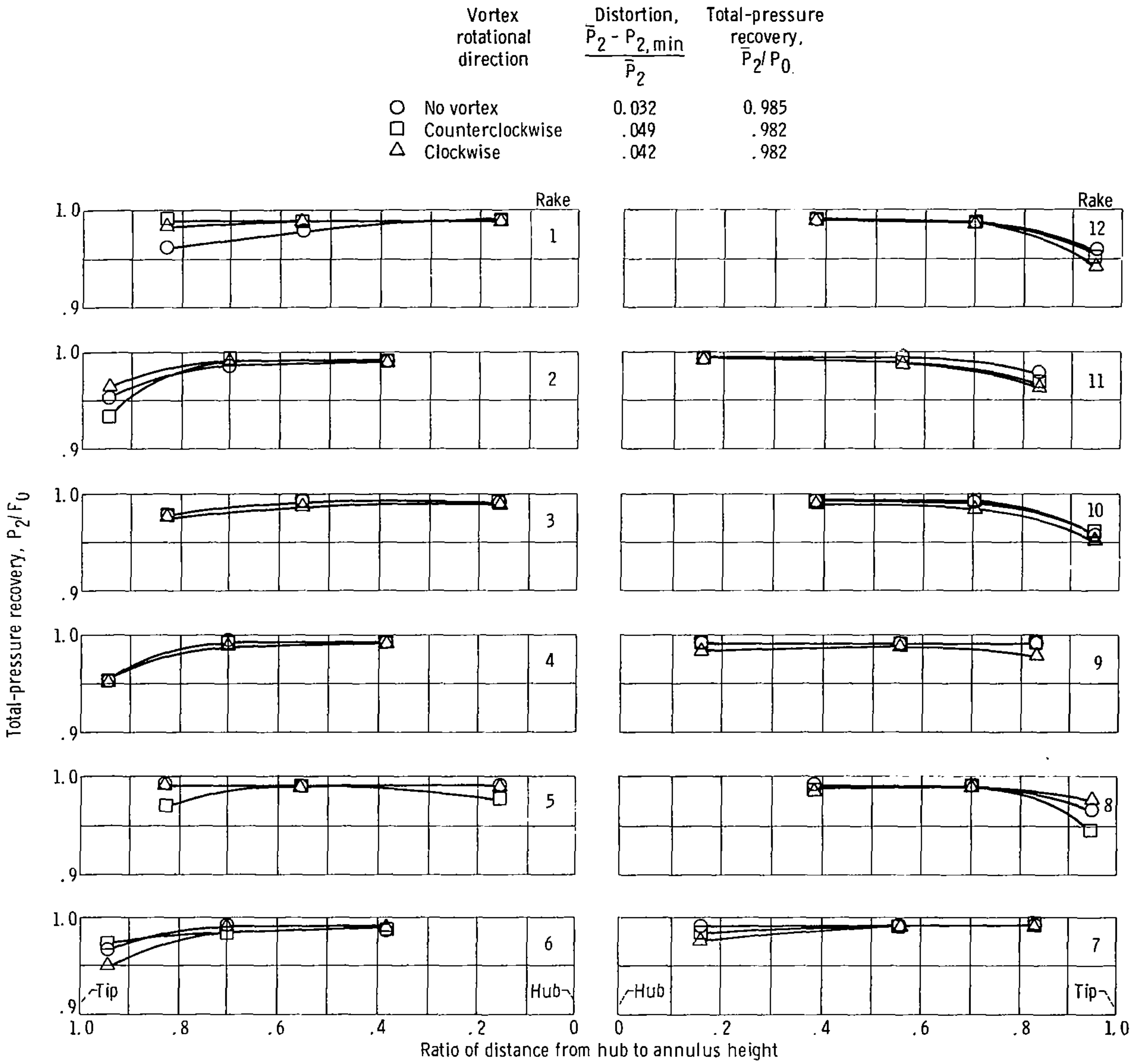

(d) Ingested vortex vertical position parameter h/H = 0.438.

Figure 21. - Continued.

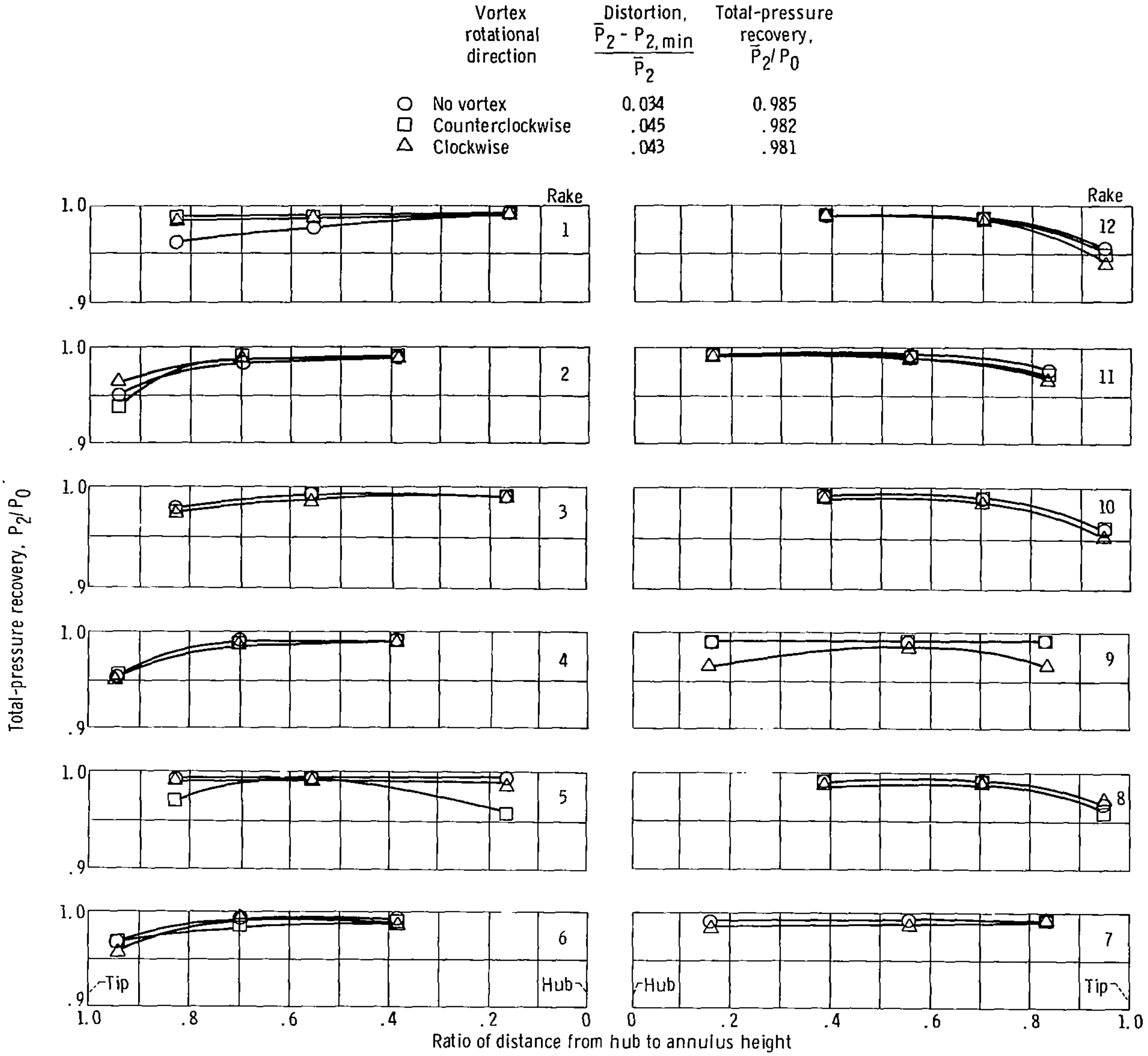

(e) Ingested vortex vertical position parameter h/H = 0.500.

Figure 21. - Continued.

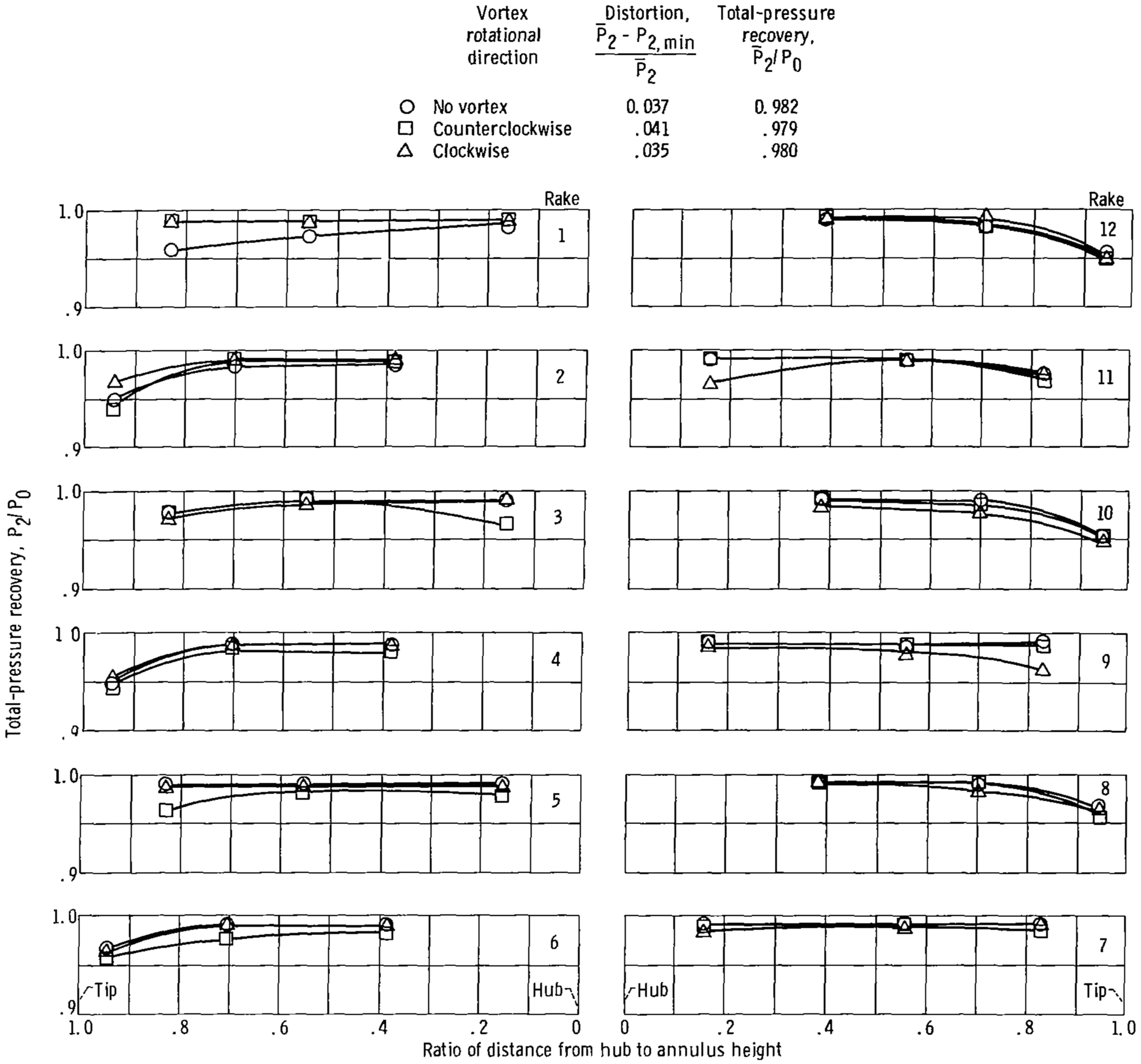

(f) Ingested vortex vertical position parameter h/H = 0.625.

Figure 21. - Continued.

	Vortex rotational direction	Distortion, $\frac{\bar{P}_2 - P_{2,min}}{\bar{P}_2}$	Total-pressure recovery, $\bar{P}_2/P_0$
○	No vortex	0.039	0.981
☐	Counterclockwise	.034	.977
△	Clockwise	.043	.980

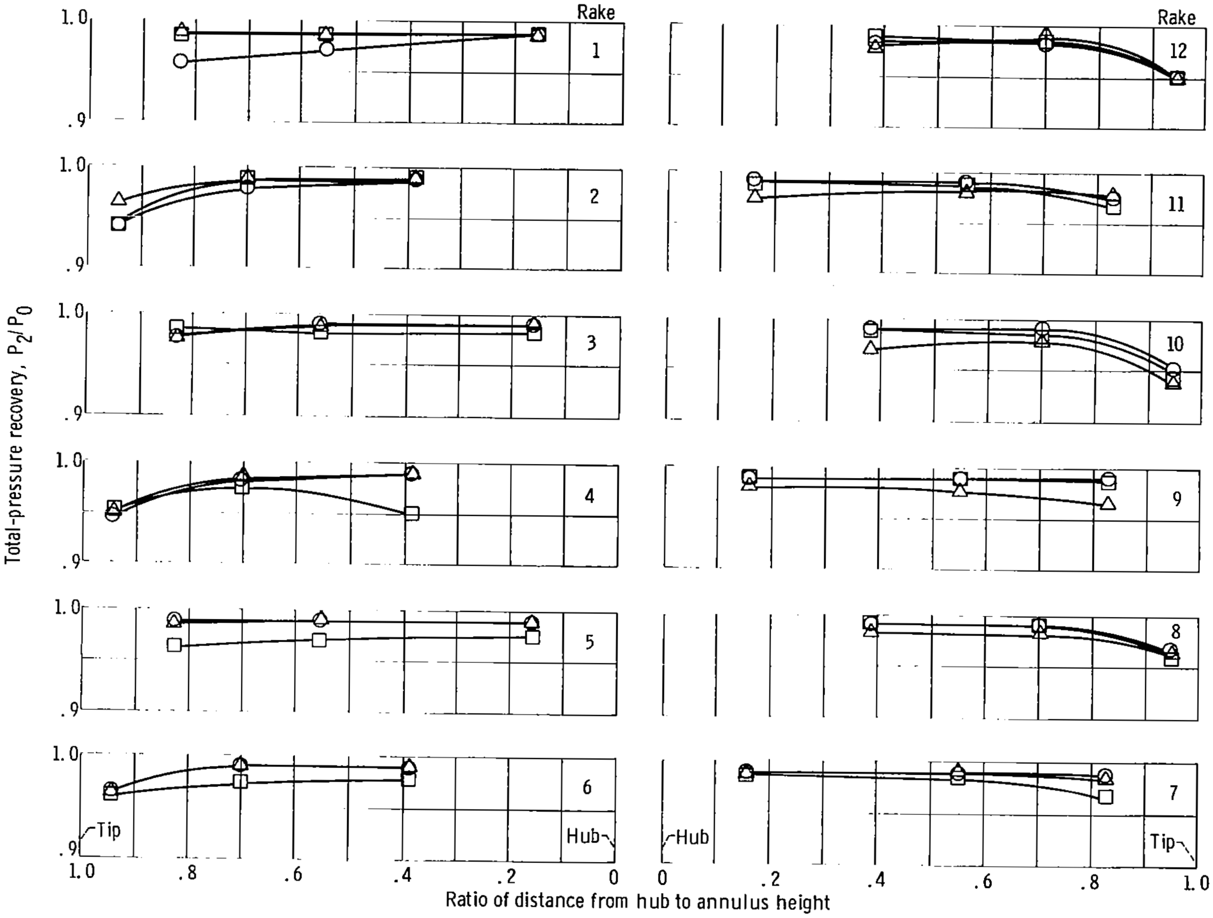

(g) Ingested vortex vertical position parameter h/H = 0.700.

Figure 21. - Continued.

Vortex rotational direction	Distortion, $\frac{\bar{P}_2 - P_{2,min}}{\bar{P}_2}$	Total-pressure recovery, $\bar{P}_2/P_0$
○ No vortex	0.038	0.981
□ Counterclockwise	.032	.976
△ Clockwise	.039	.979

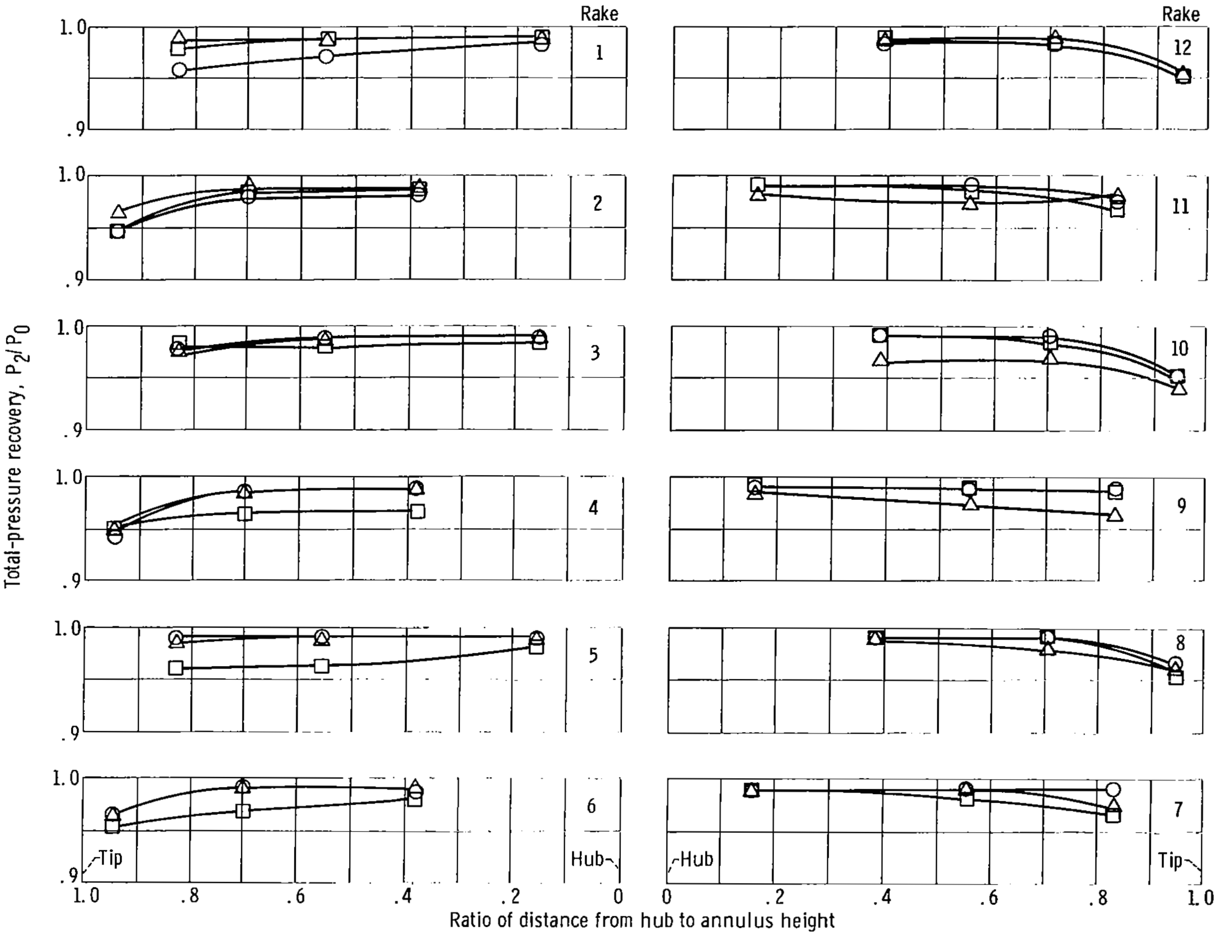

(h) Ingested vortex vertical position parameter h/H = 0.775.

Figure 21. - Concluded.

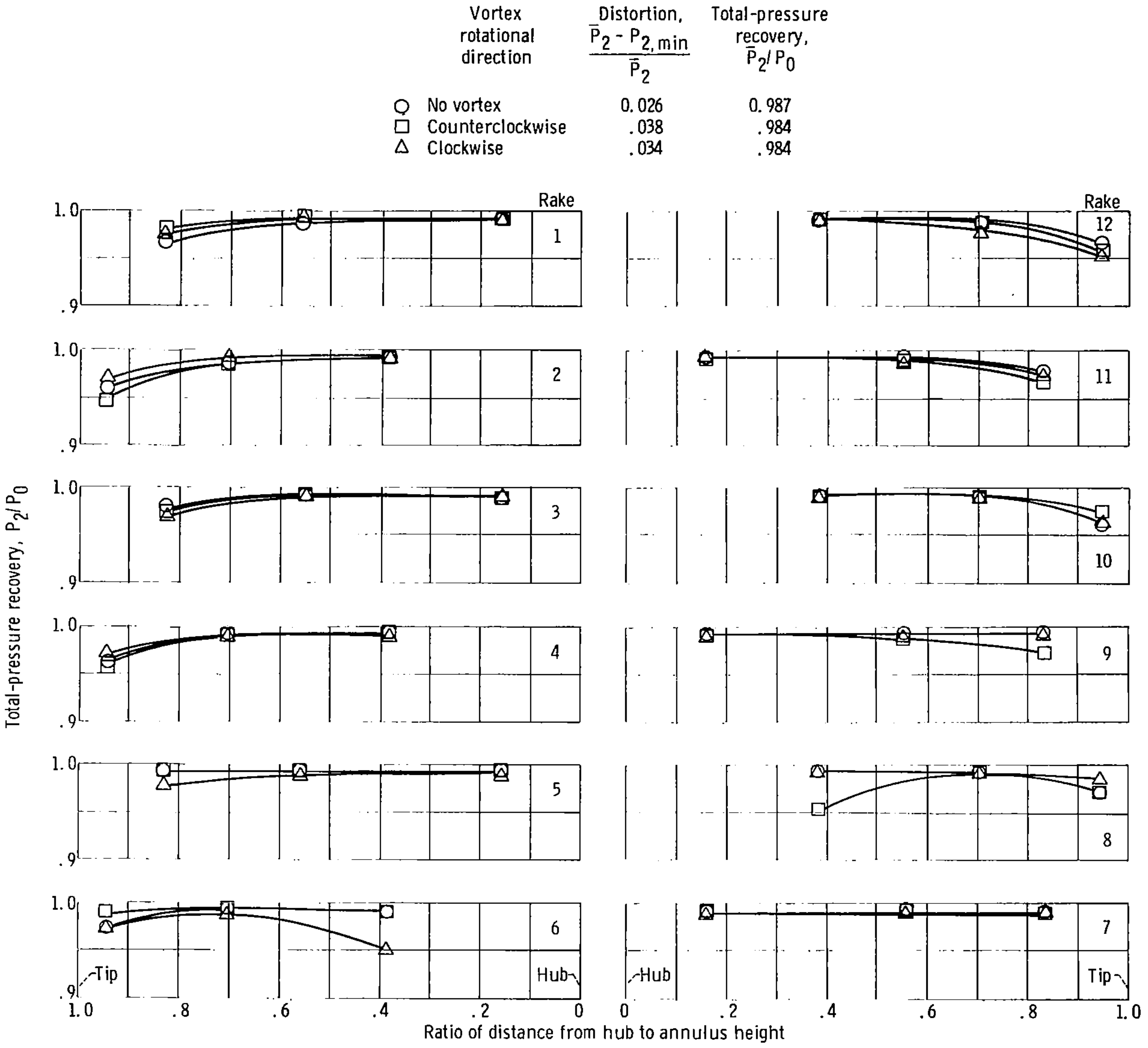

(a) Nominal engine corrected airflow, 16.5 kilograms per second; nominal inlet mass-flow ratio, 0.70.

Figure 22. - Compressor face total-pressure profiles. Ingested vortex vertical position parameter h/H ≈ 0.225.

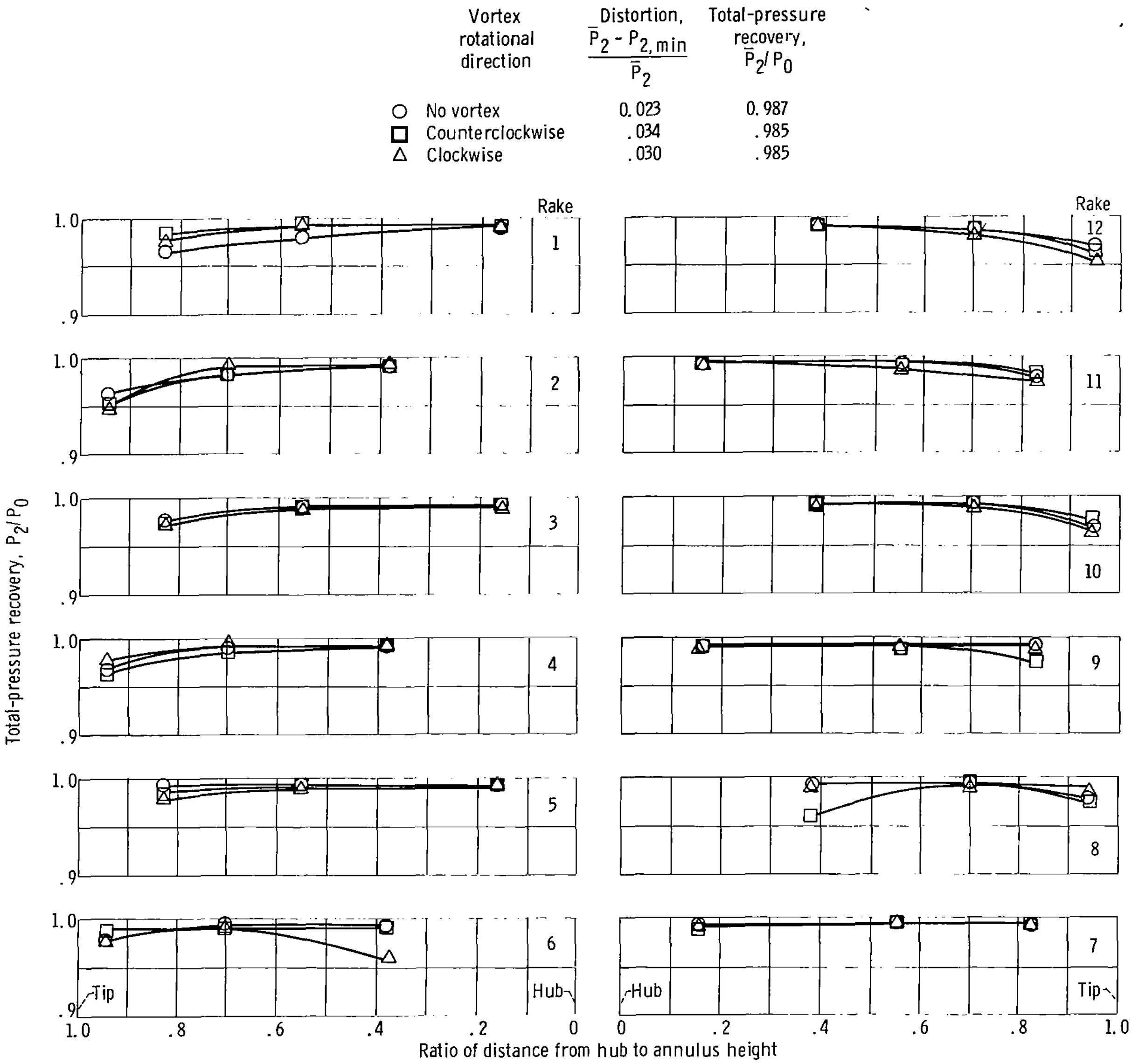

(b) Nominal engine corrected airflow, 14.5 kilograms per second; nominal inlet mass-flow ratio, 0.61.

Figure 22. - Concluded.

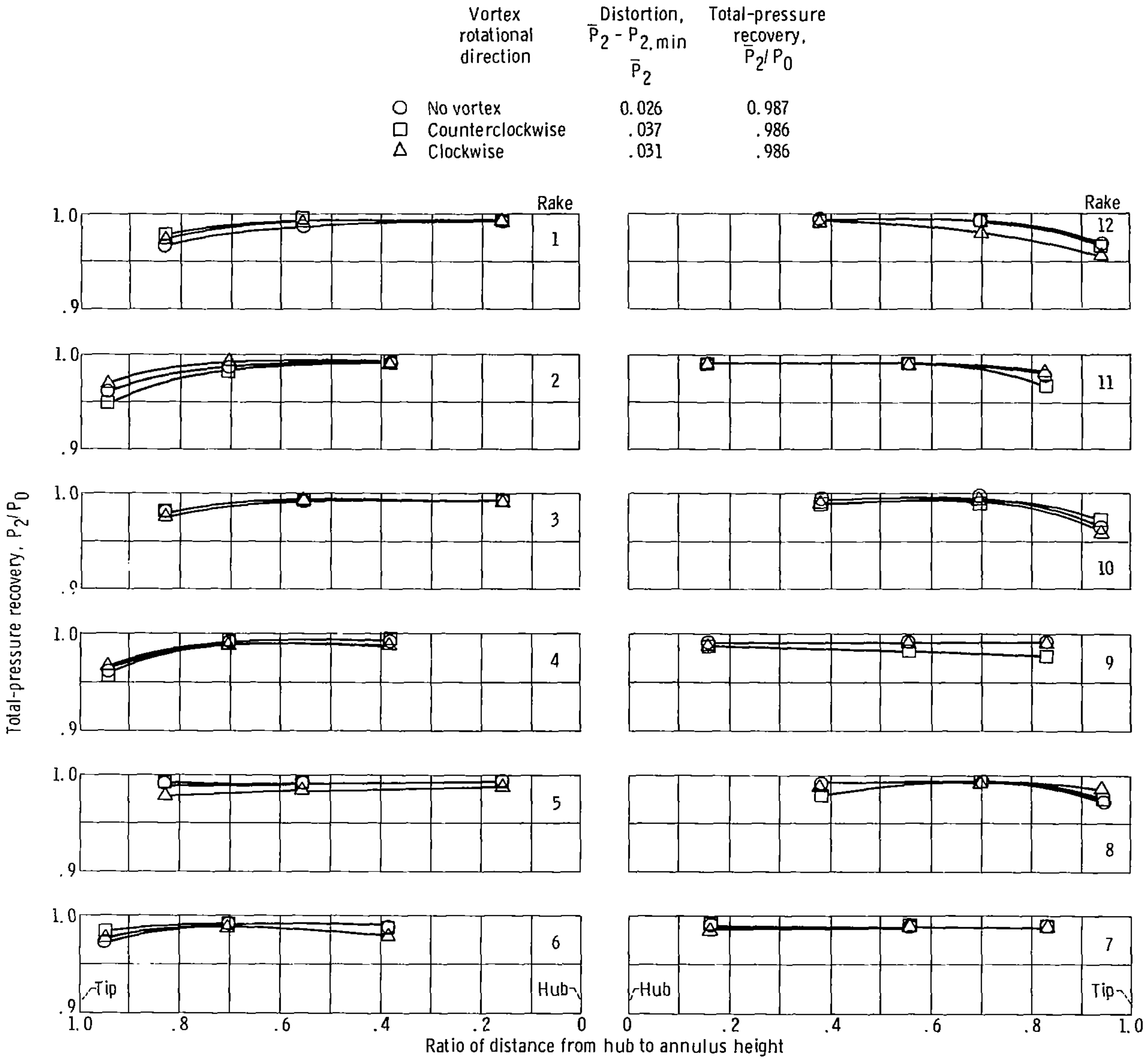

(a) Nominal engine corrected airflow, 16.5 kilograms per second; nominal inlet mass-flow ratio, 0.70.

Figure 23. - Compressor face total-pressure profiles. Ingested vortex vertical position parameter h/H = 0.150.

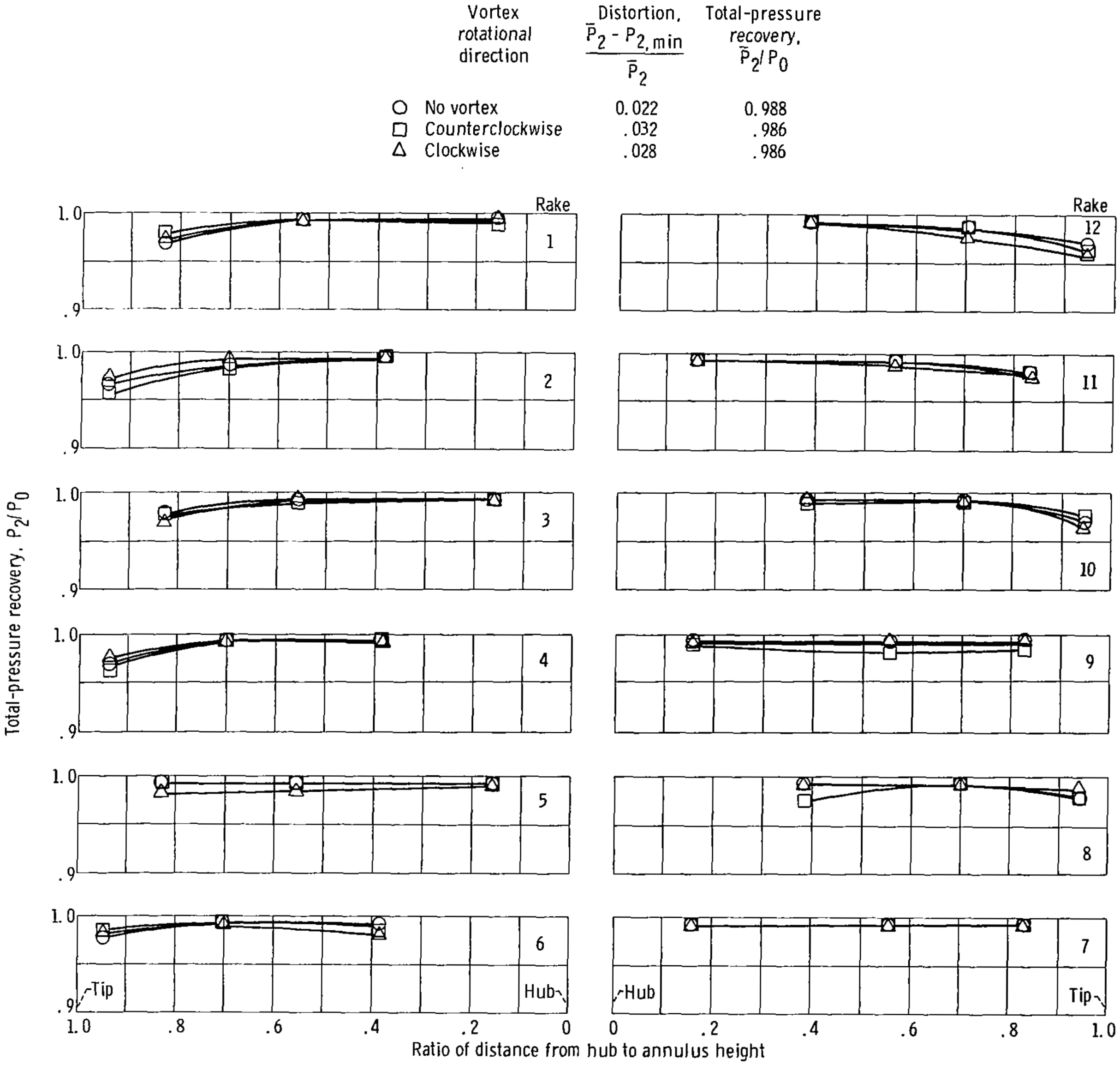

(b) Nominal engine corrected airflow, 14.5 kilograms per second; nominal inlet mass-flow ratio, 0.61.

Figure 23. - Concluded.

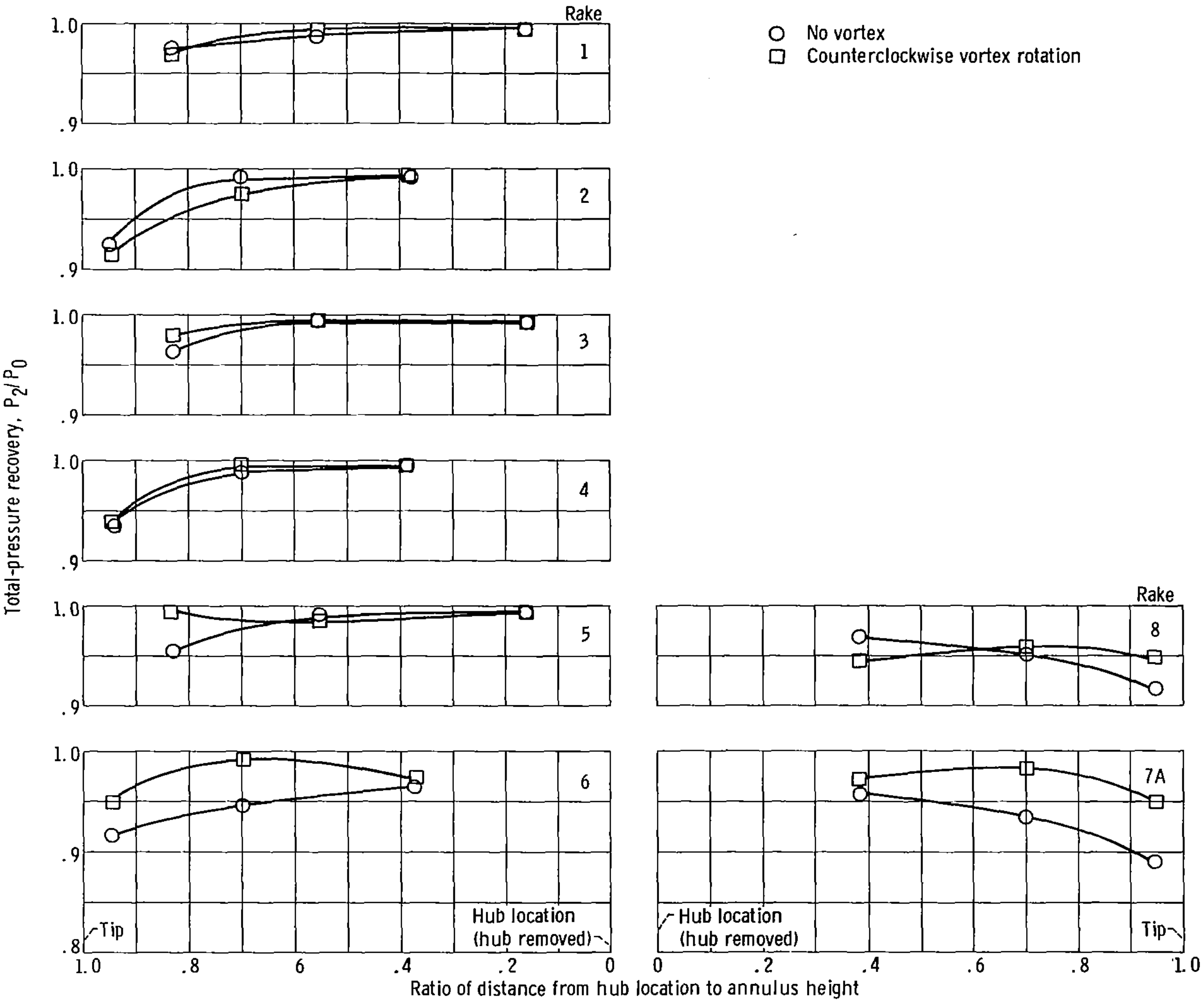

(a) Ingested vortex vertical position parameter $h/H \approx 0.14$.

Figure 24. - Compressor face total-pressure profiles. Inlet mated to coldpipe; estimated corrected airflow, 21.5 kilograms per second; estimated inlet mass-flow ratio, 0.9.

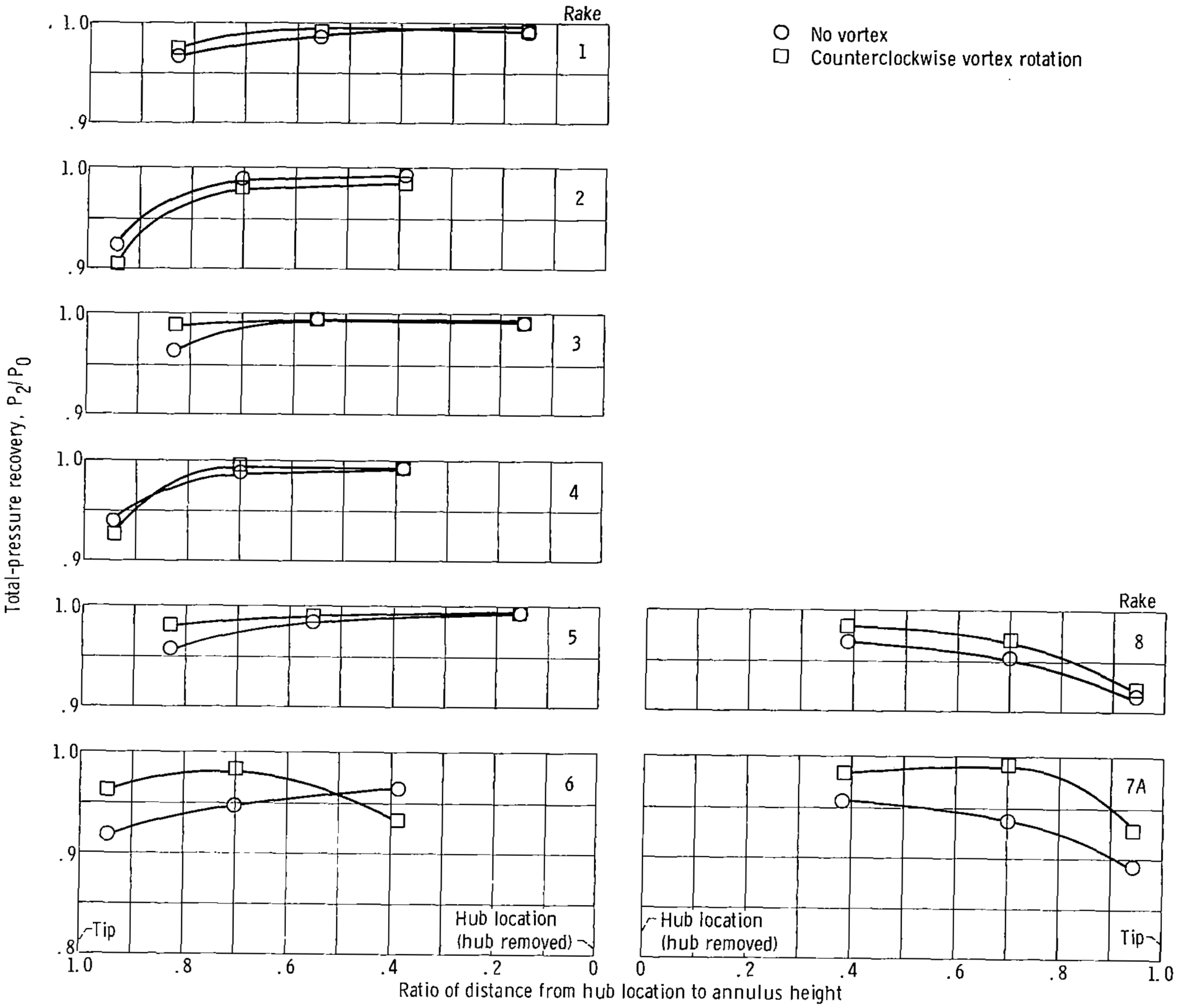

(b) Ingested vortex vertical position parameter $h/H \approx 0.32$.

Figure 24. - Continued.

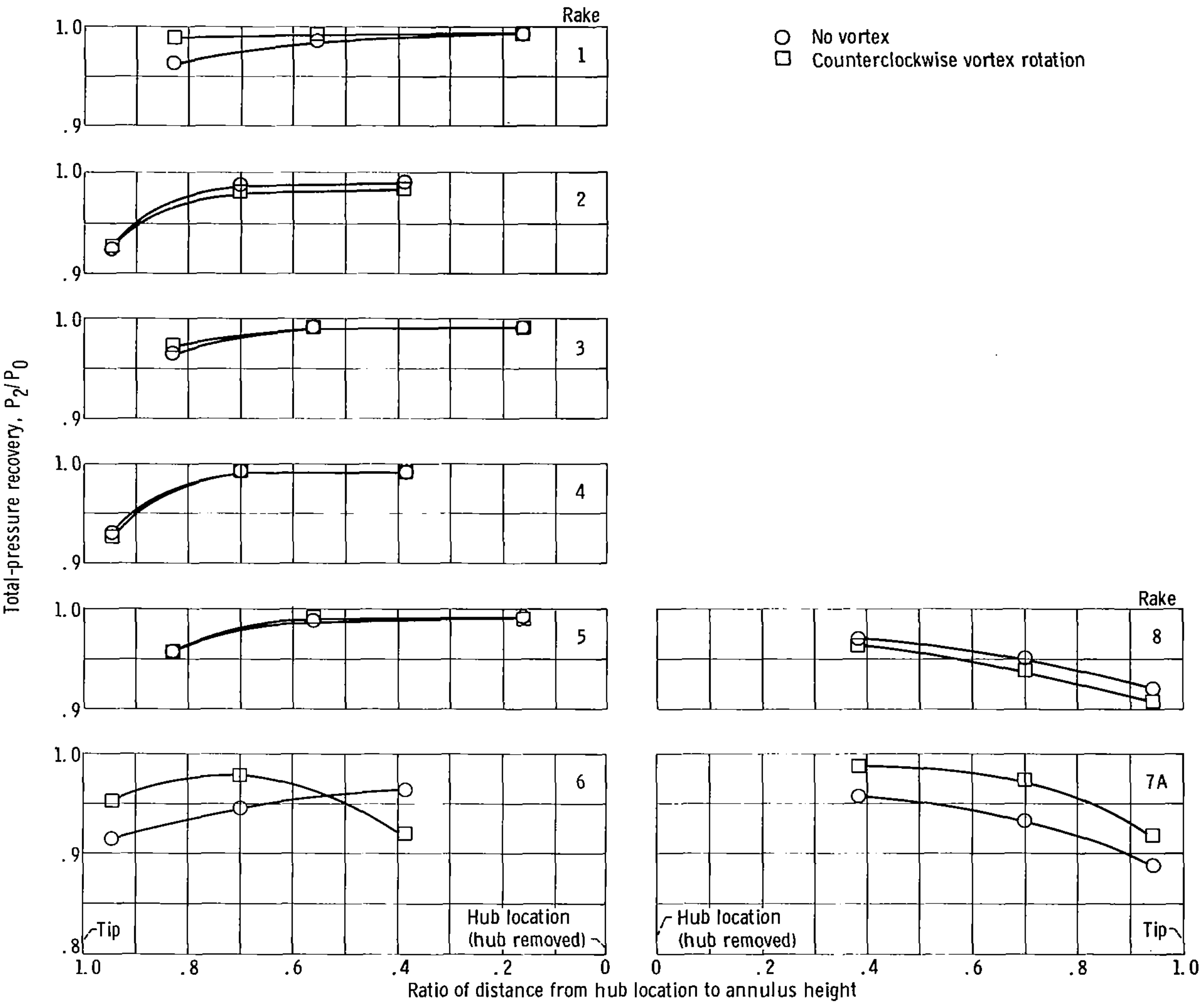

(c) Ingested vortex vertical position parameter $h/H \approx 0.5$.

Figure 24. - Concluded.

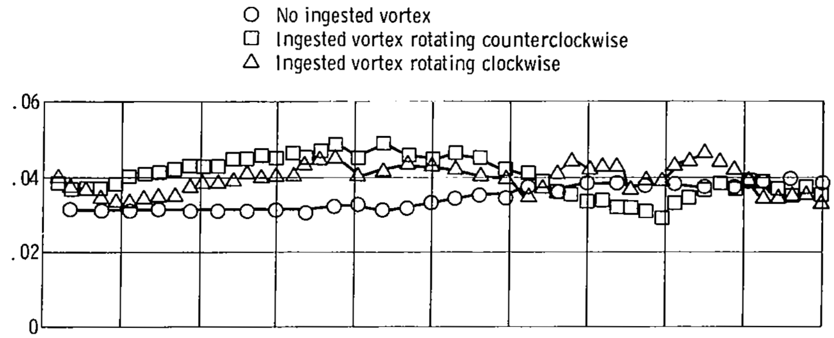

(a) Nominal engine corrected airflow, 18 kilograms per second; nominal inlet mass-flow ratio, 0.76.

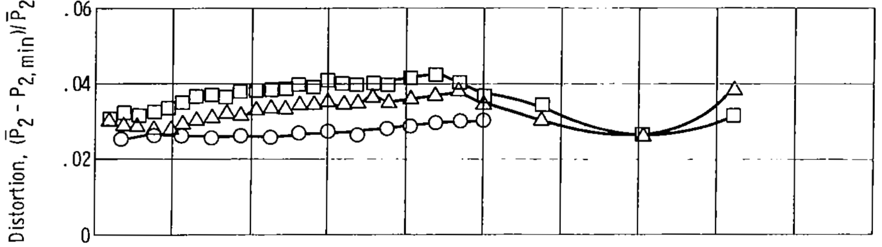

(b) Nominal engine corrected airflow, 16.5 kilograms per second; nominal inlet mass-flow ratio, 0.70.

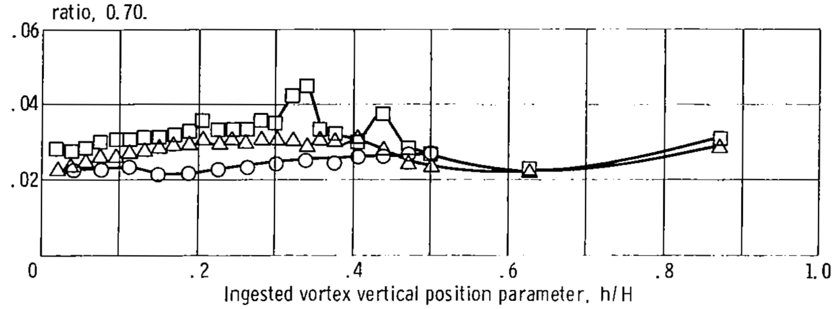

(c) Nominal engine corrected airflow, 14.5 kilograms per second; nominal inlet mass-flow ratio, 0.61.

Figure 25. - Effect of ingested vortex on compressor face total-pressure distortion.

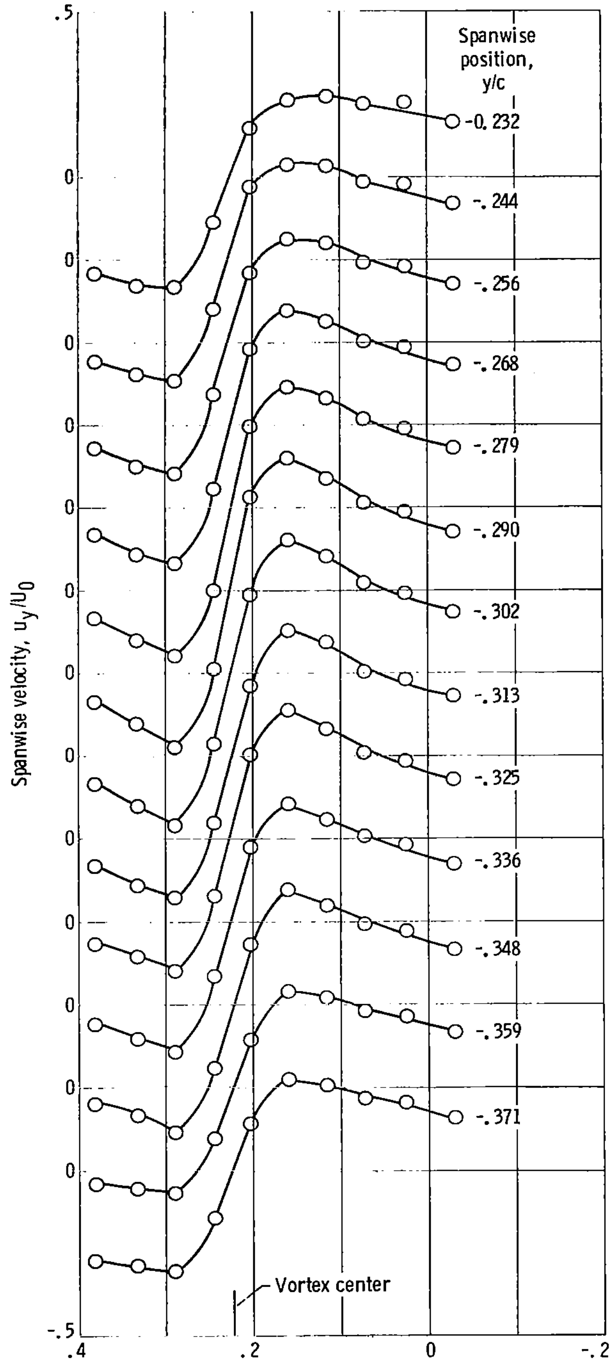

(a) Spanwise velocity profiles.

Figure 26. - Vortex properties prior to entering inlet, x/c = 7.03; wing angle of attack, 11° (counterclockwise vortex).

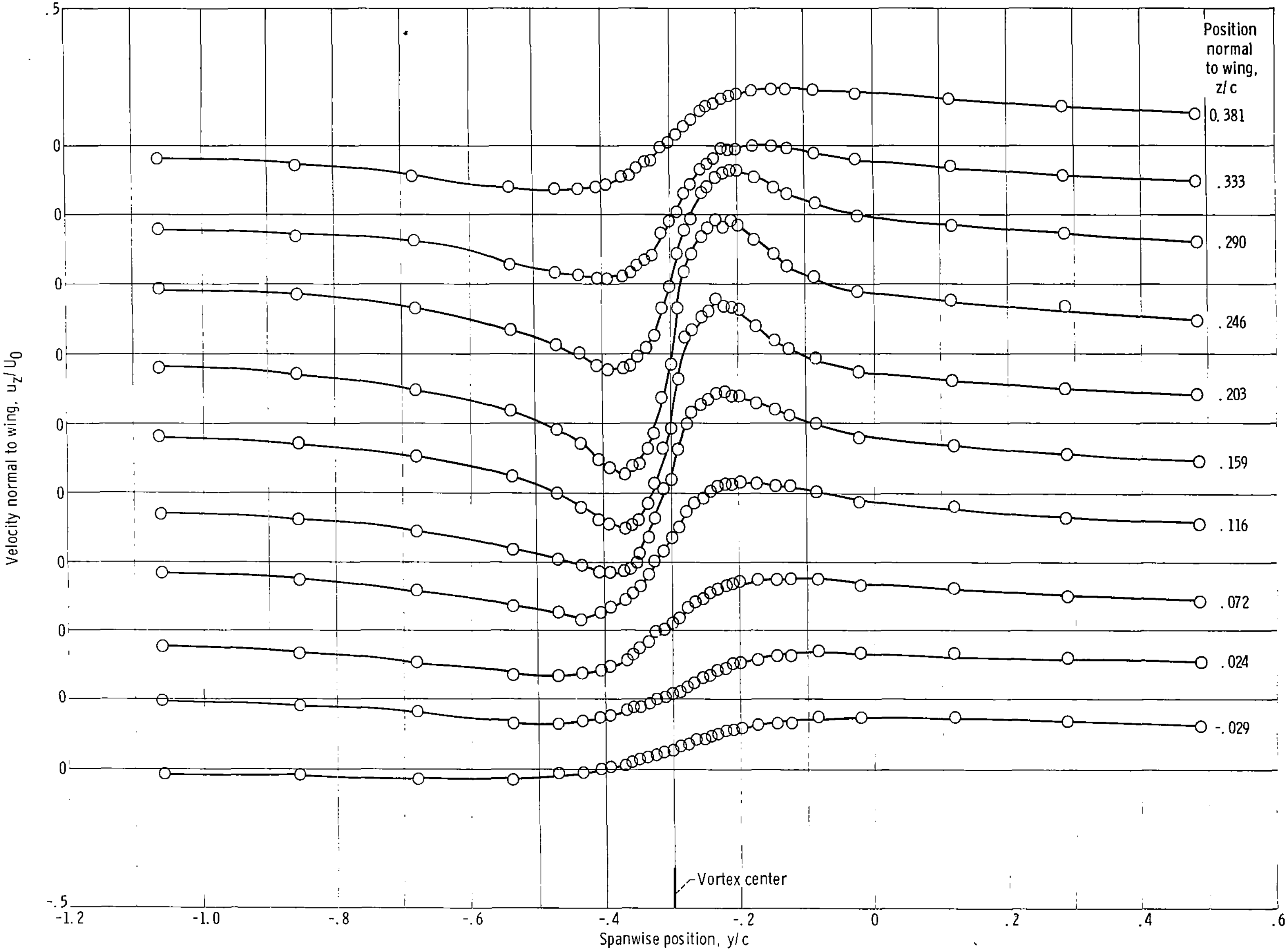

(b) Normal velocity profiles.

Figure 26. - Continued.

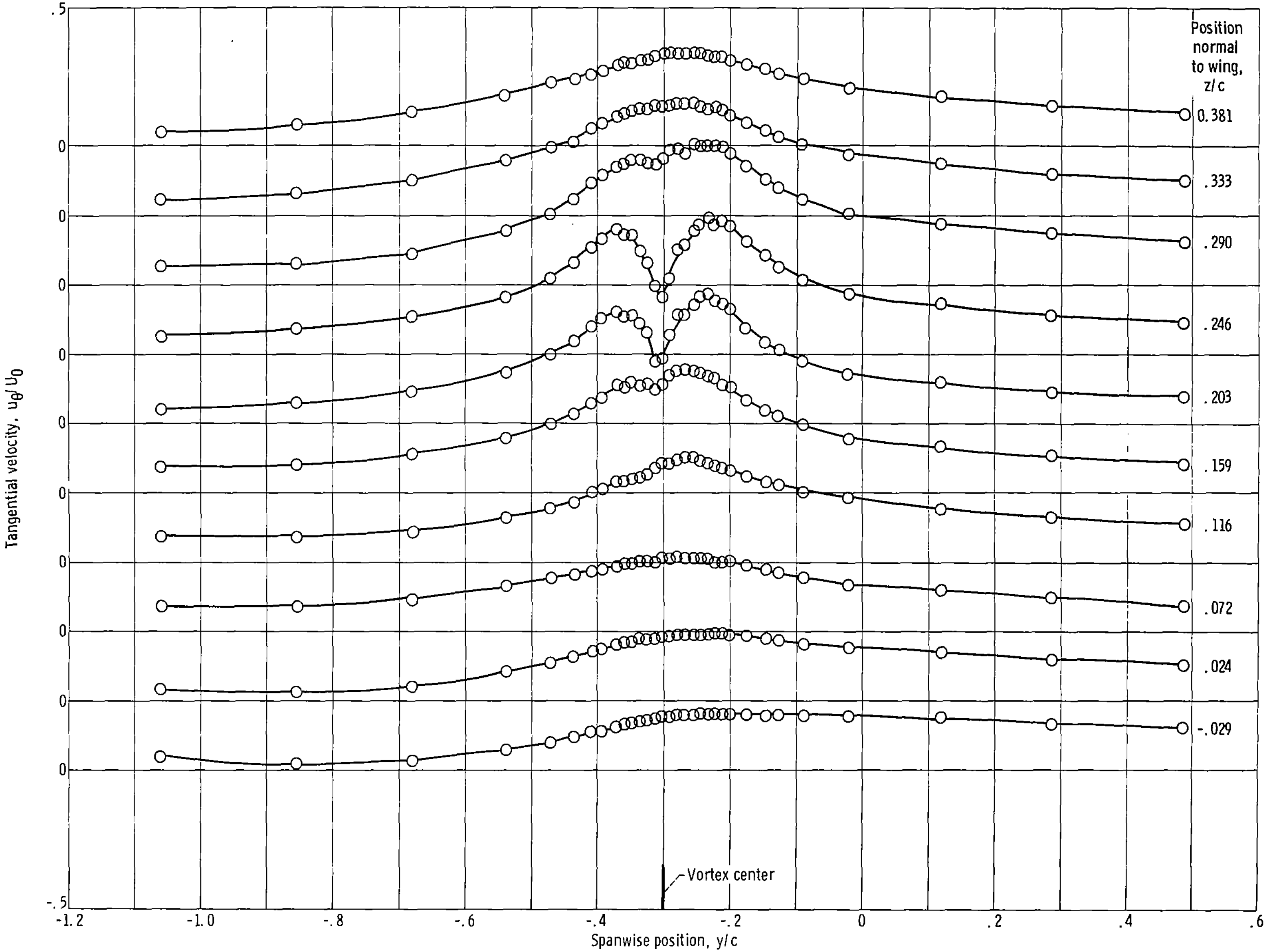

(c) Tangential velocity profiles.

Figure 26. - Continued.

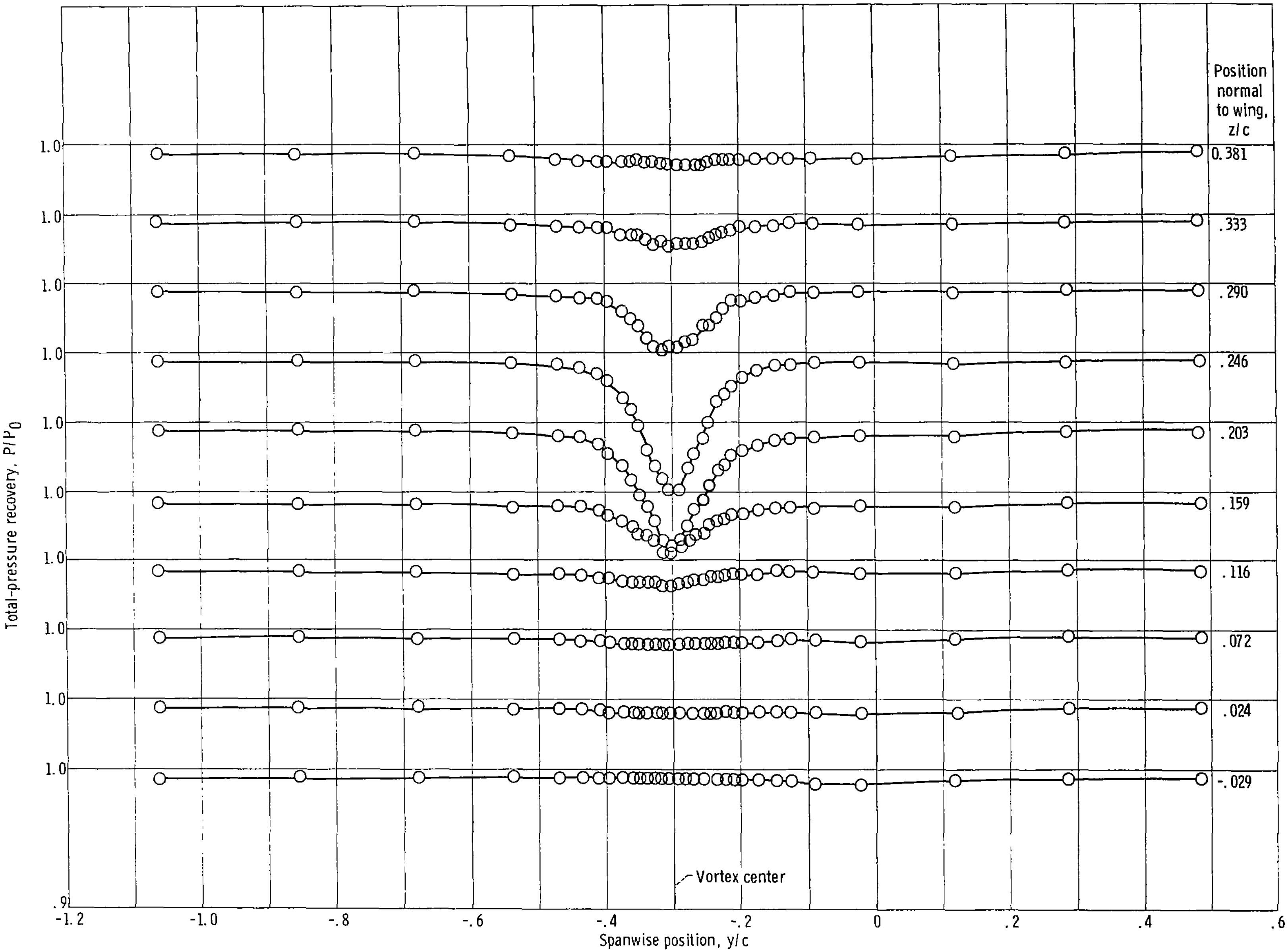

(d) Total-pressure recovery profiles.

Figure 26. - Continued.

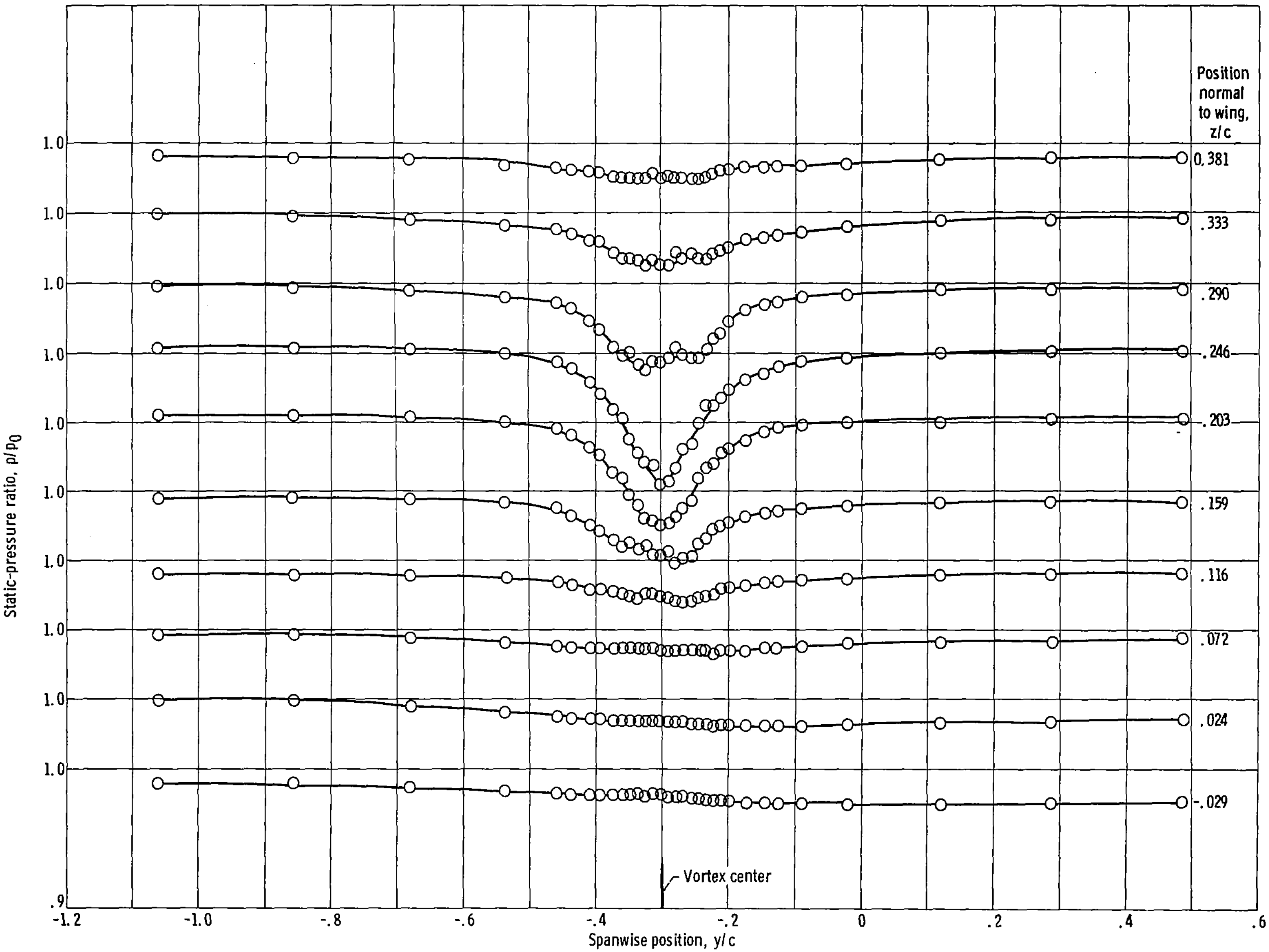

(e) Static-pressure ratio profiles.

Figure 26. - Continued.

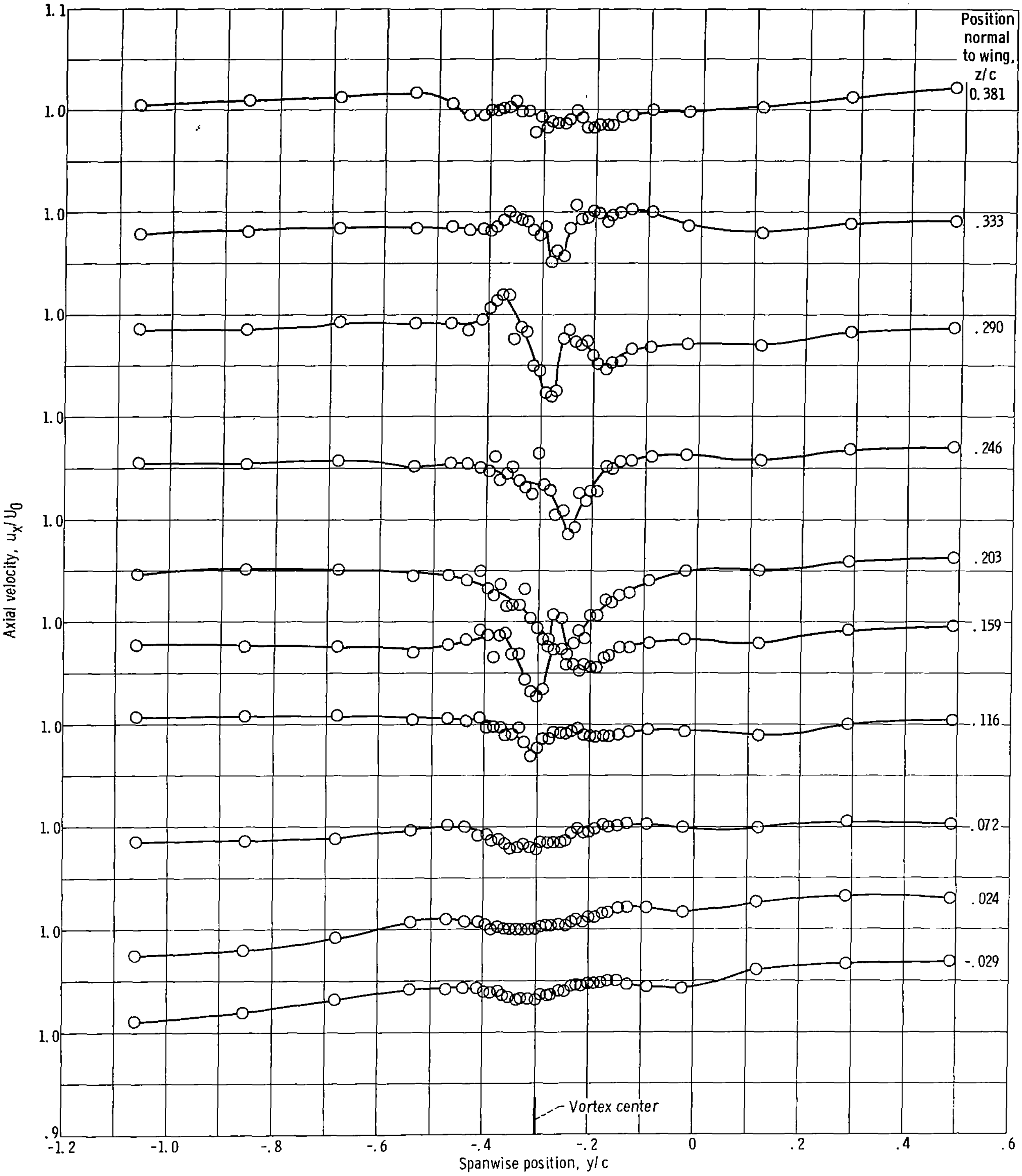

(f) Axial velocity profiles.

Figure 26. - Concluded.

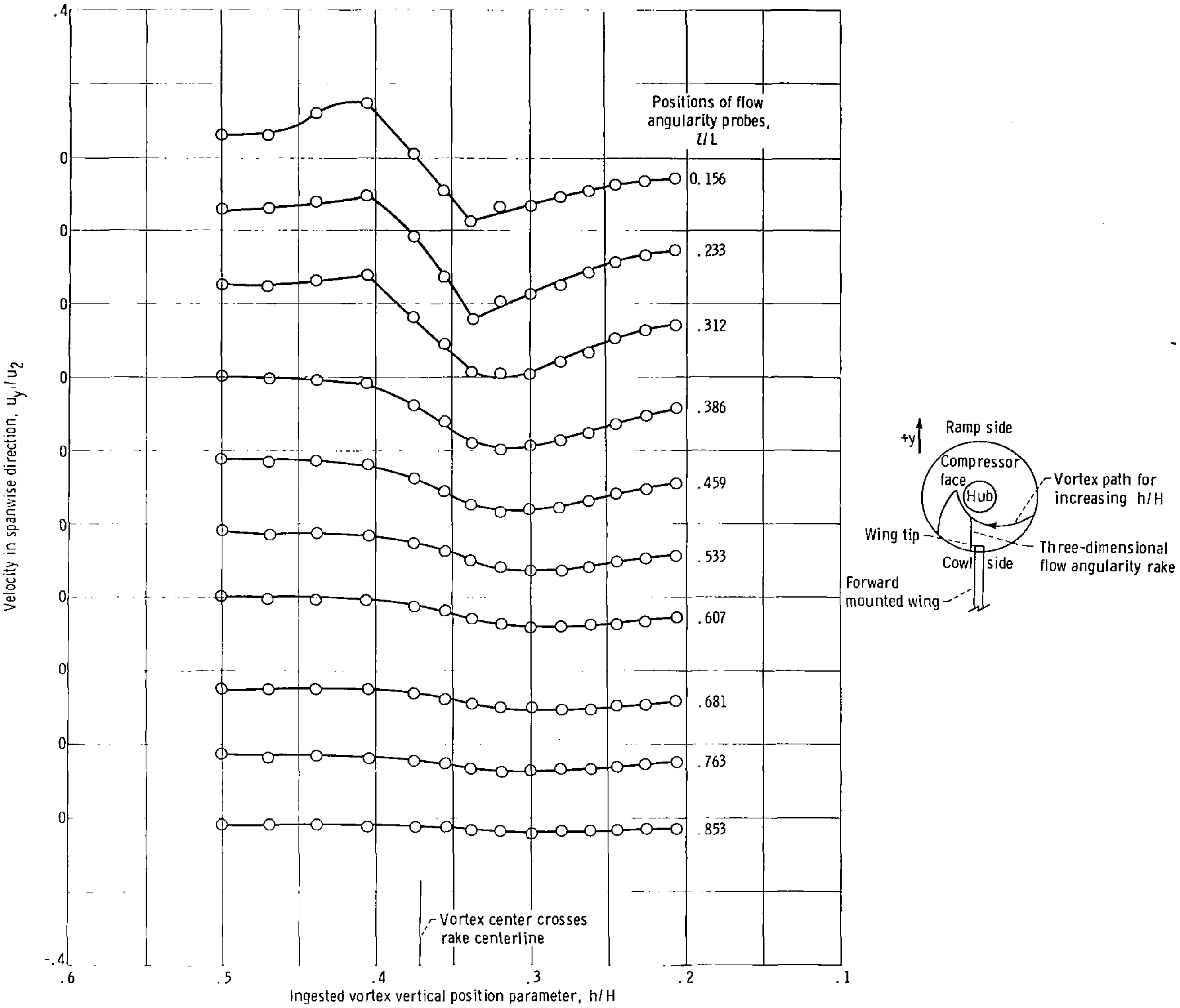

(a) Spanwise velocity profiles.

Figure 27. - Vortex properties at compressor face. Nominal engine corrected airflow, 14.5 kilograms per second; nominal inlet mass-flow ratio, 0.61; wing angle of attack, 11° (counterclockwise vortex).

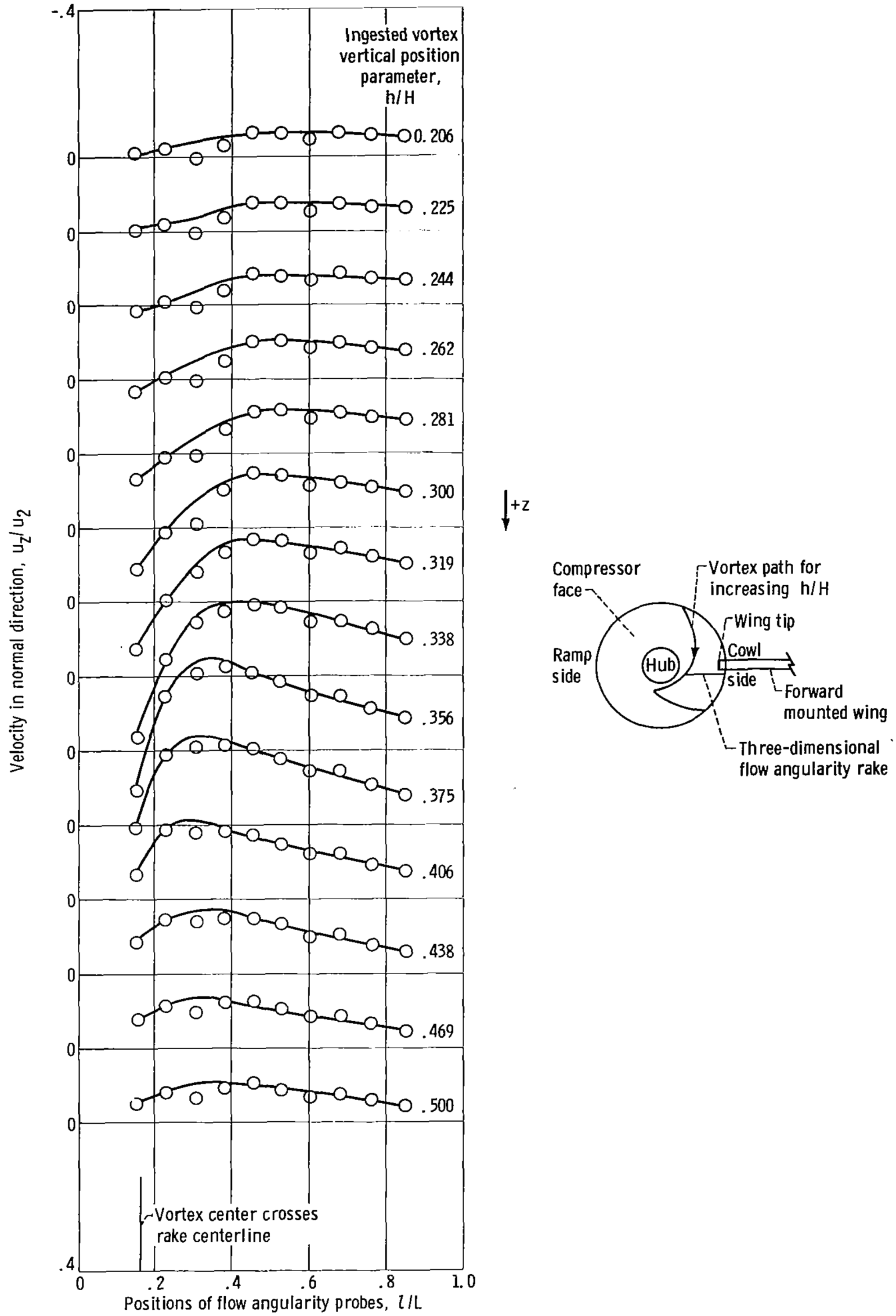

(b) Normal velocity profiles.

Figure 27. - Continued.

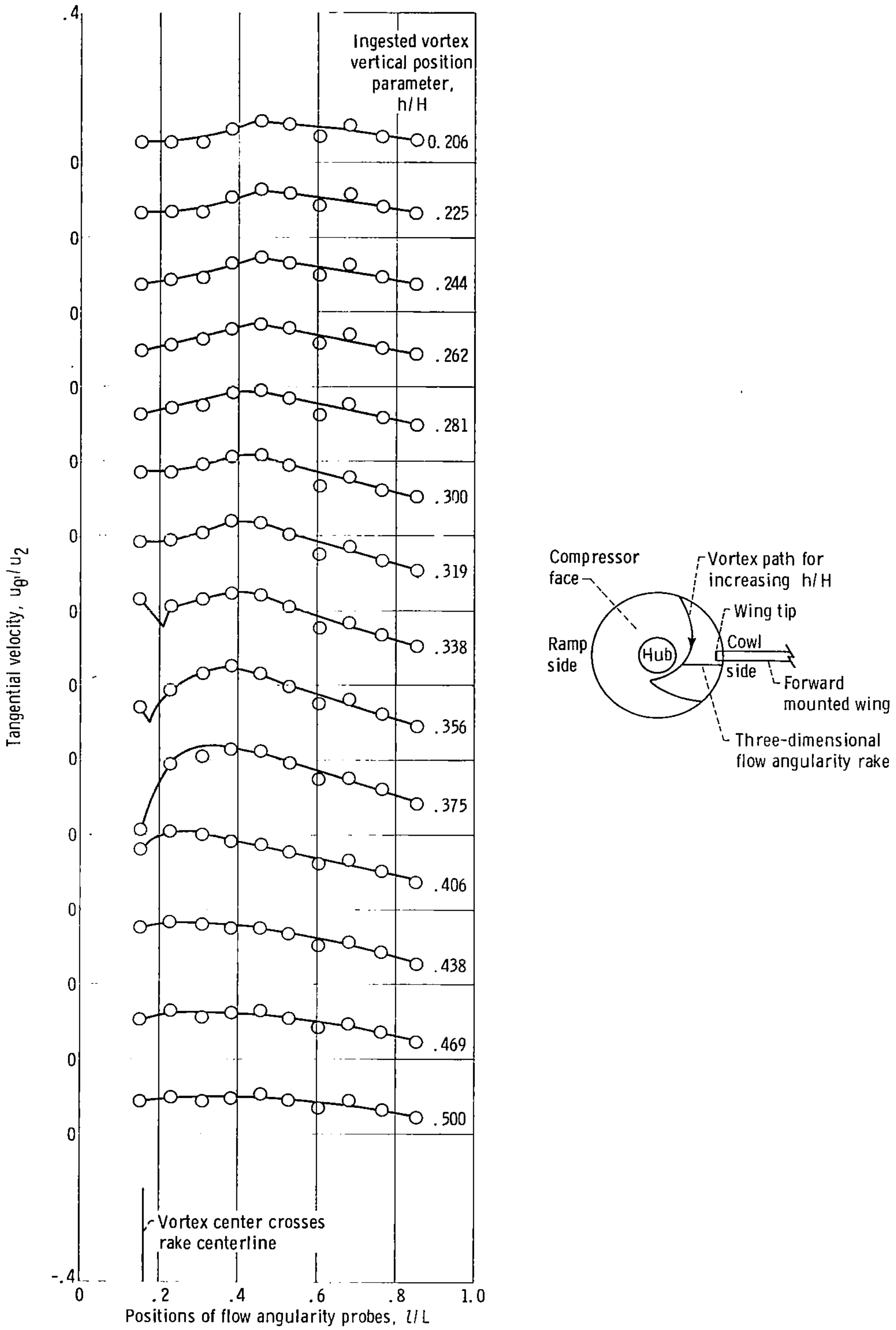

(c) Tangential velocity profiles.

Figure 27. - Continued.

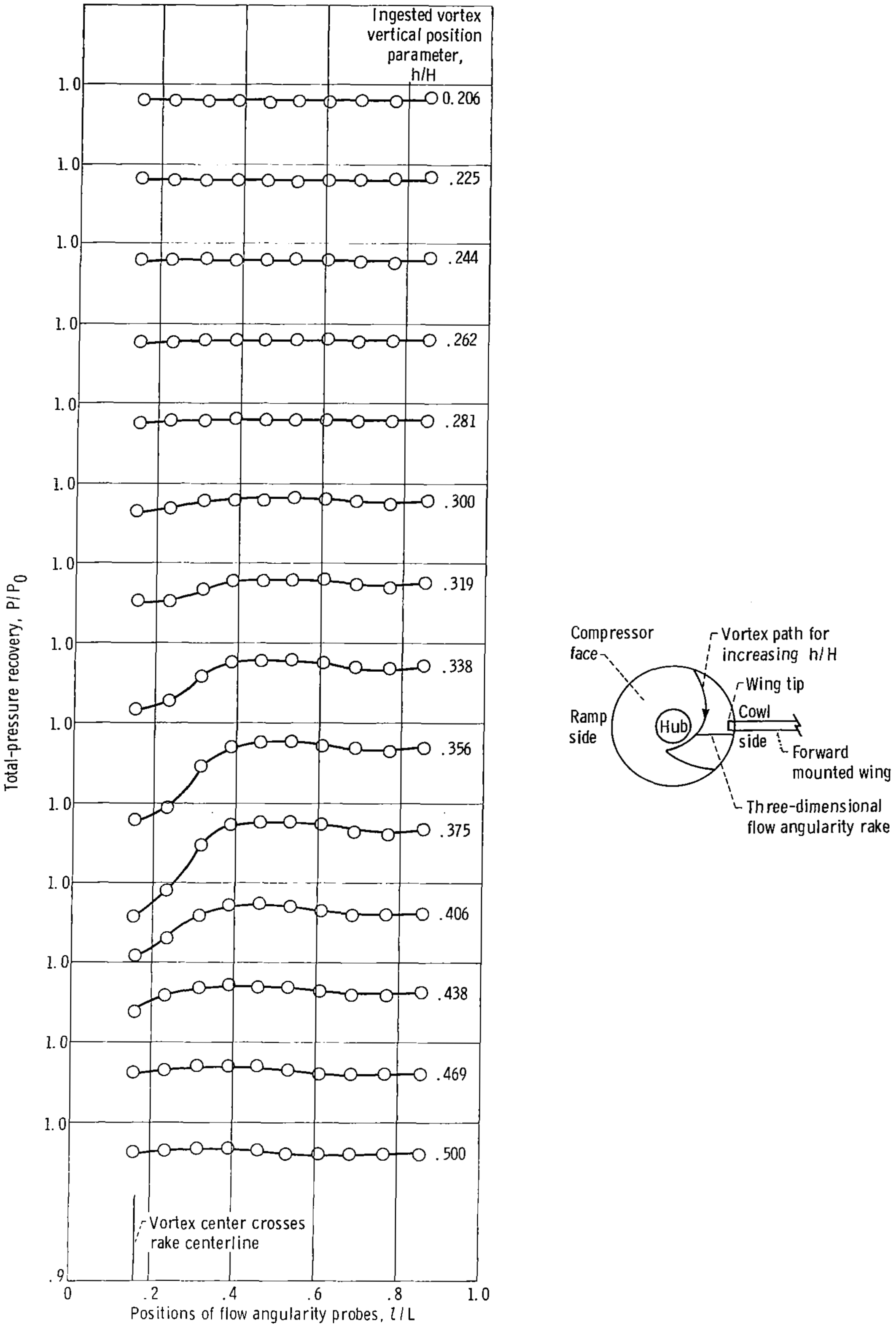

(d) Total-pressure recovery profiles.

Figure 27. - Continued.

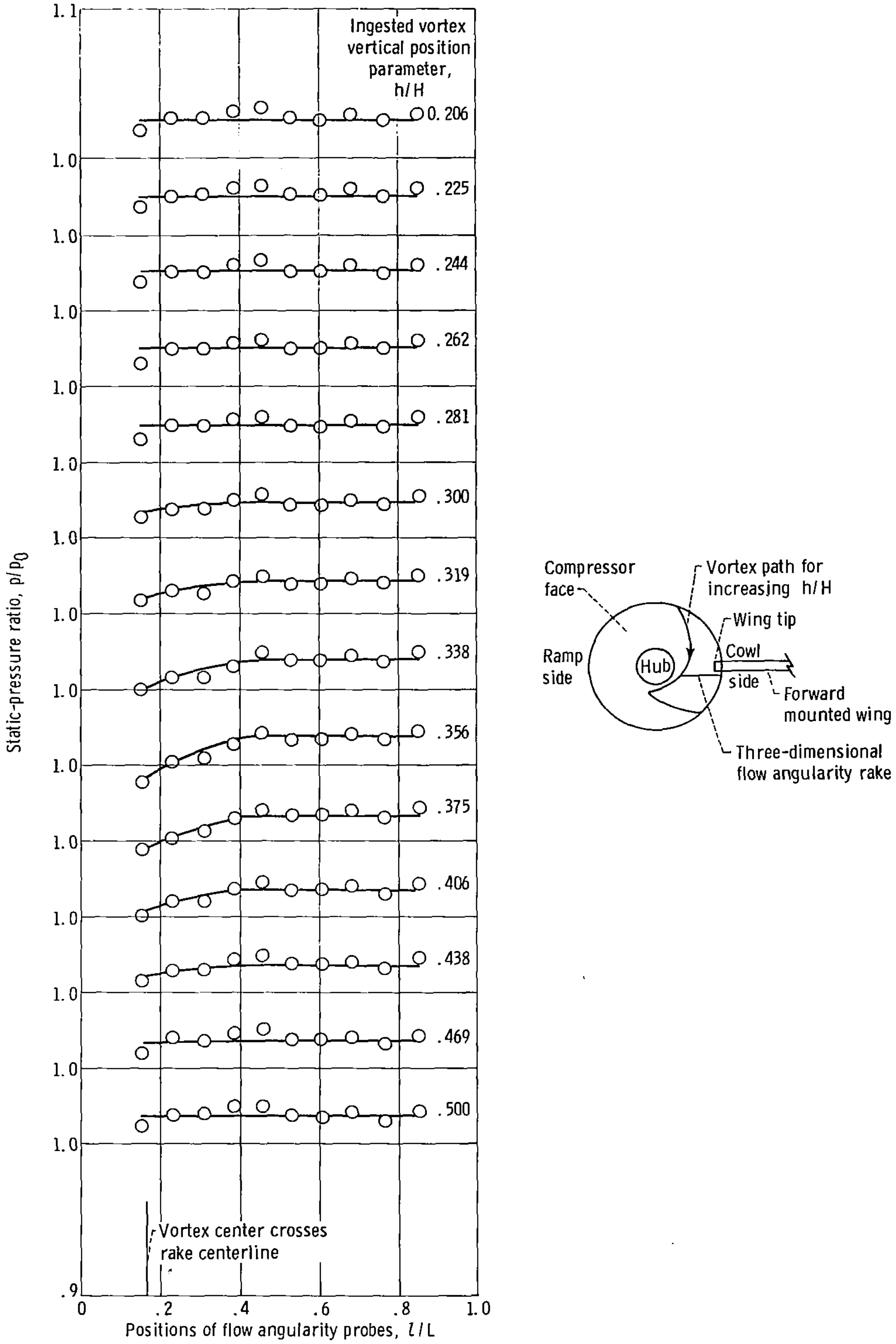

(e) Static-pressure ratio profiles.

Figure 27. - Continued.

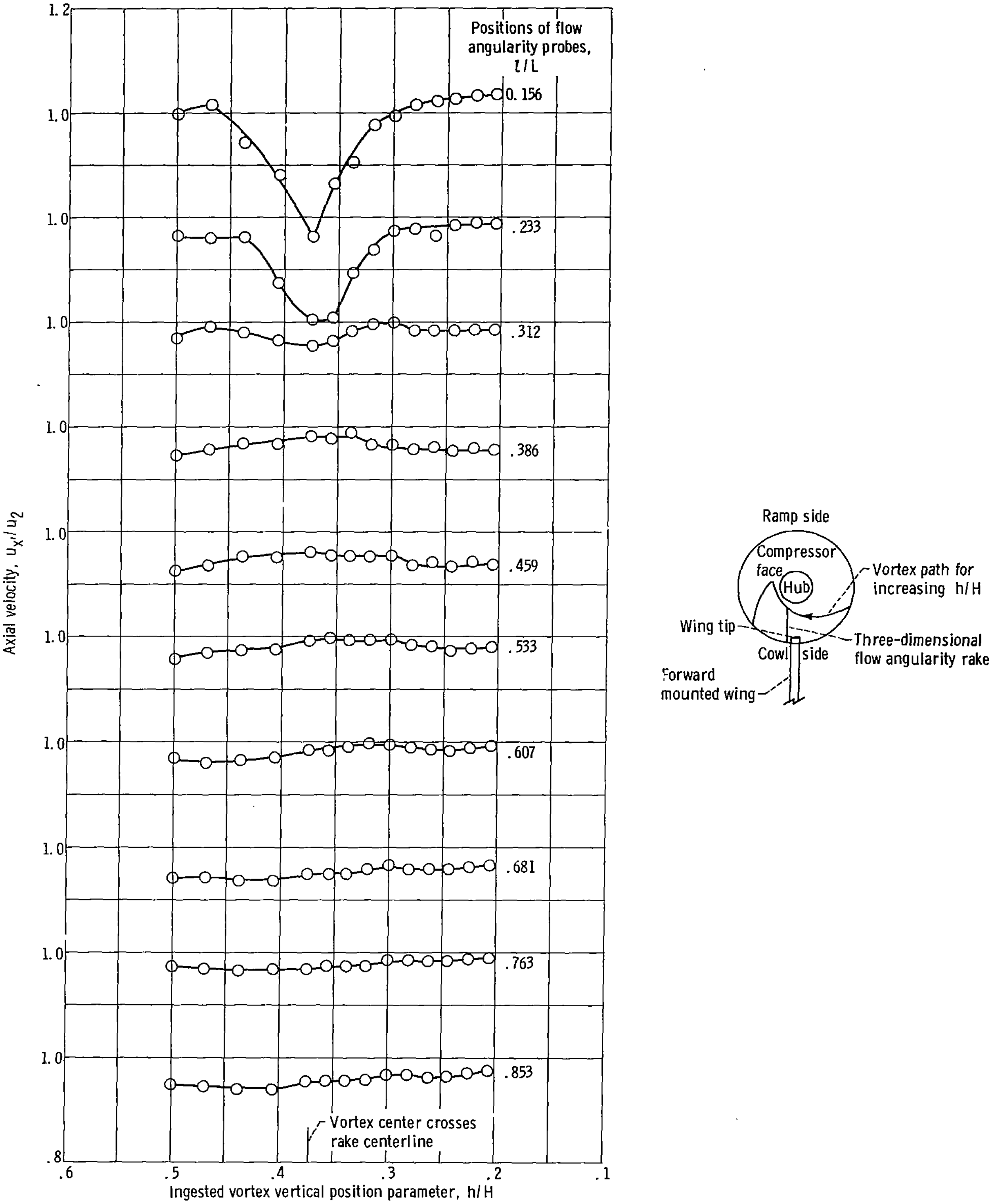

(f) Axial velocity profiles.

Figure 27. - Concluded.

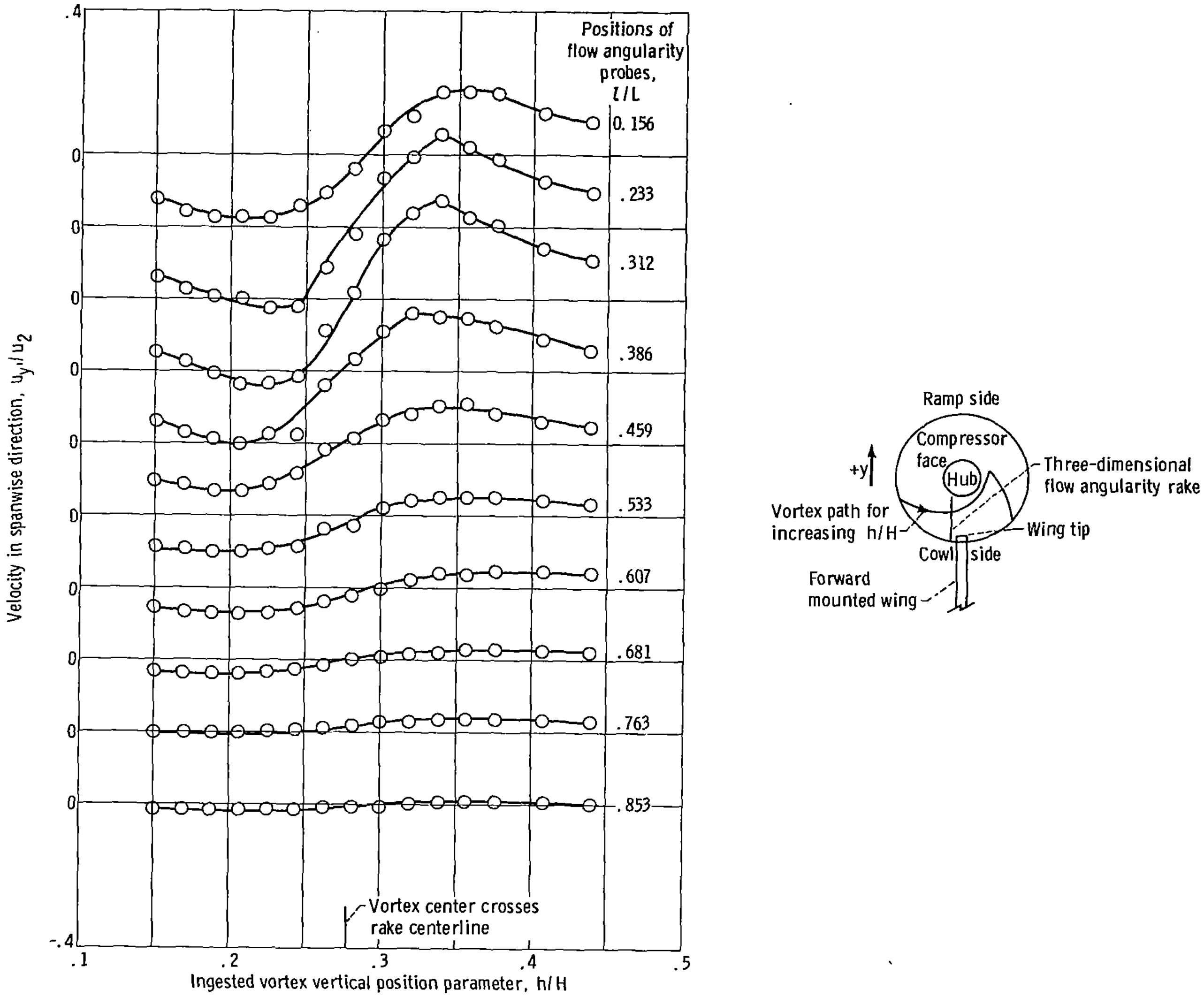

(a) Spanwise velocity profiles.

Figure 28. - Vortex properties at compressor face. Nominal engine corrected airflow, 14.5 kilograms per second; nominal inlet mass-flow ratio, 0.61; wing angle of attack, 11° (clockwise vortex).

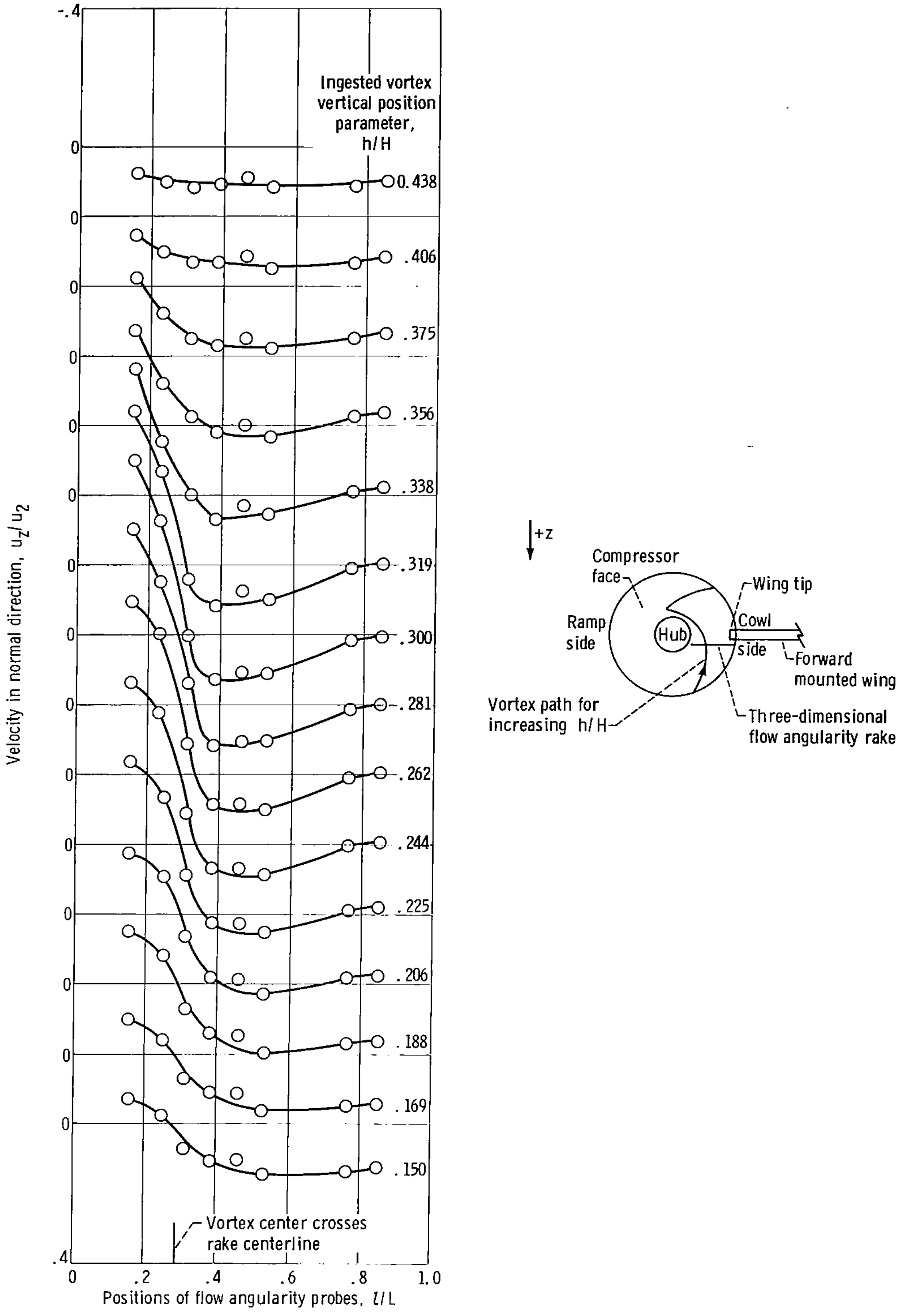

(b) Normal velocity profiles.

Figure 28. - Continued.

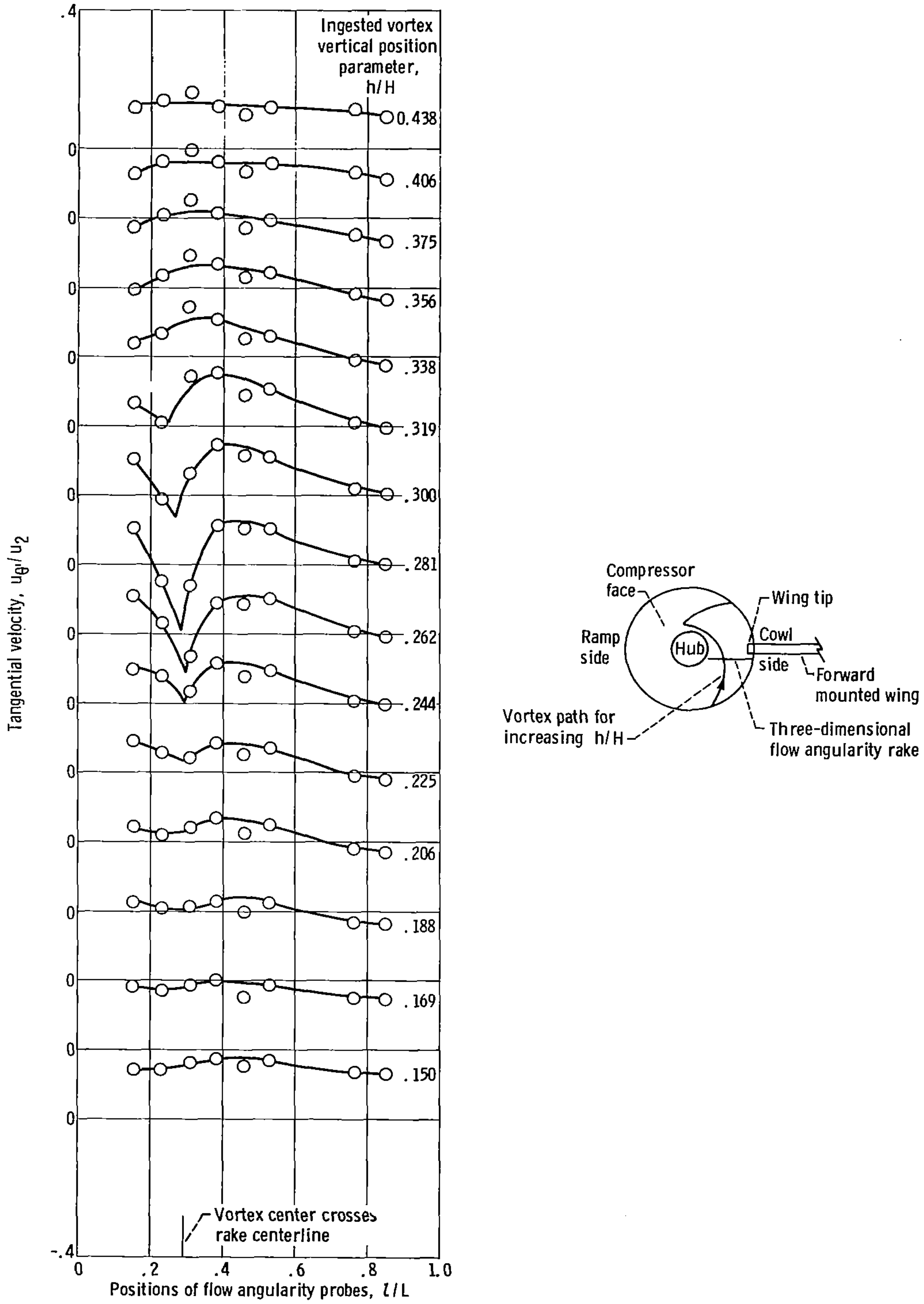

(c) Tangential velocity profiles.

Figure 28. - Continued.

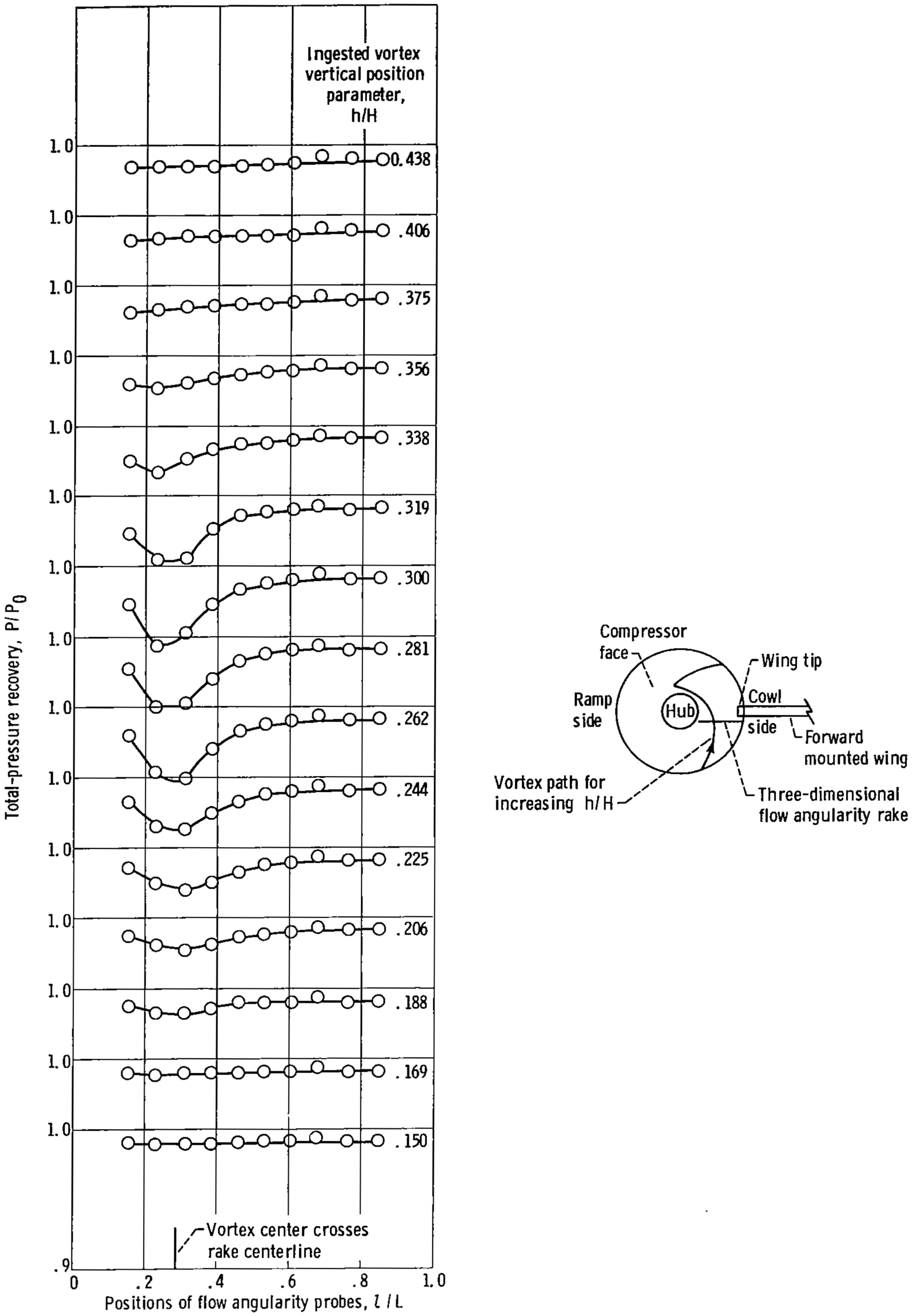

(d) Total-pressure recovery profiles.

Figure 28. - Continued.

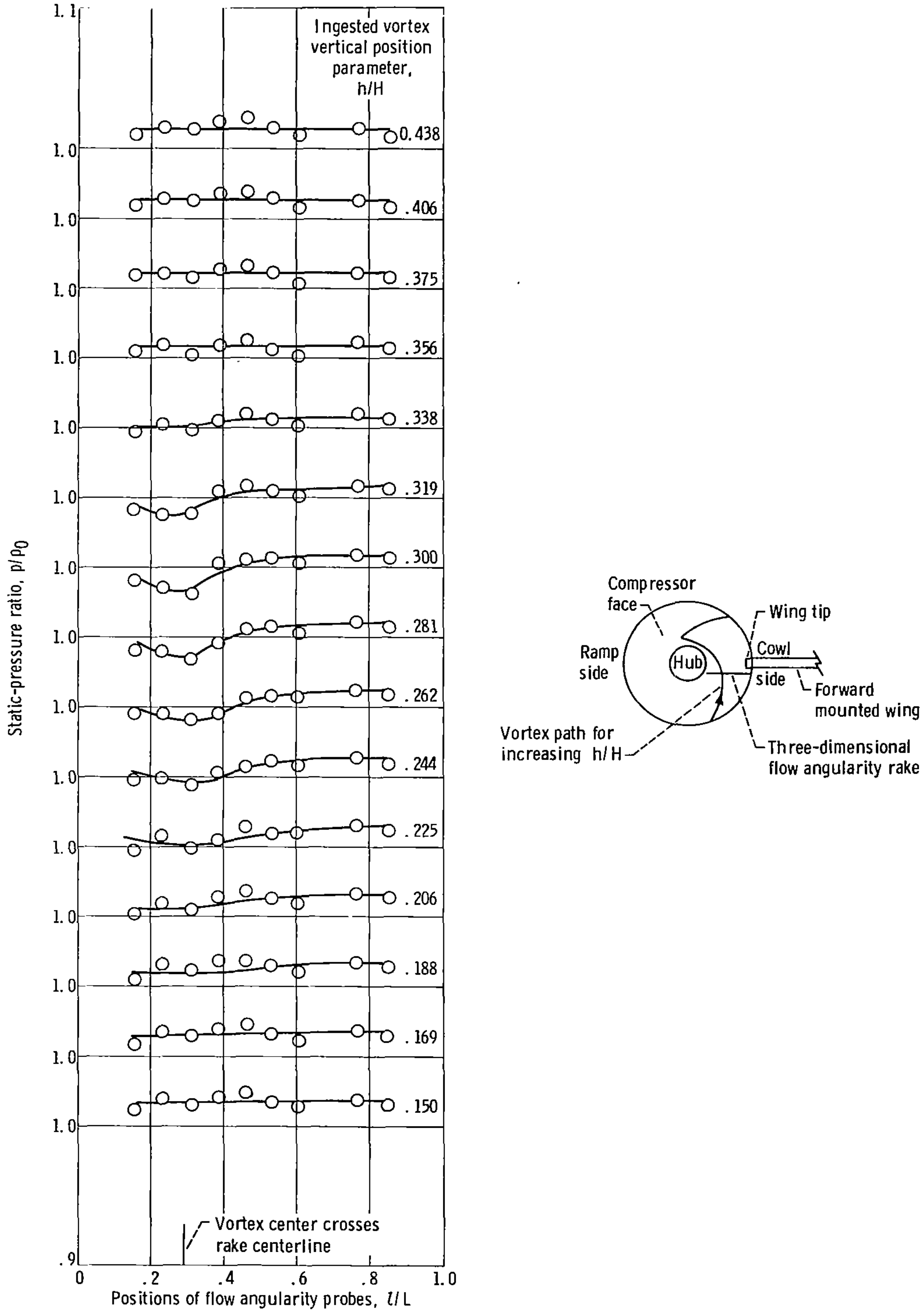

(e) Static-pressure ratio profiles.

Figure 28. - Continued.

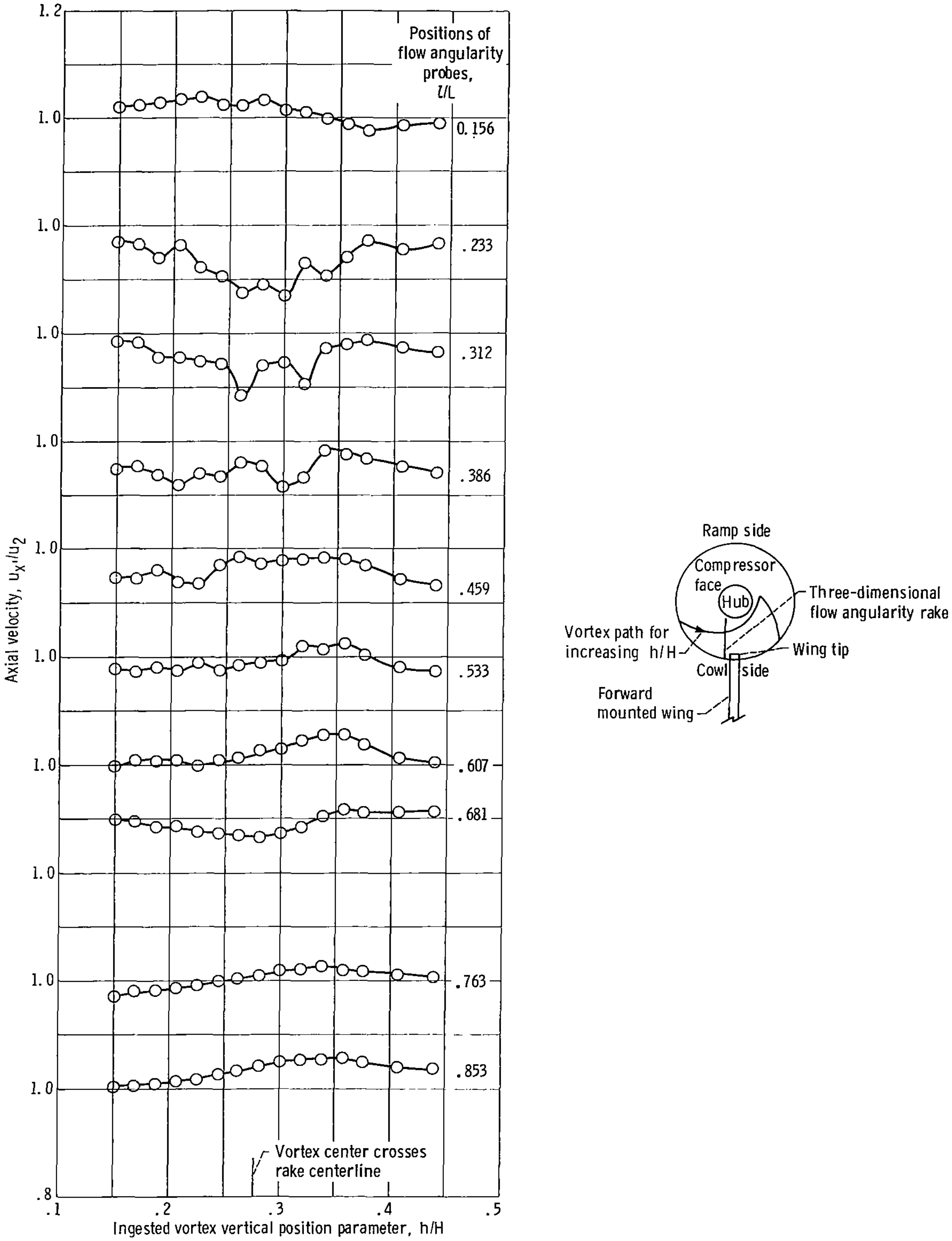

(f) Axial velocity profiles.

Figure 28. - Concluded.

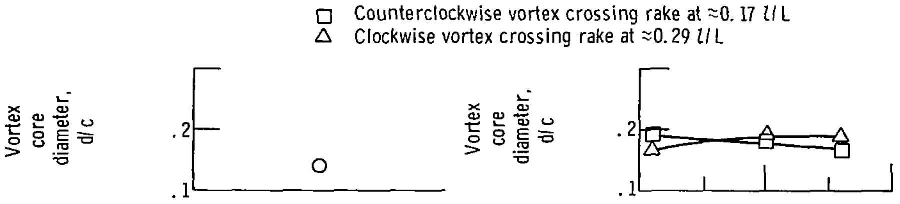

(a-1) Vortex core diameter.

(b-1) Vortex core diameter.

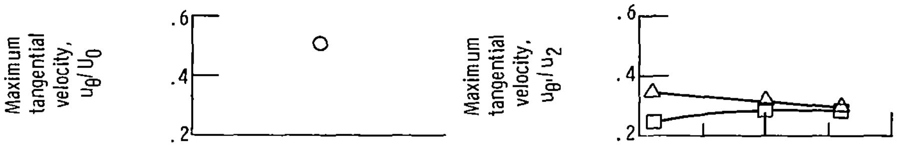

(a-2) Tangential velocity.

(b-2) Tangential velocity.

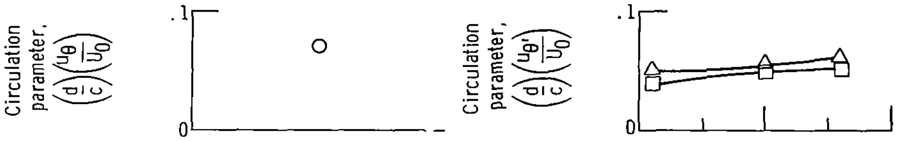

(a-3) Circulation parameter.

(b-3) Circulation parameter.

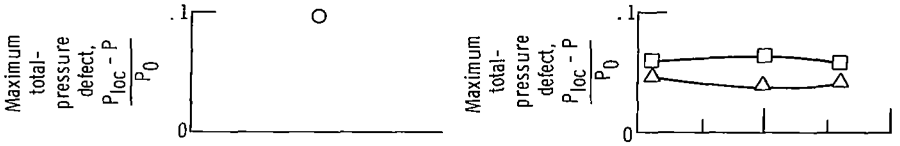

(a-4) Total-pressure defect.

(b-4) Total-pressure defect.

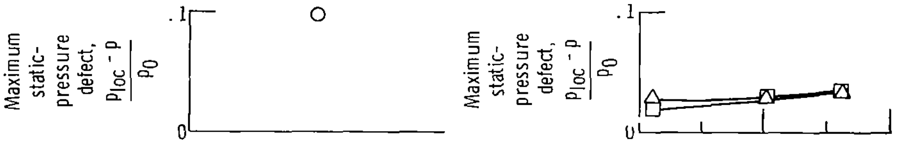

(a-5) Static-pressure defect.

(b-5) Static-pressure defect.

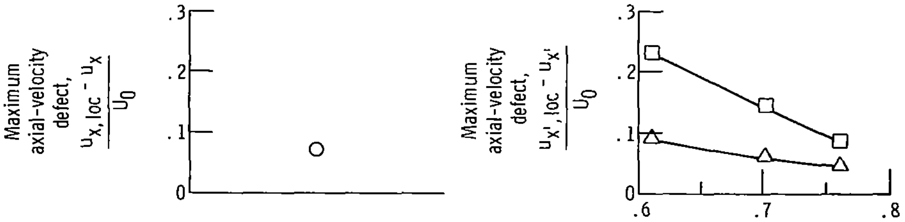

(a-6) Axial-velocity defect.

(b-6) Axial-velocity defect.

(a) Vortex properties prior to entering inlet (counterclockwise vortex), x/c = 7.03.

(b) Vortex properties at compressor face, x/c = 17.5.

Figure 29. - Summarized vortex properties.

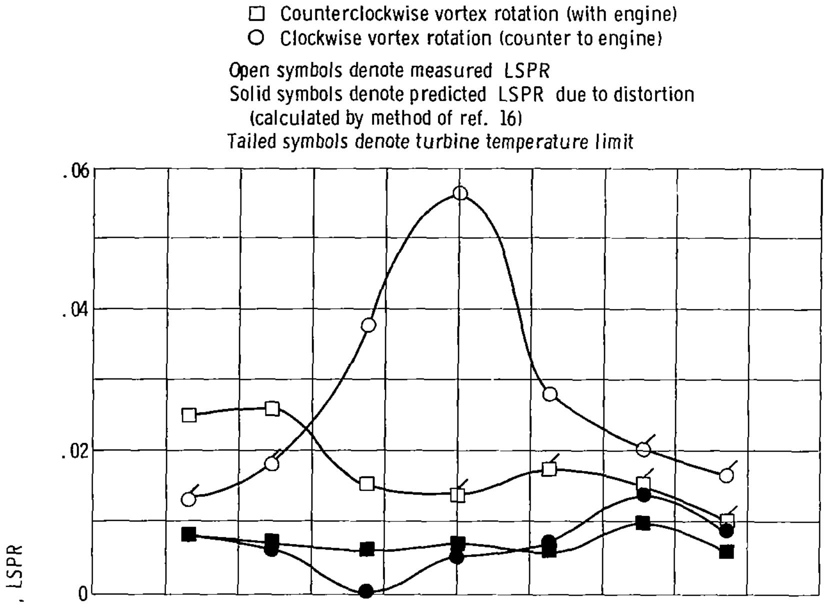

(a) Nominal engine corrected airflow, 18 kilograms per second; nominal inlet mass-flow ratio, 0.76.

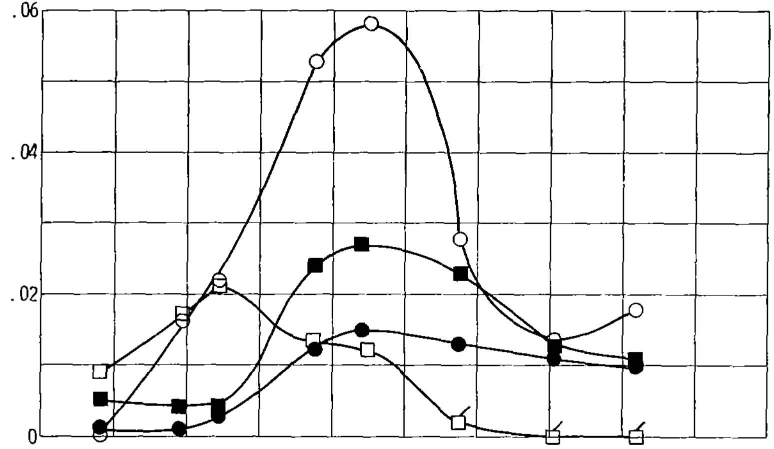

(b) Nominal engine corrected airflow, 16.5 kilograms per second; nominal inlet mass-flow ratio, 0.70.

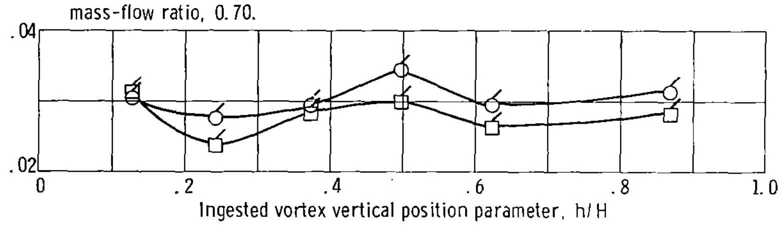

(c) Nominal engine corrected airflow, 14.5 kilograms per second; nominal inlet mass-flow ratio, 0.61.

Figure 30. - Effect of vertical placement of ingested vortex on compressor stall.

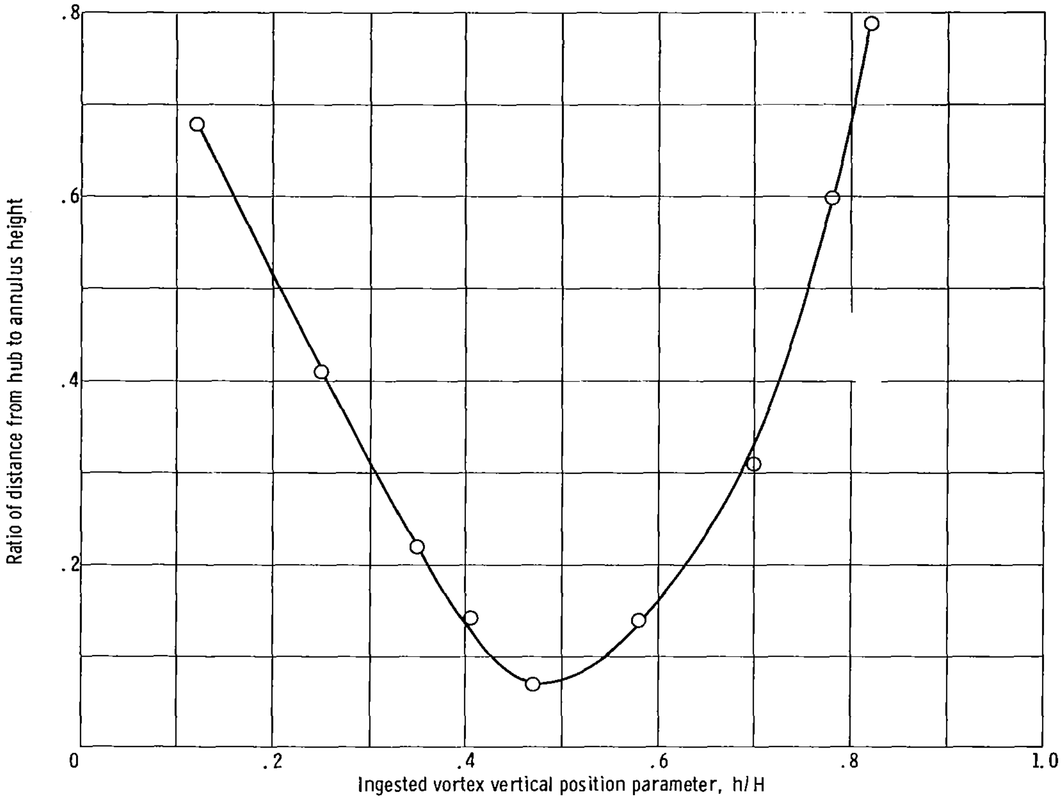

Figure 31. - Radial position of counterclockwise vortex at compressor face. Nominal engine corrected airflow, 18 kilograms per second; nominal inlet mass-flow ratio, 0.76.

NATIONAL AERONAUTICS AND SPACE ADMINISTRATION
WASHINGTON, D.C. 20546

OFFICIAL BUSINESS
PENALTY FOR PRIVATE USE $300

SPECIAL FOURTH-CLASS RATE
BOOK

POSTAGE AND FEES PAID
NATIONAL AERONAUTICS AND
SPACE ADMINISTRATION
451

U.S.MAIL

722 001 C1 U D 750711 S00903DS
DEPT OF THE AIR FORCE
AF WEAPONS LABORATORY
ATTN: TECHNICAL LIBRARY (SUL)
KIRTLAND AFB NM 87117

If Undeliverable (Section 158
Postal Manual) Do Not Return

> *"The aeronautical and space activities of the United States shall be conducted so as to contribute . . . to the expansion of human knowledge of phenomena in the atmosphere and space. The Administration shall provide for the widest practicable and appropriate dissemination of information concerning its activities and the results thereof."*
>
> —NATIONAL AERONAUTICS AND SPACE ACT OF 1958

NASA SCIENTIFIC AND TECHNICAL PUBLICATIONS

TECHNICAL REPORTS: Scientific and technical information considered important, complete, and a lasting contribution to existing knowledge.

TECHNICAL NOTES: Information less broad in scope but nevertheless of importance as a contribution to existing knowledge.

TECHNICAL MEMORANDUMS: Information receiving limited distribution because of preliminary data, security classification, or other reasons. Also includes conference proceedings with either limited or unlimited distribution.

CONTRACTOR REPORTS: Scientific and technical information generated under a NASA contract or grant and considered an important contribution to existing knowledge.

TECHNICAL TRANSLATIONS: Information published in a foreign language considered to merit NASA distribution in English.

SPECIAL PUBLICATIONS: Information derived from or of value to NASA activities. Publications include final reports of major projects, monographs, data compilations, handbooks, sourcebooks, and special bibliographies.

TECHNOLOGY UTILIZATION PUBLICATIONS: Information on technology used by NASA that may be of particular interest in commercial and other non-aerospace applications. Publications include Tech Briefs, Technology Utilization Reports and Technology Surveys.

Details on the availability of these publications may be obtained from:

SCIENTIFIC AND TECHNICAL INFORMATION OFFICE

NATIONAL AERONAUTICS AND SPACE ADMINISTRATION

Washington, D.C. 20546